

Determination of Advection and Diffusion in a Thermohaline Staircase Region

by

Joyce Marie Federiuk

B.A., M.A. Geophysics, University of California at Berkeley
(1980 and 1982)

Submitted to the Department of Earth, Atmospheric and
Planetary Sciences in partial fulfillment of the
requirements of the degree of

Master of Science in Physical Oceanography

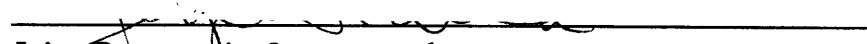
at the

Massachusetts Institute of Technology


October, 1987

© Massachusetts Institute of Technology 1987

Signature of the author


Joint Program in Oceanography,
Massachusetts Institute of Technology -
Woods Hole Oceanographic Institution, October 1987.

Certified by


Carl Wunsch
Thesis supervisor

Accepted by


W. F. Brace
Chairman, Departmental Committee on Graduate Students

WITHDRAWN
MASSACHUSETTS INSTITUTE
OF TECHNOLOGY
APR 1988
MIT LIBRARIES

Determination of Advection and Diffusion in a Thermohaline Staircase Region

by

Joyce Marie Federiuk

Submitted to the Massachusetts Institute of Technology in October 1987 in partial fulfillment of the requirements of the degree of Master of Science in Physical Oceanography.

Abstract

Thermohaline staircases consisting of a series of well mixed layers approximately 30 m thick are found at depths of 300-500 m in a region of the tropical North Atlantic spanning 48° to 58°W, 8° to 17°N. Density ratios ($R_\rho \equiv \alpha T_z / \beta S_z$) with values near 1 indicate a double diffusive origin for the structure (Schmitt, 1981, 1986). Determining the importance of double-diffusive mixing to the regional advection - diffusion balance is the subject of this study. Using hydrographic and current meter data collected in the C-SALT program of 1985 (Schmitt, 1987), we construct inverse models in both cartesian and density coordinates and seek bounds on the cross isopycnal mixing in the staircase region. In cartesian coordinates, the role of diffusion was not well resolved, probably due to inadequacy of the steady state model in the presence of eddies. By reformulating the problem in boxes bounded by isopycnals which more closely follow the layers, and solving directly for cross isopycnal fluxes of salt and heat, the resolution of the diffusivities was improved. Inversions were done on data from the spring and fall CTD surveys. The average salt diffusivity in the step region was estimated from the isopycnal inversions to be $\kappa_s = (2.8 \pm 1.3) \text{cm}^2/\text{s}$ in spring and $\kappa_s = (3.9 \pm 2.2) \text{cm}^2/\text{s}$ in fall.

Thesis supervisor:

Carl Wunsch
*Cecil and Ida Green Professor
of Physical Oceanography*

Table of contents

Abstract	2
Chapter 1: Introduction	4
Chapter 2: The Data	15
2.1 Objective Mapping of Tracer Fields	16
2.2 Cartesian Mapping	17
2.3 Isopycnal Mapping	28
2.4 Current Meter Data	32
Chapter 3: Cartesian Inversions	36
3.1 Model Dynamics	36
3.2 Finite Difference Formulation	42
3.3 SVD Solution	44
3.4 Results of Inversions	49
Chapter 4: Isopycnal Inversions	70
4.1 Model Dynamics	70
4.2 Finite Difference Formulation	72
4.3 Results of Inversions	74
Chapter 5: Summary and Conclusions	83
Appendix: Error Estimates	86
References	87
Acknowledgments	90

Chapter 1. Introduction

In the tropical Atlantic just east of Barbados well developed thermohaline staircase structure has been noticed in hydrographic surveys for over a decade (Boyd and Perkins, 1987). The staircases in this region generally occur between depths of 200 and 800 m and consist of a series of well mixed layers 5 to 30 m thick, separated by high gradient interfaces across which the temperature and salinity changes by up to 1° and .2 ppt. Typical CTD profiles from this region are shown in figure 1.

Staircases are found only in regions having a destabilizing salinity gradient and are generally understood to be a manifestation of the salt fingering form of double diffusion (Stern and Turner, 1969, Turner, 1973). In the western tropical North Atlantic the necessary conditions are set up by the confluence of warm, salty Subtropical Underwater (characterized by a salinity maximum at 150 m) overlying cold, fresh Antarctic Intermediate water (salinity minimum at 800 m). These extrema can be easily identified in the salinity profiles in figure 1.

Schmitt (1979) has shown that the strength of the salt fingering depends on the density ratio, R_ρ , which gives the relative contribution of temperature and salinity to the density gradient and is defined by

$$R_\rho = \frac{\alpha T_z}{\beta S_z}$$

where $\alpha = -(1/\rho)\partial\rho/\partial T$, $\beta = (1/\rho)\partial\rho/\partial S$, and T_z and S_z are the vertical gradients of temperature and salinity. Salt fingering can occur for values of R_ρ between 1 and about 100 (Stern, 1960), but is strongest for values near 1 (Schmitt and Evans, 1978), and apparently must be less than about 1.7 for staircases to form (Schmitt, 1981). Well developed staircases have been found under the Mediterranean outflow (eg. Elliot et al., 1974), in the Tyrrhenean Sea (eg. Williams, 1974), in the Caribbean Sea (Lambert and Sturges, 1977) and in a few other regions of strong salinity gradients. Although extensive staircases are not common, much of the Central Water in the world's

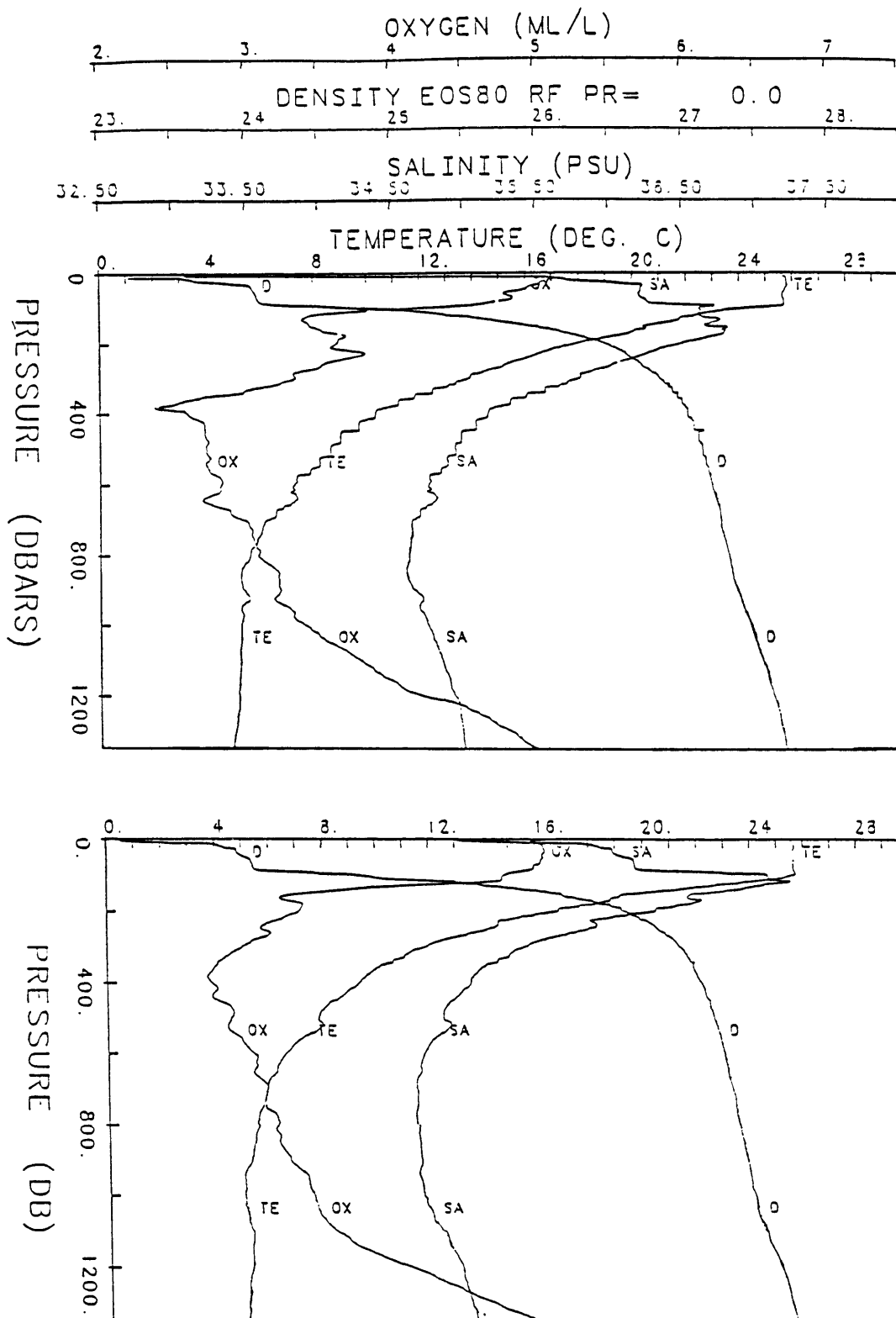


Figure 1. Upper: CTD profiles of temperature, salinity, oxygen and density at 12.4°N, 56.5°W. A well developed staircase can be seen between 300 and 600 db. Lower: profiles from a station 100 km west of the station shown above. Staircase structure is barely discernable at 350 db (from Chandler and Schmitt, 1987).

oceans probably supports vigorous salt fingering, as evidenced by R_ρ values near 2 and irregular finestructure (Schmitt and Evans, 1978). Schmitt (1981) postulated that double diffusion may be responsible for the form of the T-S relationship of the main thermocline, which closely follows curves of constant R_ρ (Ingham, 1966).

The widespread presence of salt fingers inferred from R_ρ values in the Central Water, coupled with estimates of heat and salt fluxes extrapolated from laboratory experiments, suggests that the salt fluxes due to double diffusion may be a significant contribution to large scale mixing and the evolution of water masses (Schmitt and Evans, 1978). This idea was supported by a study of advection and double-diffusion in a thermohaline staircase in the eastern Caribbean Sea. Lambert and Sturges (1977) estimated double-diffusive heat and salt fluxes by applying laboratory flux laws to observed layer characteristics. They found that the vertical flux of salt could be balanced by the horizontal advection, (assuming small vertical advection with $w \approx 10^{-5} \text{ cm/s}$). But advection rates were uncertain (both horizontal and vertical), and because the intensity of fingering had never been directly measured in the ocean it was not known whether laboratory experiments could be extrapolated to oceanic conditions.

The 1985 C-SALT field experiment was instigated by R. Schmitt to try to directly measure the extent and intensity of salt fingering, deduce the fluxes of heat and salt and to relate them to the large scale distribution of hydrographic properties. The program included intense surveys of the region just east of Barbados on regional, fine and microscales. Details of the instruments used and measurements taken are given in Schmitt (1987). AXBT surveys of the region were done in the spring and fall of 1985 to define the distribution of the staircases. CTD surveys of a dense grid of stations were done in the spring and fall of 1985. Figure 2 shows the location of the fall CTD stations relative to the distribution of staircases. The spring survey, done in March and April from the R. V. Endeavor, sampled interior stations to 2100 m and perimeter stations to the bottom, which is generally between 4000 and 5000 m, shallowing to

1400 m in the southwest corner. The November survey from R. V. Knorr repeated the perimeter stations and alternate northeast–southwest transects in the interior. The fall cruise also included fine and microstructure sampling in the staircase. A mooring with 10 current meters was deployed in the center of the CTD grid during the spring survey and removed after the fall survey.

Preliminary results of the C–SALT program are discussed in Schmitt et al. (1987). The layers were found to be horizontally coherent over hundreds of kilometers and individual layers (identified by thermistors on the mooring) were found to persist for at least 8 months. Thicknesses of the interfaces between mixed layers ranged from about .5 to 3 m, which is an order of magnitude greater than the thicknesses predicted by the commonly used $4/3$ power law (Stern, 1976) for the density flux of salt. Measurements of dissipations and layer thicknesses in the C–SALT study support use of flux laws based on the Stern number, which give lower fluxes and dissipation rates than the $4/3$ power law used by Lambert and Sturges (1977) (Schmitt et al., 1987).

This study focuses on the role of double diffusion in the regional and mesoscale circulation and distribution of hydrographic properties. Accordingly, we review here the regional circulation and hydrography. The large scale property distributions, analyzed by Wüst using the ‘core method’ (Wüst, 1964), clearly indicate the origin of the salinity extrema above and below the staircases. A salinity transect through the staircase region (from Wüst, 1964) is shown in figure 3. The salinity maximum at about 150 m depth can be traced to its outcrop in the high evaporation region of the Sargasso Sea. Near 800 m depth, the salinity minimum of the Antarctic Intermediate water is traceable across the equator, through the C–SALT region and into the Caribbean Sea (see eg. Fuglister, 1960 or Wüst, 1964). Between the depths of these water masses, the water in the C-SALT region shows T–S characteristics intermediate between those of the North Atlantic Central Water (NACW) and the South Atlantic Central Water (SACW) (Boyd and Perkins, 1987, Schmitt et al., 1987).

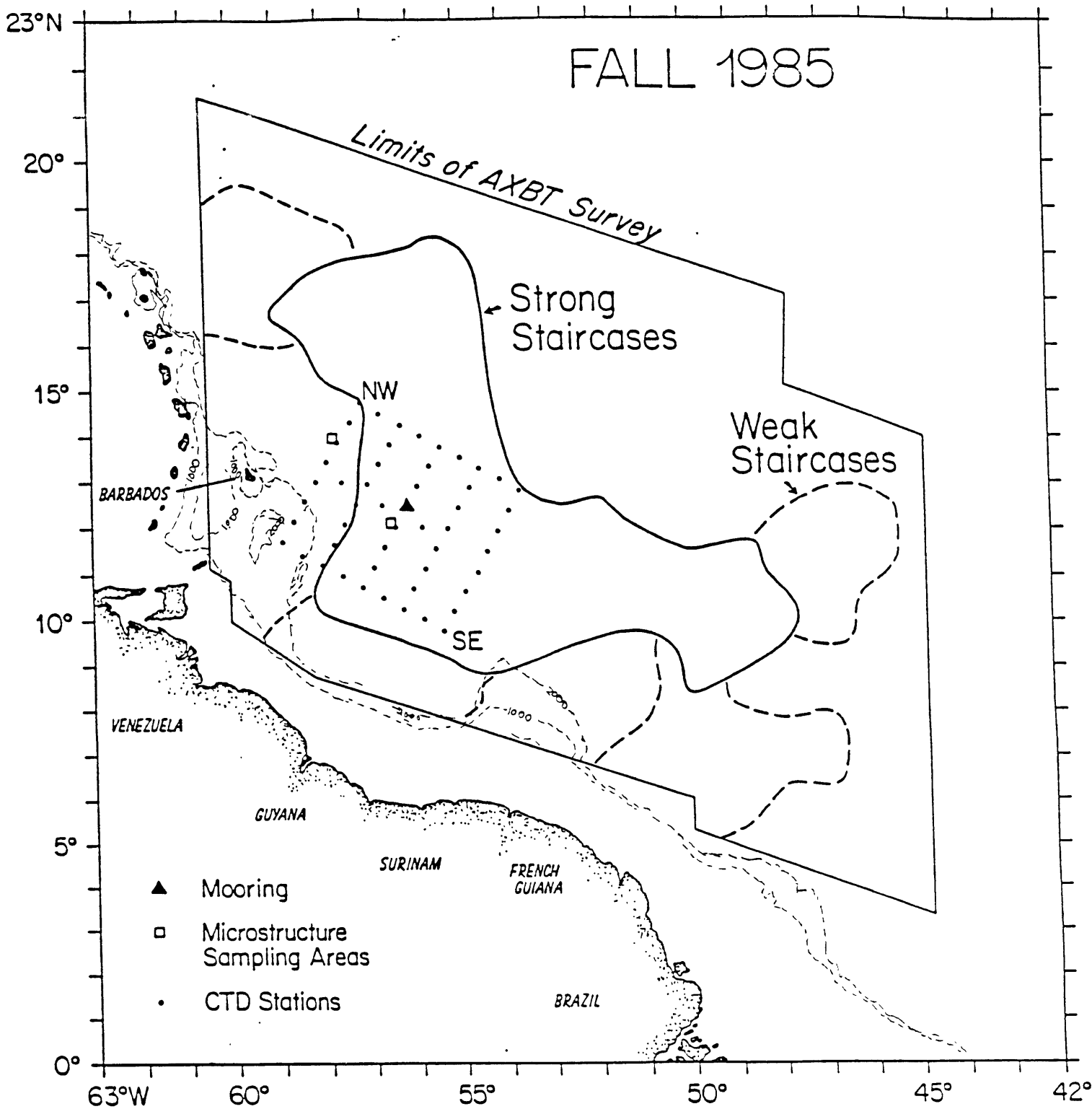


Figure 2. Location of C-SALT CTD grid in regional setting of thermohaline staircases. (from Schmitt et al., 1987) Mooring location is shown with a triangle. Bottom topography is indicated by dotted line.

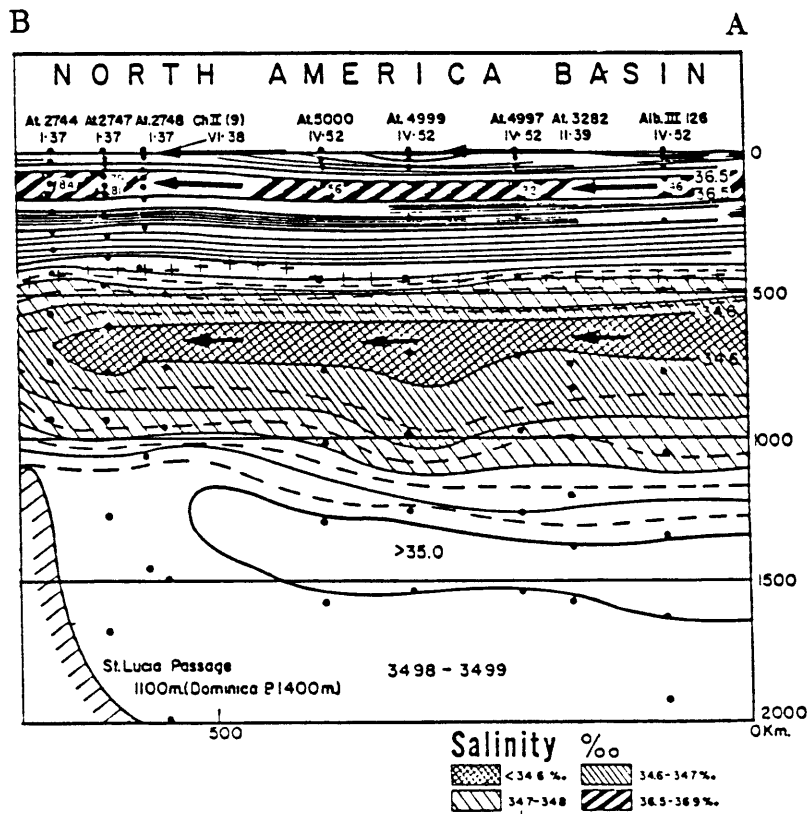
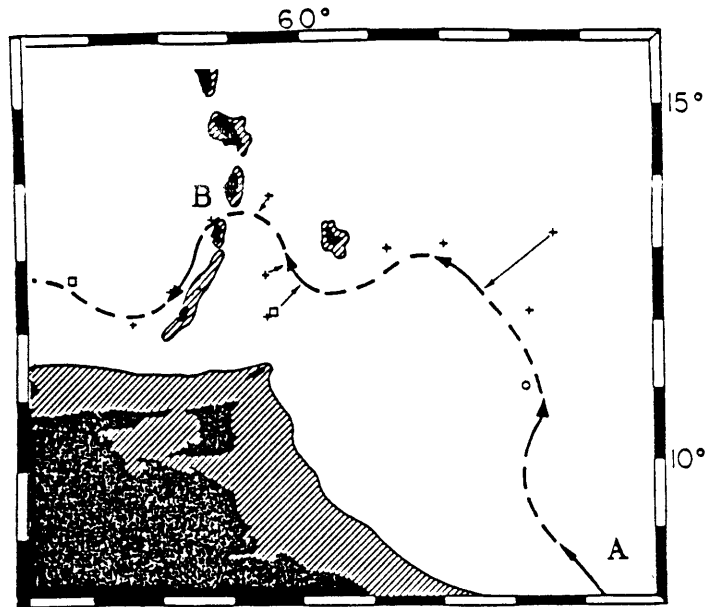


Figure 3. A salinity profile along the track shown in the upper box. Subtropical Underwater is indicated by the bold diagonal at 150 m, and Antarctic Intermediate Water is the tongue of minimum salinity centered at about 700 m (from Wüst, 1964).

General circulation models generally confirm Wüst's ideas about the origins of the salinity extrema. Shown in figure 4 are diagrams of the large scale circulation produced by Olbers et al. (1985) using a β spiral technique with the Levitus data set. At 100 m, near the depth of the subtropical salinity maximum, water moves southwestward from the Sargasso Sea through the C-SALT region and into the Caribbean Sea. No distinctive currents through this region appear at intermediate depths, where the staircases form. At 1000 m, the water moves northward along the coast of South America.

Although the water near 500 m looks quiescent on the regional scale, smaller scale surveys of adjacent regions have found strong currents and eddies. Southeast of the C-SALT region, near 5°N the northward flowing North Brazilian Coastal Current (NBCC) turns offshore to form the Equatorial Undercurrent (Metcalf, 1968 and Bruce and Kerling, 1984). Metcalf (1968) found that northwest of the retroflexion, the water in the 13–24° range (above about 300 m) is supplied by the North Equatorial Current rather than by the Brazilian Coastal Current, and that the flow of water up the coast of South America may be disrupted to depths of about 600 m. This diversion of the NBCC is much stronger in the spring. On the opposite side of the C-SALT region, east of the Lesser Antilles Mazeika et al. (1980) found strong currents and numerous eddies to depths of about 700 m (figure 5). Water with T-S properties similar to those in the C-SALT region was found in an eddy north of Barbados, but this type of water was not detected entering the Caribbean Sea south of 15°N.

In this study we use inverse methods to try to determine the importance of the double-diffusive fluxes to the regional advection-diffusion balance. Inverse methods provide a systematic way of incorporating hydrographic and current meter data as well as dynamical constraints into a self-consistent model of the circulation. The C-SALT data seems particularly well suited to this type of modeling. The CTD surveys are synoptic and eddy resolving. We should therefore not be plagued by the sometimes inconsistent data which arises from non-synoptic coverage of time-dependent flows

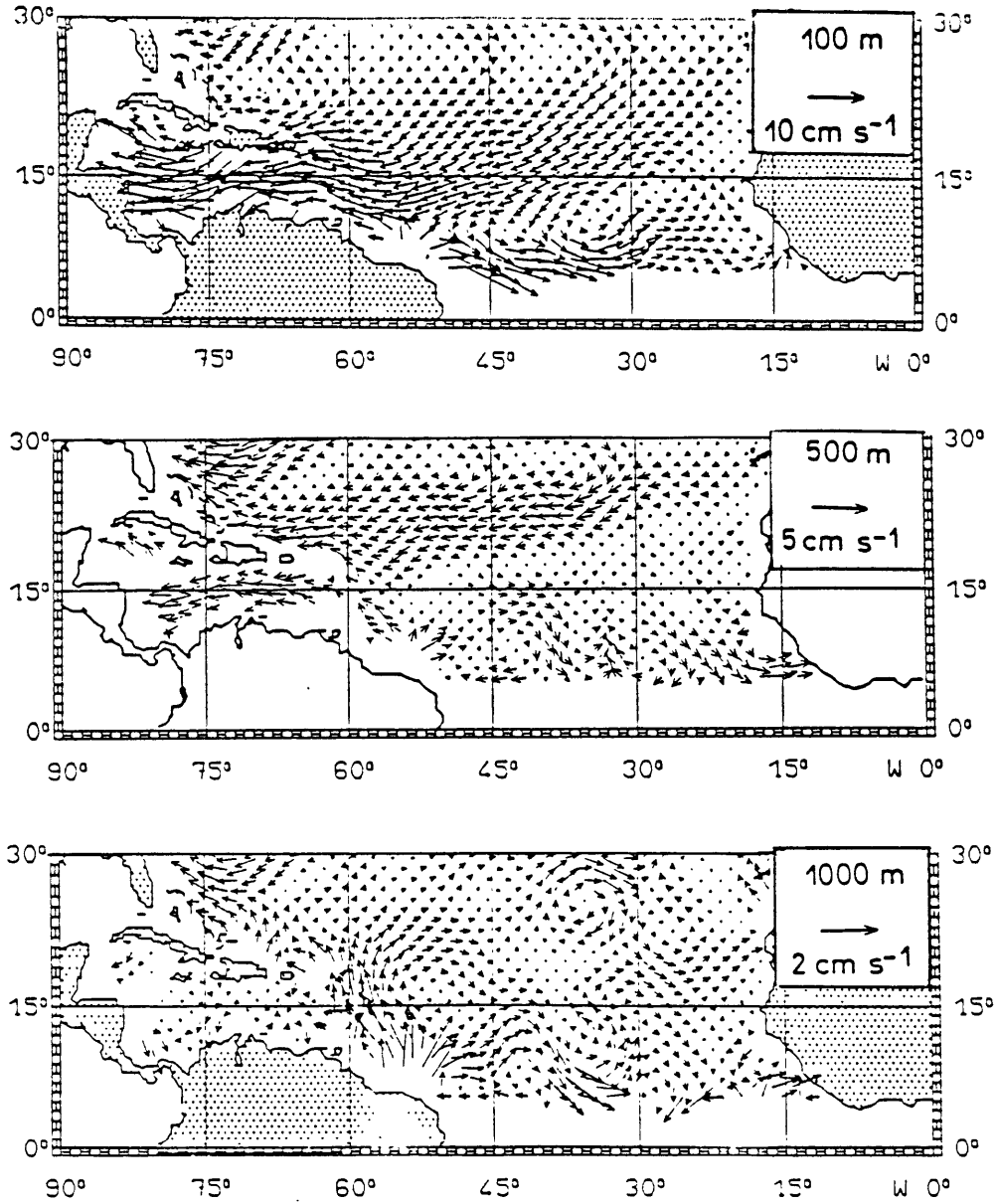


Figure 4. Circulation at 3 levels from the general circulation calculation of Olbers et al., 1985.

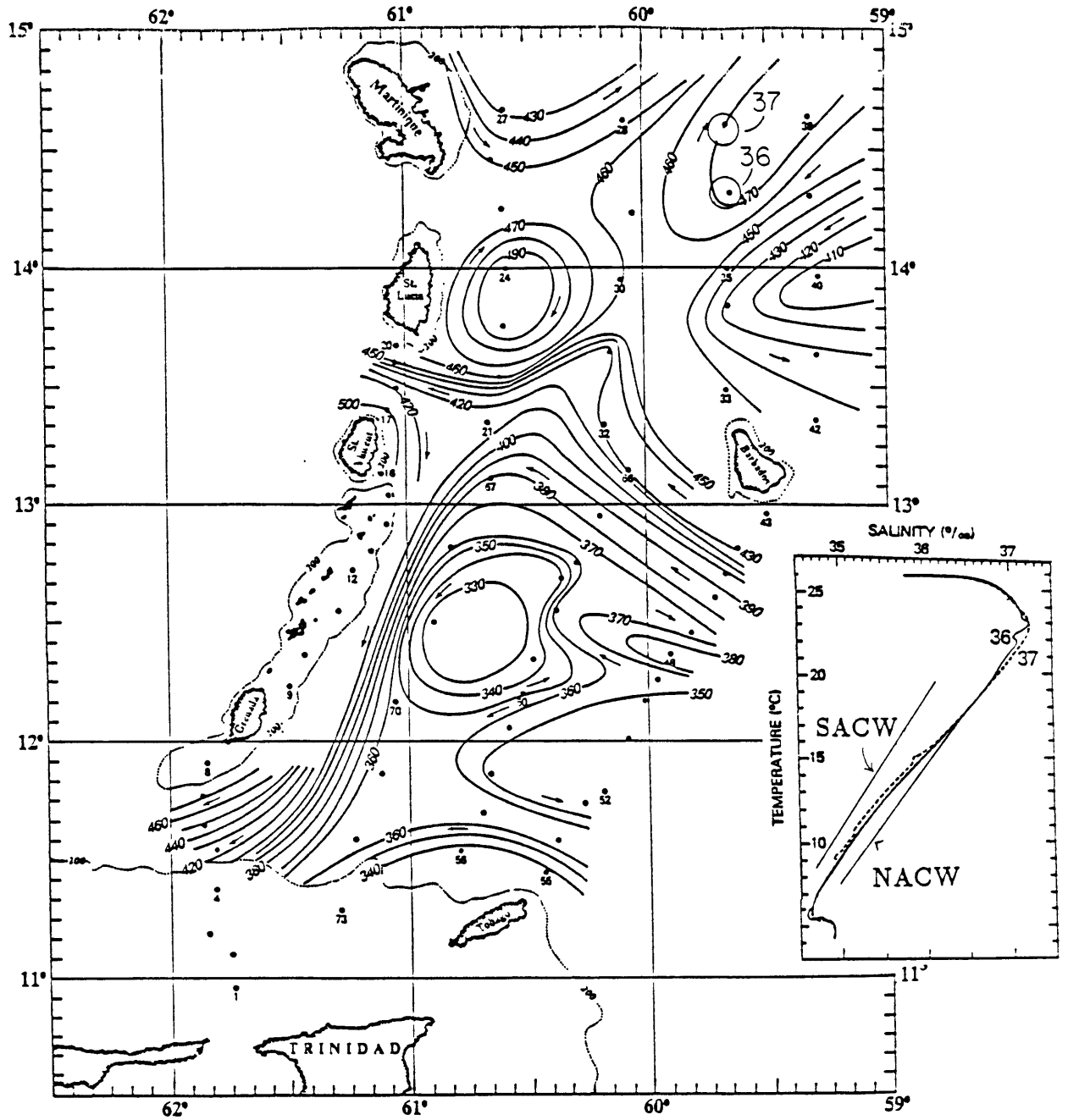


Figure 5. Depth of the sigma theta 27.0 surface from Mazeika et al. (1980). T-S characteristics of water at staircase depths (8° to 12°) looked similar to SACW for all stations except 36 and 37 in the north central eddy. The T-S diagram for these stations shows the mixture of NACW and SACW characteristic of the C-SALT region about 200 km to the west.

(see Wunsch, 1978). Since the CTD stations are spaced closely enough to resolve the eddy field, we might expect the diffusivity in the model to be representative of double-diffusion rather than a parameterization of sub-grid scale eddies.

We impose mass, heat and salt balance constraints and assume geostrophic dynamics. Our model is steady state. Even with spring and fall CTD surveys, we do not know the detailed time evolution of the fields. From the tracer and dynamic constraints and the current meter observations, we determine the reference level velocities and investigate the role of diffusion in the regional dynamics. Inversions are first done using rectangular boxes bounded by pressure surfaces. We attempt to solve for horizontal and vertical reference level velocities and separate heat and salt diffusivities. Since the data are closely spaced we can formulate the inverse problem in finite difference form, as done by Tziperman (1987) and Olbers et al. (1985). This form allows computation of tracer gradients which appear in the diffusion terms of the equations. Although neither of these two previous studies found satisfactory resolution of vertical velocities or diffusivities, Olbers used a non-synoptic data set and Tziperman's data from the eastern Mediterranean contained sub-grid scale eddies. We expect better resolution with the C-SALT data set. After finding a solution in the cartesian formulation we reformulate the problem in boxes bounded by isopycnals and attempt to solve directly for the cross isopycnal mass, heat and salt fluxes. Thermohaline staircases have been found to more closely follow isopycnals than isobars, so isopycnals provide a more natural coordinate system for studying the role of double diffusion.

In Chapter 2, maps of the data on pressure surfaces and isopycnals are presented, and the geostrophic velocities relative to 1000 m are shown and compared with the current meter records. The problem of integrating the current meter data with the hydrographic data is discussed. Chapter 3 includes formulation and results of the pressure surface inversions for both spring and fall data sets. In chapter 4, the isopycnal

formulation is described and the results of the inversions are presented. Chapter 5 contains a summary and comparison of the two formulations.

Chapter 2. The Data

The available data include spring and fall CTD surveys (including oxygen) of the control volume shown in figure 2. Station spacing was 56km in the spring. Because the CTD survey lines run diagonally northeast to southwest, we first map the tracer data onto a north-east grid to facilitate inclusion of beta in the model dynamics. Interpolation for the mapping was done using the objective mapping scheme of Bretherton, Davis and Fandry (1976). The mapping procedure is described in section 2.1. Since inversions are done using boxes bounded by both isobars and isopycnals, we need to map the tracers onto regular grids on both isobaric and isopycnal surfaces. A set of maps of temperature and salinity are made for each type of surface. In section 2.2, tracers and relative geostrophic velocities on isobars are shown, and section 2.3 contains the corresponding maps on isopycnal surfaces. In section 2.4 the current meter data are presented and the use of these constraints on the reference level velocities is discussed.

2.1 Objective Mapping of Tracer Fields

In the objective mapping interpolation scheme, the value of the field at a point \underline{x}_r is expressed as a linear combination of the values at neighboring points \underline{x}_i . Smoothing is determined by specifying the correlation function between neighboring points. We assume for the correlation a Gaussian function of the distance between points, as was used by Roemmich (1983). The expression for the field ϕ at a point \underline{x}_r is, following Bretherton et al. (1976),

$$\phi(\underline{x}_r) = \bar{\phi} + \sum_i \sum_j C_{ir} F_{ij}^{-1} (\phi(\underline{x}_j) - \bar{\phi}) \quad (2.1)$$

with the summation being over all CTD station locations, \underline{x}_j . $\bar{\phi}$ is the objective mean, a spatial average over all the observations, defined in Bretherton et al. (1976) as

$$\bar{\phi} \equiv \frac{\sum_{ij} F_{ij}^{-1} \phi_j}{\sum_{ij} F_{ij}^{-1}}. \quad (2.2)$$

F_{ij} is a square matrix containing the expected products of the observed field at points \underline{x}_i and \underline{x}_j ,

$$F_{ij} = \langle \phi(\underline{x}_i) \phi(\underline{x}_j) \rangle + \delta_{ij} E \quad (2.3)$$

where E is the observational error in each measurement. C_{ir} is a matrix containing the expected products of the measured field and the field interpolated to points (\underline{x}_r),

$$C_{ir} = \langle \phi(\underline{x}_i) \phi(\underline{x}_r) \rangle. \quad (2.4)$$

The correlation function is taken to be

$$\langle \phi(\underline{x}_i) \phi(\underline{x}_j) \rangle = \bar{\phi}^2 e^{-\frac{d^2}{l^2}}$$

where d is the distance between \underline{x}_i and \underline{x}_j , and l is the correlation length scale. The correlation length was chosen to be 100 km, which smooths both data sets to approximately the distance between stations in the fall survey, and preserves the eddy signal.

The error, E , in each CTD measurement was estimated to be $0.01\bar{\phi}^2$, or about 12% of the measured field. The resultant variance in the mapped tracer fields is estimated from (Bretherton et al., 1976)

$$\overline{(\phi(\underline{x}_r) - \phi_{obs}(\underline{x}_r))^2} = C_{rr} - \sum_{ij} C_{ri} F_{ij}^{-1} C_{jr} + \frac{(1 - \sum_{ij} C_{rj} F_{ji}^{-1})^2}{\sum_{ij} F_{ij}^{-1}}. \quad (2.5)$$

To keep the mapping error to a minimum in the inversion procedure, we have evaluated tracer balances only within the region where the resultant tracer variance is less than about 10%, shown in figure 6.

2.2 Cartesian Mapping

After vertically averaging over 40 db, maps of the tracers are made every 50 db in pressure down to 700 db, then every 100 db below. The tracers, smoothed horizontally with the 100 km correlation length scale, are then mapped onto the north–east aligned grid with spacing of $1/2^\circ$, or about 55 km, which is close to the original CTD station spacing in the spring survey.

A schematic of the staggered grid used in the finite difference formulation is shown in figure 7. Density will be obtained from the mapped temperature and salinity at the center and upper right hand corner of each cell. Horizontal geostrophic velocities are computed on the north and south edges (v) and east and west edges (u). Vertical velocities are computed in the centers of the top and bottom faces of the cells.

Maps of the temperature and salinity fields at 400 and 800 db for spring and fall CTD surveys are shown in figures 8–11. Although the most noticeable feature is the eddy field, there is also a north–south gradient in the mean fields, the water being generally warmer and saltier in the north. Between the spring and fall data sets there is also a cooling and freshening trend in the mean temperature and salinity fields at each depth. At 300 db the spring to fall change is about -0.4° and -0.01 ppt and tapers off to zero near 700 db.

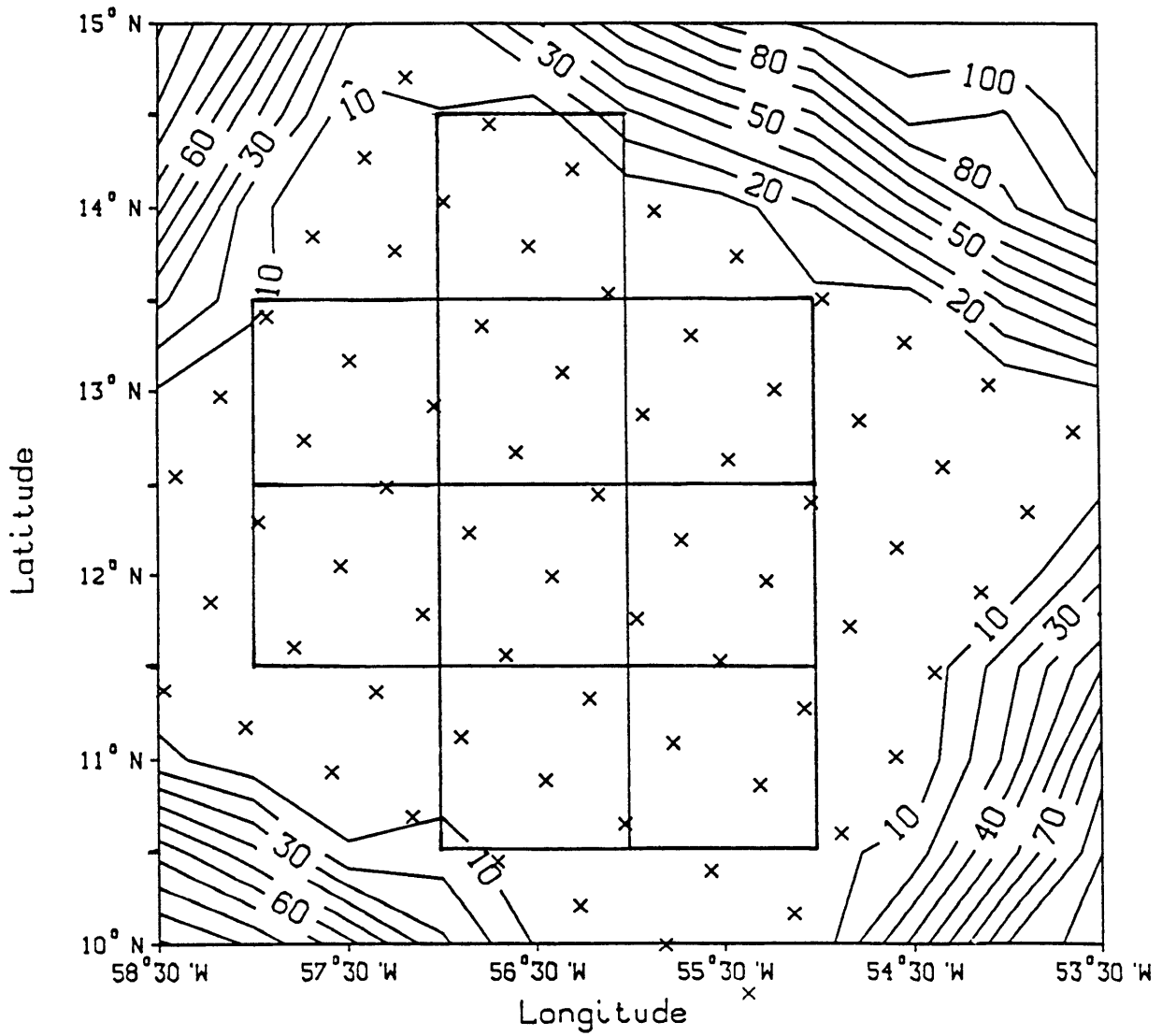
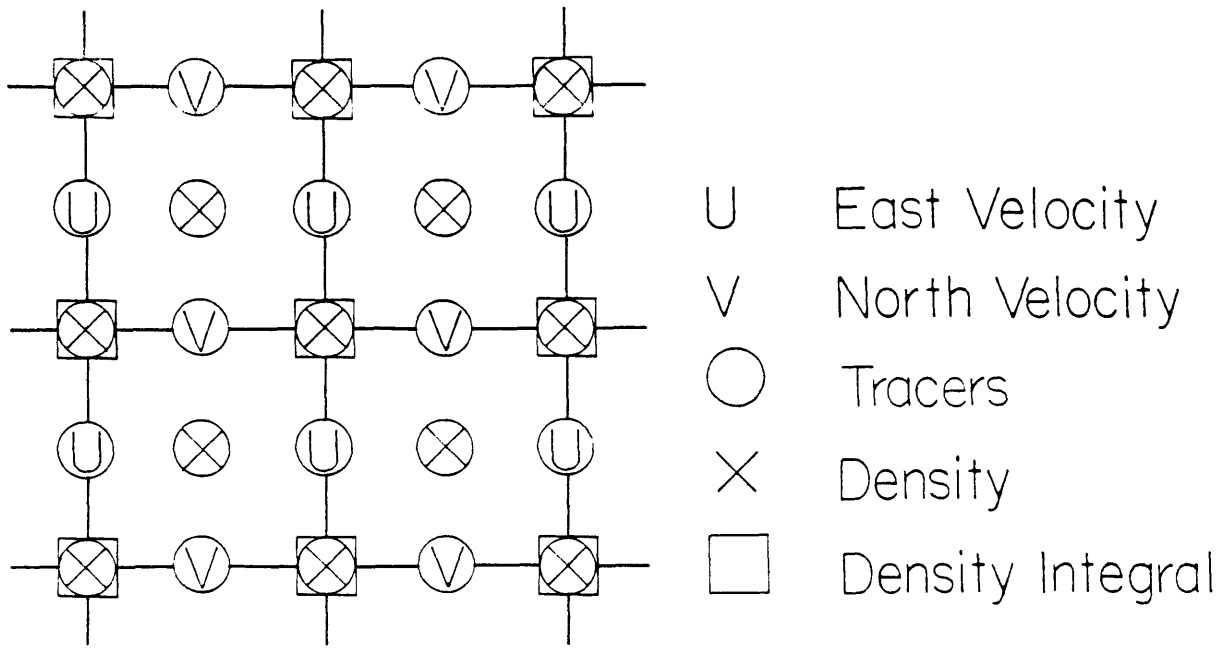
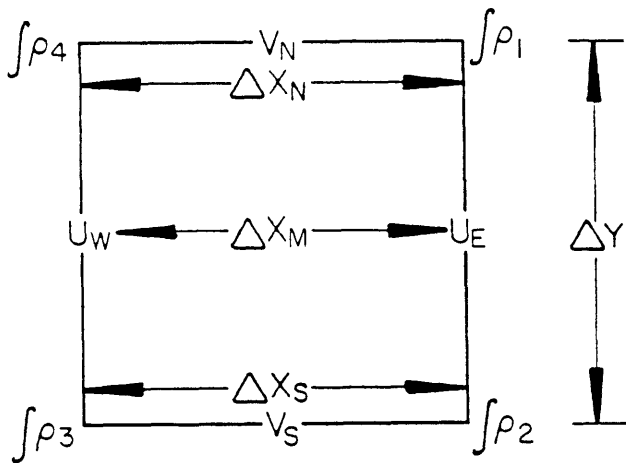


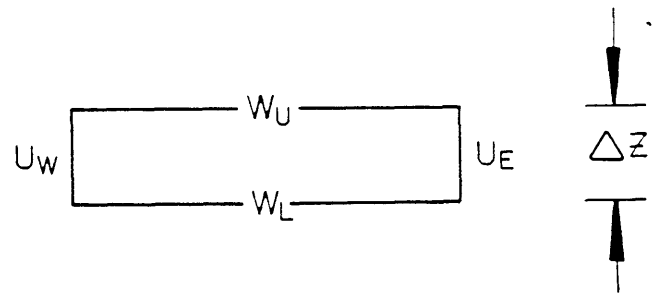
Figure 6. Variance of the error in the mapped tracer fields relative to the location of the CTD stations. Tracer balances are evaluated in the boxes shown.



a.



b.



c.

Figure 7. a) Staggered grid. b) Plan view of 1 cell. c) Side view of 1 cell.

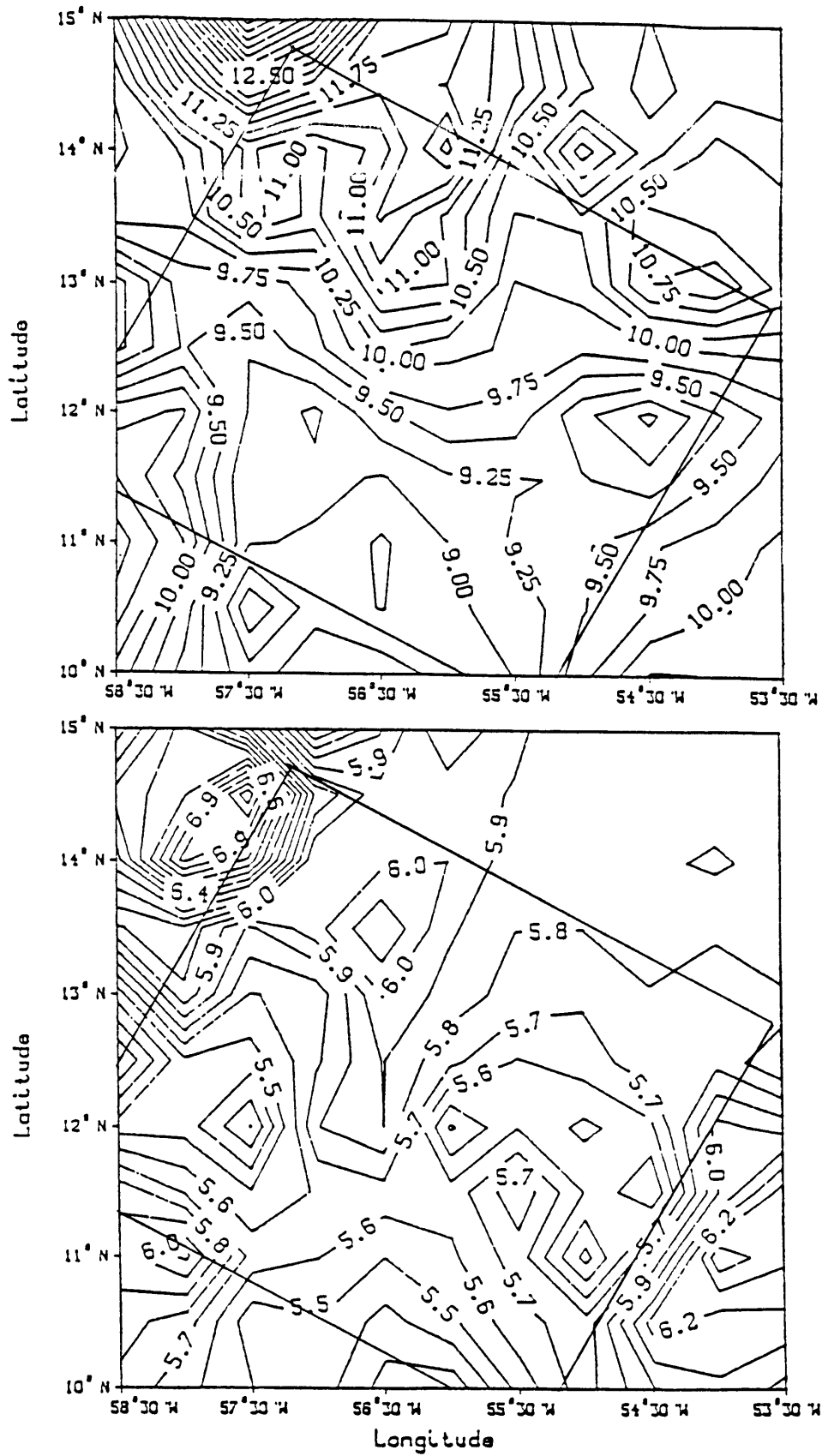


Figure 8. Temperature fields at 400 db (upper) and 800 db (lower) for spring. The CTD grid is outlined.

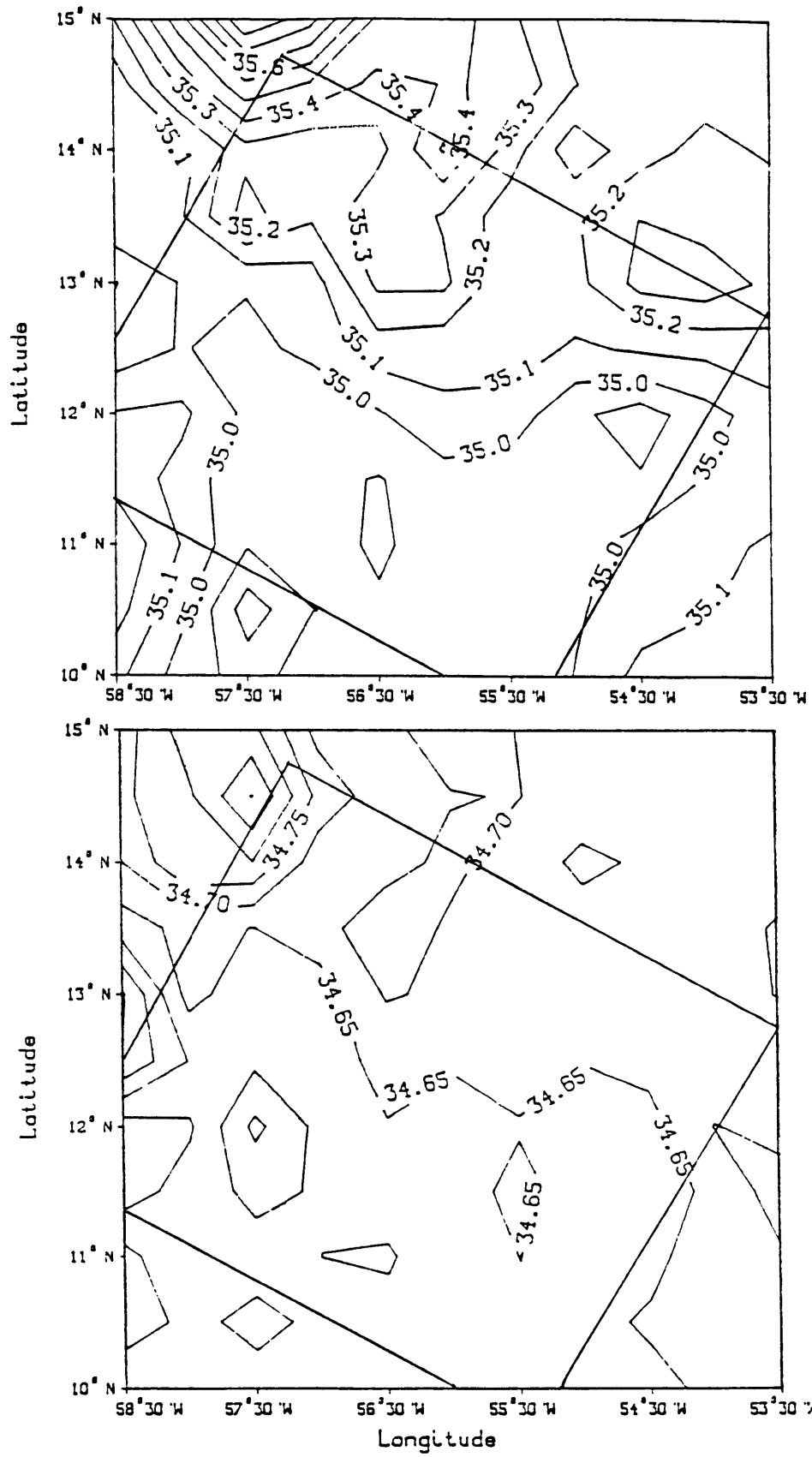


Figure 9. Salinity fields at 400 db (upper) and 800 db (lower) for spring. The CTD grid is outlined.

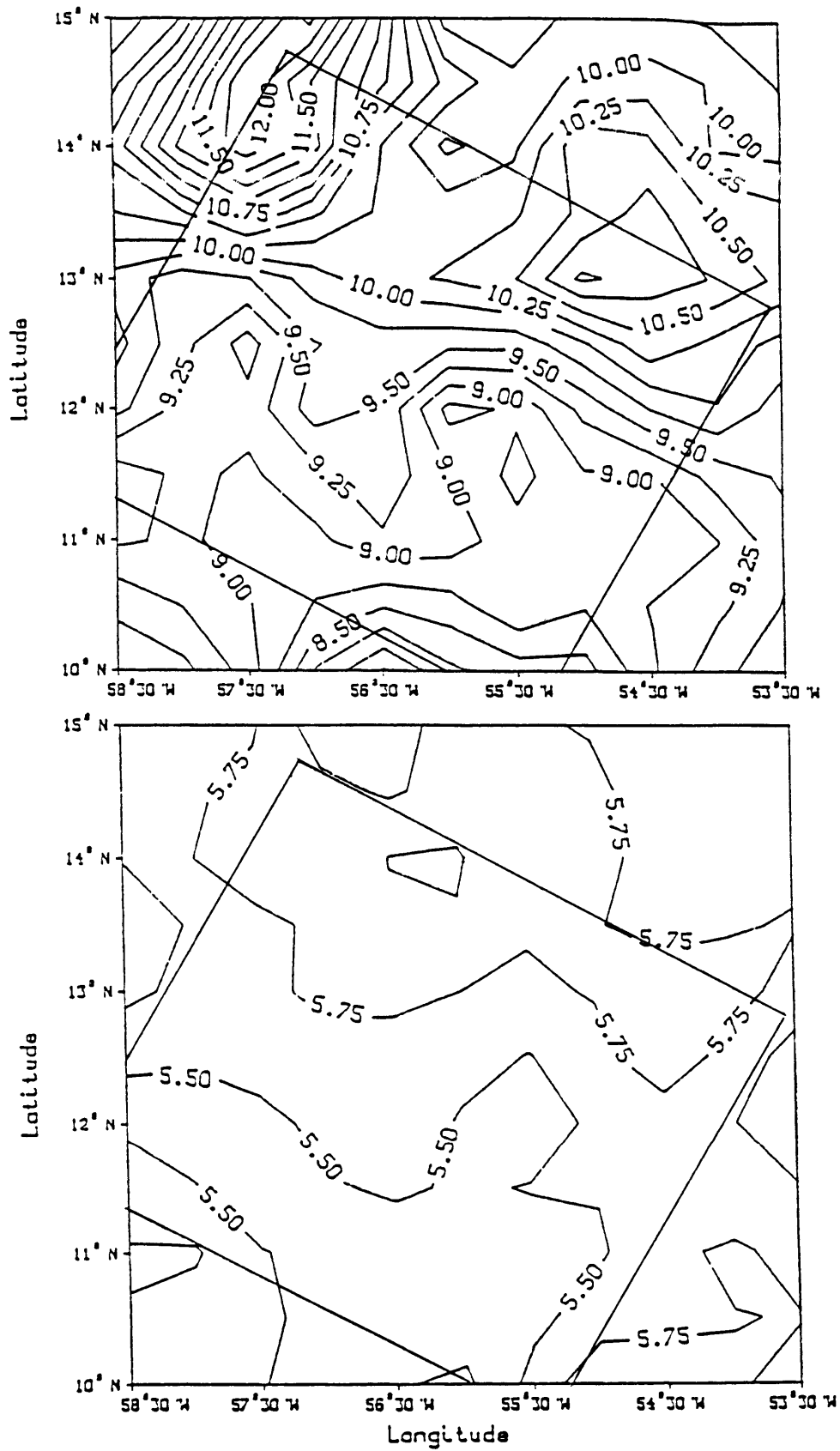


Figure 10. Temperature fields at 400 db (upper) and 800 db (lower) for fall. The CTD grid is outlined.

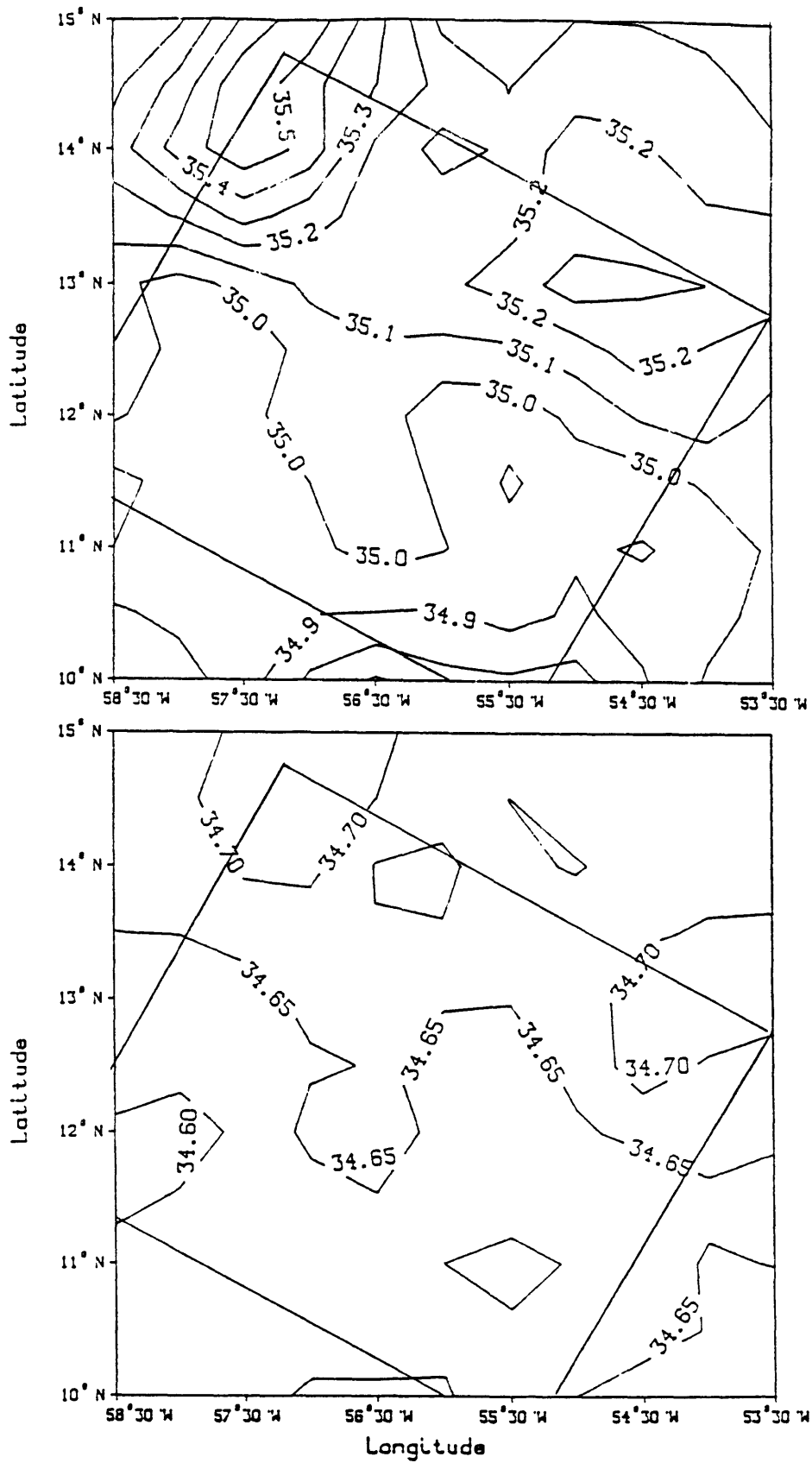


Figure 11. Salinity fields at 400 db (upper) and 800 db (lower) for fall. The CTD grid is outlined.

Geostrophic Velocities

Geostrophic velocities relative to reference level z_0 are computed from the integrated thermal wind equations

$$\begin{aligned} u_{rel} &\equiv \frac{g}{f \rho_0} \int_{z_0}^z \rho_y dz \\ v_{rel} &\equiv -\frac{g}{f \rho_0} \int_{z_0}^z \rho_x dz. \end{aligned} \tag{2.6}$$

Velocites were computed from integrals of the density (derived from the mapped tracers) at each $1/2^\circ$ gridpoint. Details of the finite difference scheme are given in section 3.2. The reference level used is 1000m, where, below the core of the Antarctic intermediate water, we are assuming velocities are small. The reference level velocities then should not be much larger than a few cm/s.

The horizontal relative velocity fields at 400 and 800 db are shown for spring and fall in figures 12 and 13. Both spring and fall fields exhibit energetic eddies embedded in a generally southwestward flow of a few cm/s. The mean flow at 400 db is small, as the general circulation models indicate. At shallower depths the mean westward flow is stronger, as are the eddies. A mean velocity field at 800 db is difficult to discern. The relative flow at that depth does not exhibit the northward flow of about 2 cm/s that Olbers et al. (1985) found. The eddies have velocities 1 to 2 cm/s faster in the spring. We have computed stream lines from the horizontal velocity fields to help visualize the flow, and a comparison of spring and fall flow fields at 400 db is shown in figure 14. The stream lines were constructed by integrating v in the eastward direction and u in the northward direction.

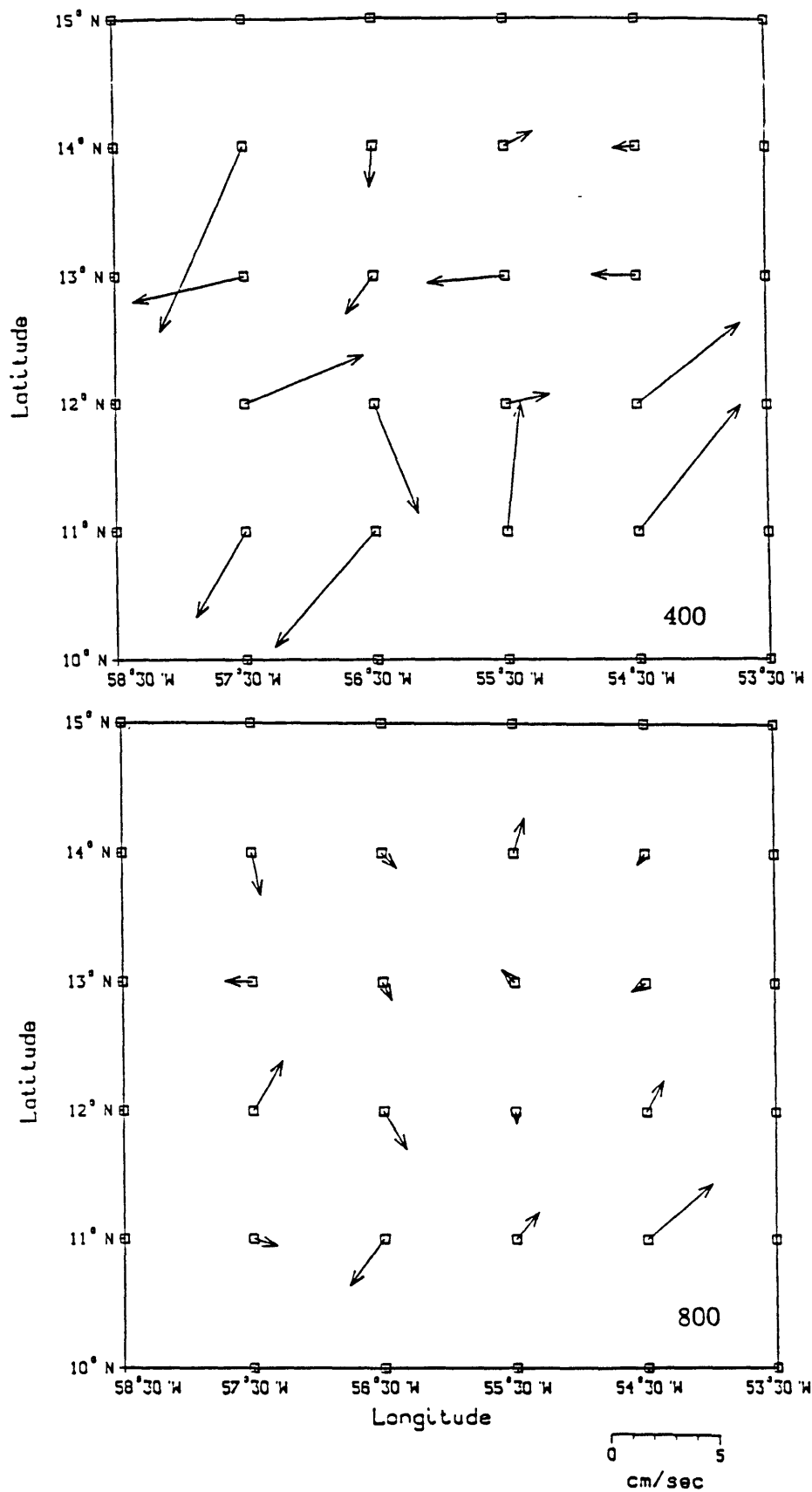


Figure 12. Geostrophic velocity vectors at 400 and 800 db relative to 1000 db for spring.

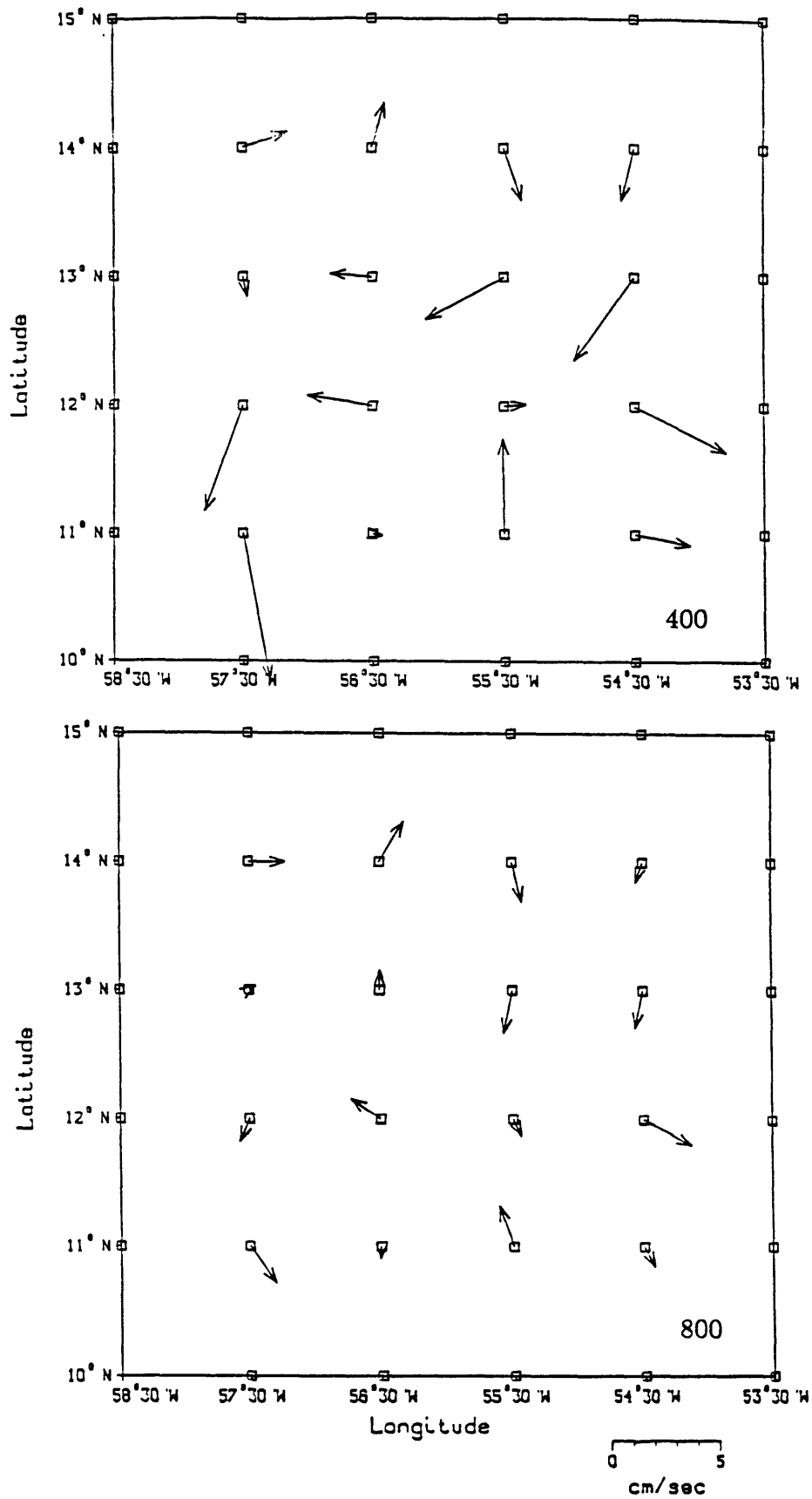


Figure 13. Geostrophic velocity vectors at 400 and 800 db relative to 1000 db for fall.

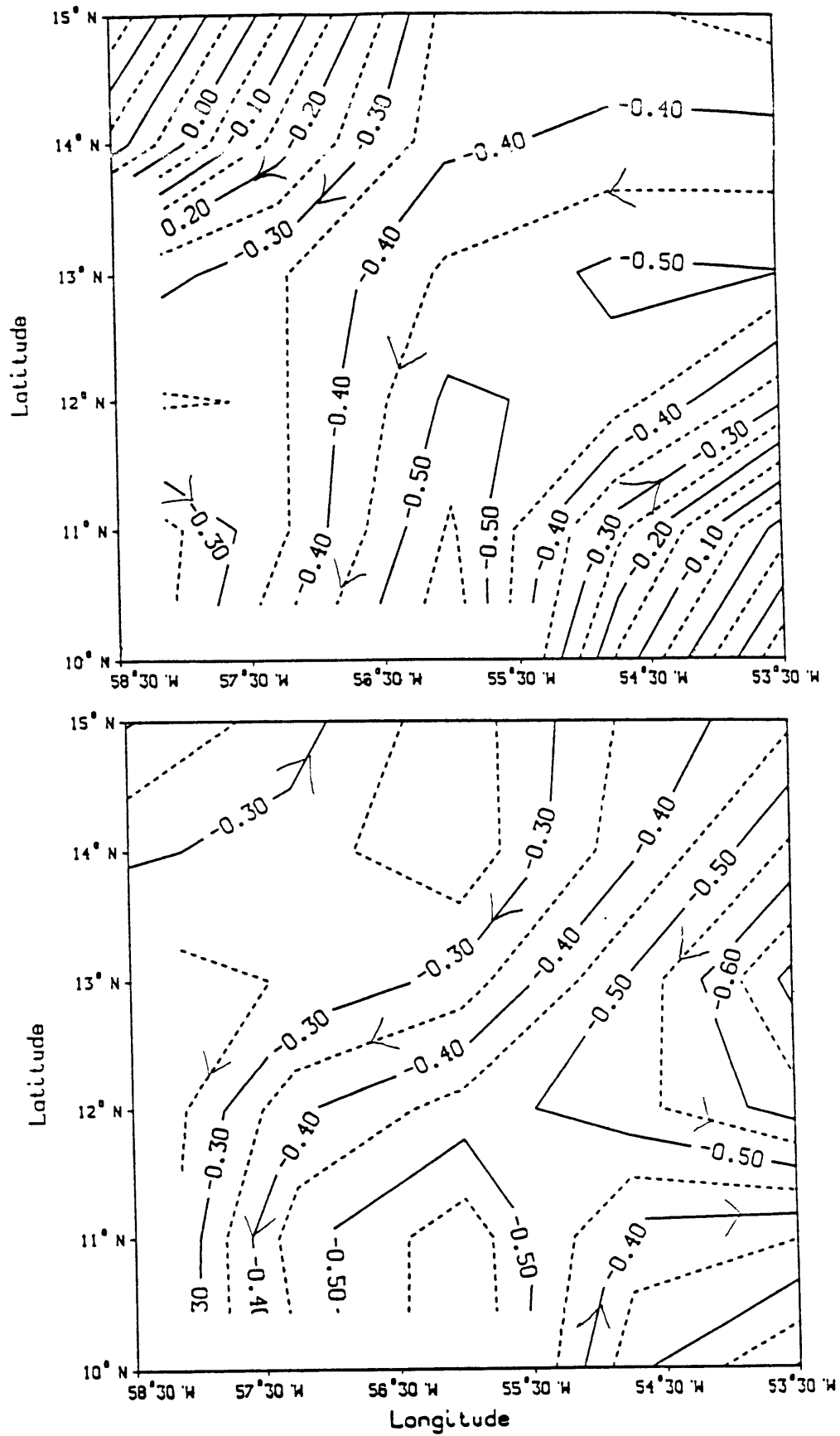


Figure 14. Stream lines at 400 db for spring (upper) and fall (lower).

2.3 Isopycnal Mapping

The 1 db pressure sorted CTD data, temperature, salinity, oxygen and dynamic height was first running averaged over 10 db in depth, then linearly interpolated in z for values on the isopycnal surfaces. At the sigma theta levels used in the inverse model, $\sigma_\theta = 24.5, 26.0, 26.5, 26.8, 26.9, 27.0, 27.1, 27.2, 27.3,$ and 27.4 , tracers were objectively mapped onto the $1/2$ degree square grid. The levels were chosen to define the thermohaline staircases, which are generally confined between 26.8 and 27.2 . Maps of pressure, temperature and salinity for spring and fall data sets on sigma theta 26.9 are shown in figures 15–18. Figure 15 shows the pressure at sigma theta 27.0 for spring and fall. On average, each isopycnal surface is about 30 db shallower in the fall than in spring, reflecting the cooling and freshening trend seen on the pressure surfaces. The average temperature and salinity on isopycnals does not vary significantly between spring and fall.

Geostrophic Velocities

Relative geostrophic velocities evaluated on isopycnals were computed from the dynamic height ϕ on isopycnals. ϕ was first computed on isobars by summing over the specific volume anomalies, δ ,

$$\phi = - \sum_i \delta_i dp_i$$

then interpolated onto isopycnals and objectively mapped to grid points. Horizontal velocities (not along-isopycnal) were evaluated from

$$\begin{aligned} v_\sigma &= \frac{1}{f} \frac{\partial \phi}{\partial x} \Big|_z = \frac{1}{f} \left[\frac{\partial \phi}{\partial x} \Big|_\sigma + \frac{\partial \phi}{\partial z} \frac{\partial z}{\partial x} \Big|_\sigma \right] \\ u_\sigma &= -\frac{1}{f} \frac{\partial \phi}{\partial y} \Big|_z = -\frac{1}{f} \left[\frac{\partial \phi}{\partial y} \Big|_\sigma + \frac{\partial \phi}{\partial z} \frac{\partial z}{\partial y} \Big|_\sigma \right]. \end{aligned} \tag{2.7}$$

The reference level used was sigma theta 27.4 , which lies at an average pressure of 947 db in the spring and 914 db in the fall. This depth is slightly shallower than in the isobaric formulation. Relative velocities on isopycnals look very similar to those

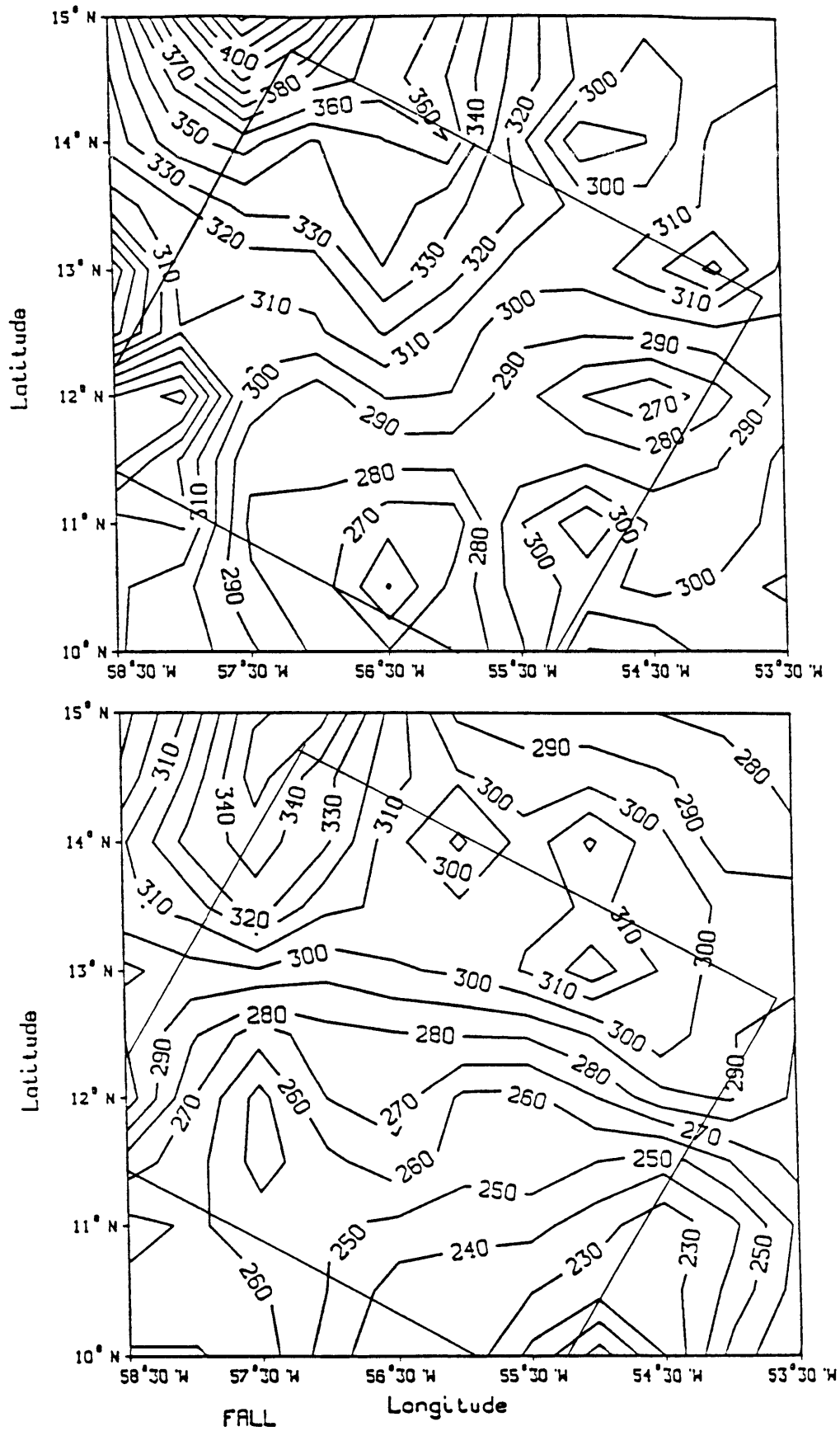


Figure 15. Pressure on sigma theta 26.9 for spring (upper) and fall (lower).

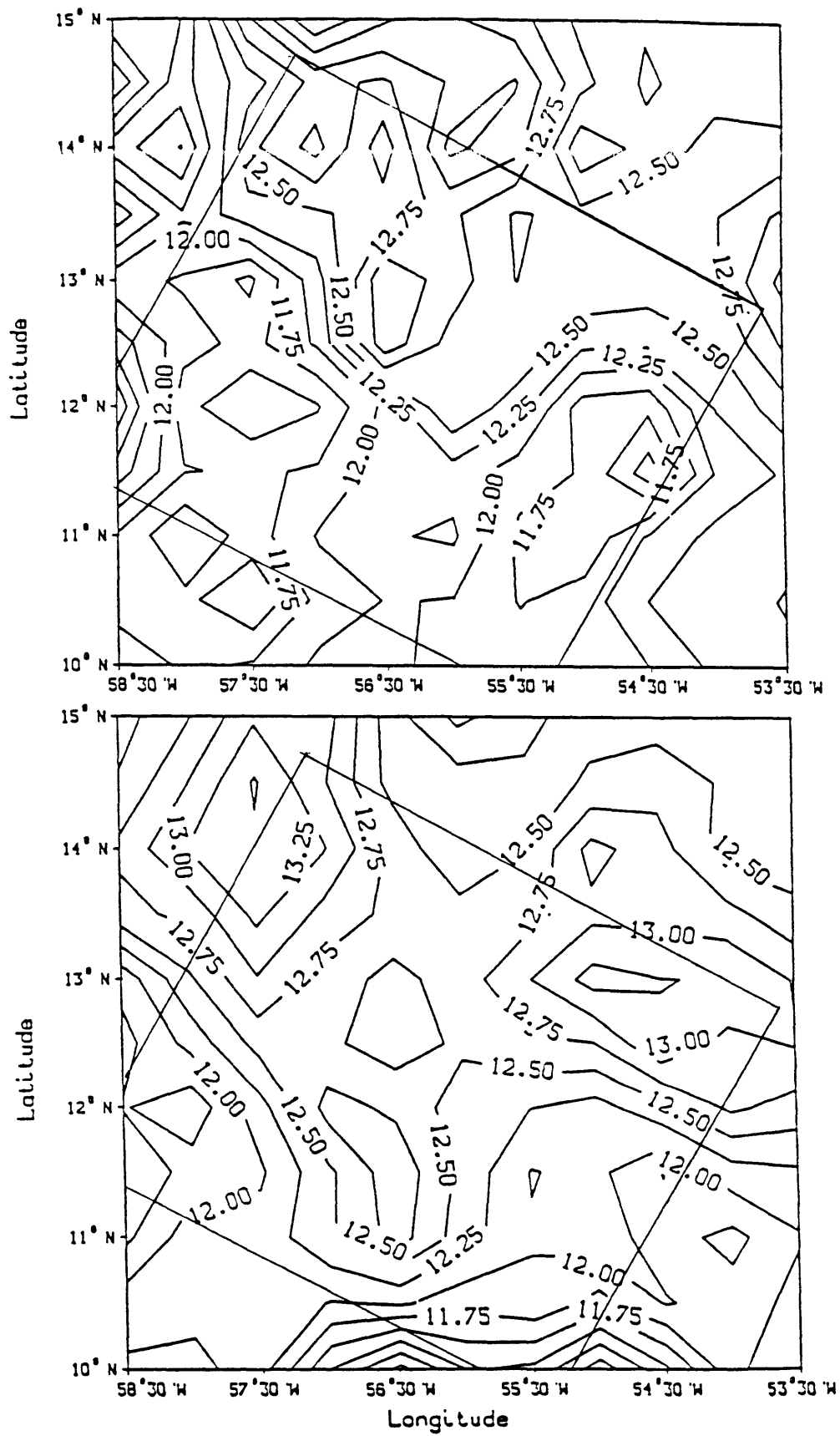


Figure 16. Temperature on sigma theta 26.9 for spring (upper) and fall (lower).

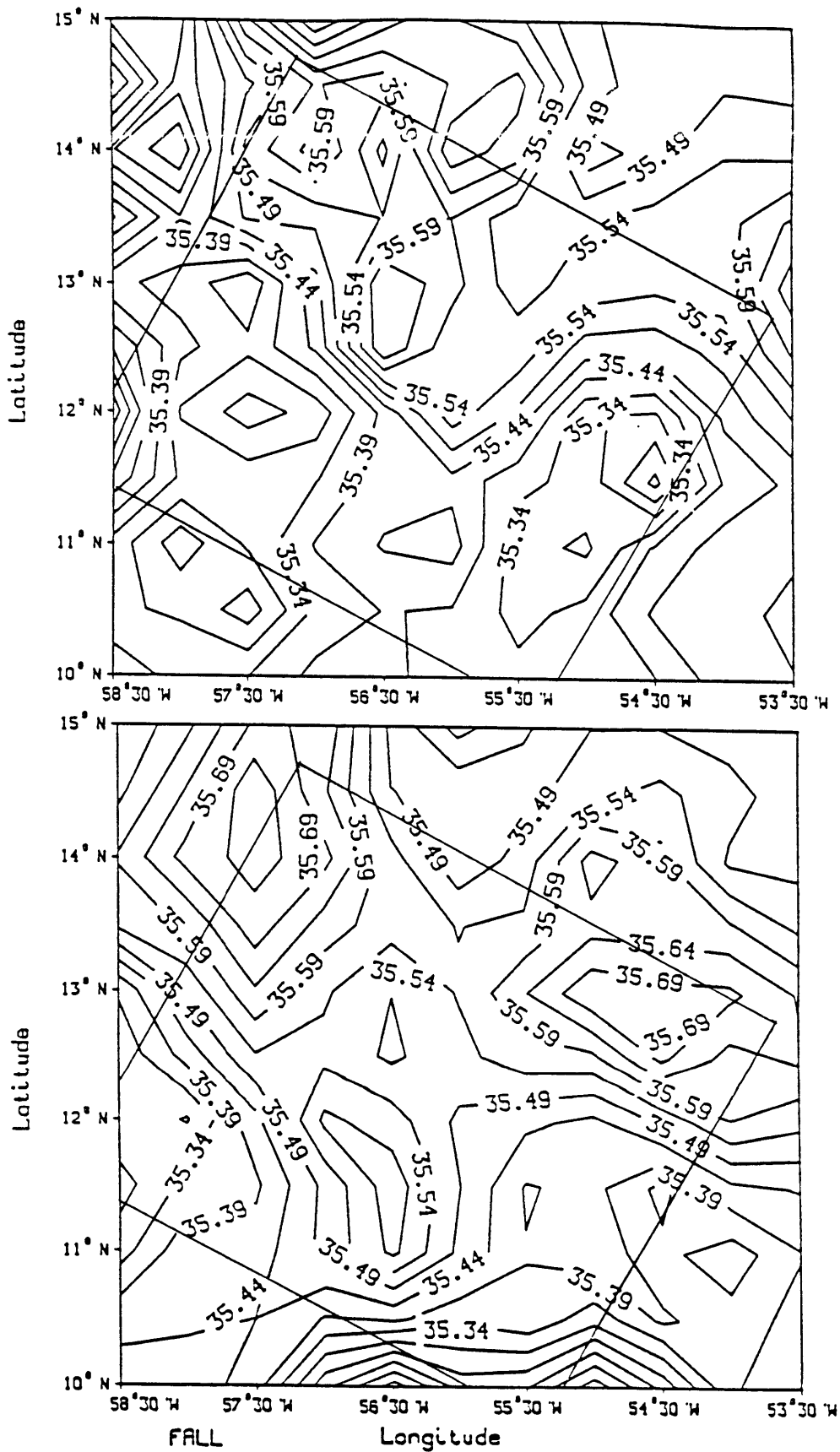


Figure 17. Salinity on sigma theta 26.9 for spring (upper) and fall (lower).

at corresponding depths on isobars, hence are not shown. The velocity shear between sigma theta 26.9 and 27.1 (staircase depths) is generally less than 2 cm/s in both the spring and fall.

2.4. Current Meter Data

The mooring, located at approximately the center of the CTD survey grid, contained 8 current meters within the step region, 335 and 415 m, with 2 additional meters at 170 m and 850 m. Progressive vector diagrams constructed by H. Perkins of NORDA for the 350m and 850m records are shown in figure 18. The 8 closely spaced current meters showed very little shear, hence the 350m record is quite representative. The deep record is also coherent in direction with the shallower ones, but the currents generally have slightly smaller amplitudes than the shallower ones. The most striking feature of the current meter records is the strong time variability. This result emphasizes the obvious difficulty in trying to incorporate such data into a steady state model. In trying to select the most appropriate time interval over which to average the data for the inversion, we see that not only the duration, but the starting point of the average will determine the values we obtain.

We have considered three of the many possible schemes for temporally averaging the current meter data, and tabulate the velocities and standard deviations obtained with each averaging scheme in table 1. The first method is to average over the time during which the CTD surveys were done, giving an 11 day average in the spring (while the spring survey took 18 days, only the last 11 days coincided with current meter operation) and a 13 day average in the fall.

Another possible averaging scheme is to choose a time interval by scaling arguments to correspond to the 100 km smoothing of the hydrographic data. With velocities of about 5 cm/s, this time interval is approximately 30 days, and the starting time was chosen to center the interval about the CTD survey as much as possible. This procedure

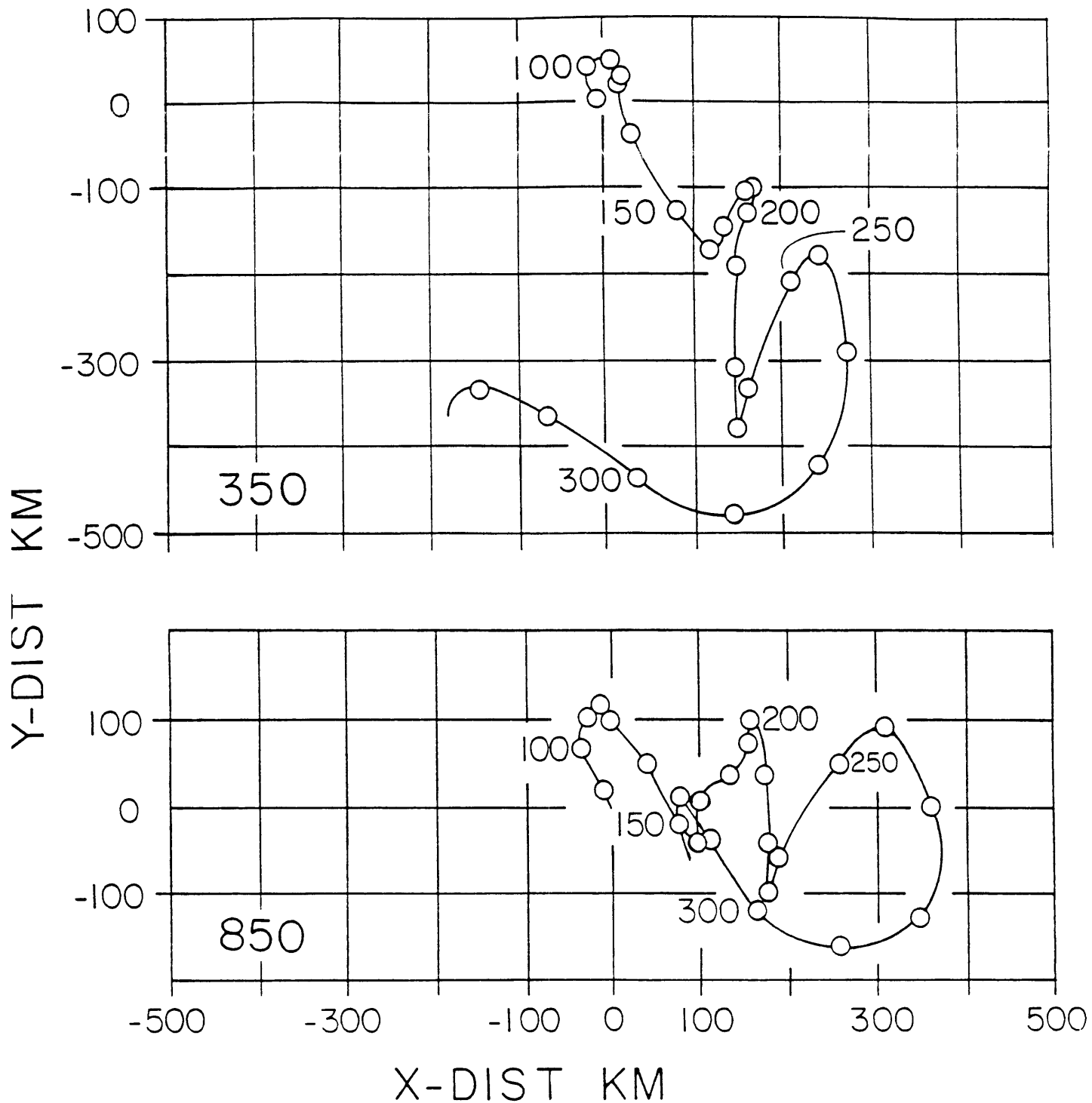


Figure 18. Progressive vector diagrams for the duration of the current meter records at depths of 350 and 850 m. Squares mark 50 day intervals from starting day 85 to ending day 329. CTD surveys ran from days 78–96 in the spring, and from days 303–316 in the fall. (Figure courtesy of H. Perkins.)

Time Interval	350 m	415 m	850 m
	U , V	U , V	U , V
Spring 30 day	1(\pm 4) , 1(\pm 4)	1(\pm 3) , 2(\pm 4)	0(\pm 3) , 4(\pm 3)
Spring 11 day	-2(\pm 3) , 1(\pm 5)	-2(\pm 2) , 3(\pm 4)	-2(\pm 2) , 6(\pm 3)
Fall 30 day	-13(\pm 5) , 5(\pm 7)	-16(\pm 5) , 7(\pm 9)	-8(\pm 4) , 6(\pm 6)
Fall 13 day	-11(\pm 4) , 6(\pm 5)	-16(\pm 3) , 10(\pm 5)	-6(\pm 4) , 10(\pm 6)
Whole Record	-1(\pm 6) , -2(\pm 9)	-2(\pm 8) , -2(\pm 11)	0(\pm 5) , 0(\pm 8)

Table 1. Current meter velocities at depths 350, 415 and 850 m using the 3 averaging schemes discussed in the text. Standard deviations are given in parenthesis. Values at 350 m are an average over the 6 instruments between 335 and 365 m. (data courtesy of H. Perkins of the Naval Ocean Research and Development Activity)

gives very small spring velocities since the current frequently changes direction, and large fall velocities nearly identical to the 13 day average, since the currents are steadily northwestward over that interval.

The third interval considered was an average over the entire 244 days of the current meter records. This gives much smaller velocities which are more consistent with the magnitude of the thermal wind velocities, but it is not apparent from the current meter records that even such a long interval represents any real steady state average.

None of these averaging intervals is entirely satisfactory. The long time average is probably not appropriate since both spring and fall CTD surveys resolve individual eddies, yet the 244 day interval gives velocities averaged over the passage of several eddies. We find that with the large variances obtained using this averaging interval, the current meter observations are not significantly different from the solutions found without current meter constraints. The same was true for the short term averages in the spring. In the fall however, the eddy persisting over the mooring for over 30 days has significantly larger velocities than the relative geostrophic velocities found at the site (compare figure 13 with table 1). Reference level velocities of 6 to 10 cm/s are required to satisfy the current meter constraints. Inversions described in section 3.4

indicate that these current meter data may not be consistent with a steady state model and the 100 km smoothing of the hydrographic data.

Chapter 3. Cartesian Inversions

3.1 Model Dynamics

The basic idea employed is to construct the simplest steady state advection–diffusion model which is geostrophic, mass conserving, and is consistent with all tracer and velocity measurements. By incorporating the required constraints on the velocity field into the tracer advection–diffusion balance, we form a linear system of equations in the reference level velocities and diffusivities, which can be solved by standard linear inverse methods. Except for the addition of diffusivity, the formulation of the equations is similar to that used by Wunsch (1978).

The dynamics imposed are the geostrophic balance

$$\begin{aligned}fu &= -\frac{1}{\rho_0}p_y \\fv &= \frac{1}{\rho_0}p_x\end{aligned}\tag{3.1}$$

which with the hydrostatic balance

$$p_z = -g\rho$$

yields the thermal wind equations

$$\begin{aligned}u_z &= \frac{g}{f\rho_0}\rho_y \\v_z &= -\frac{g}{f\rho_0}\rho_x.\end{aligned}\tag{3.2}$$

We also require mass conservation

$$u_x + v_y + w_z = 0.\tag{3.3}$$

The linear vorticity balance,

$$\beta v = f w_z\tag{3.4}$$

must also hold since it is derived from (3.1) and (3.3).

The steady state advection-diffusion balance for temperature T , (and similarly for salinity) can be written using (3.3) in the form

$$\nabla \cdot (\underline{u}T) - \nabla \cdot (\kappa^T \cdot \nabla T) = 0 \quad (3.5)$$

The tensor form is used for the diffusivities to allow parameterization of along and across isopycnal components rather than just horizontal and vertical. The elements of the diffusivity tensor can be written (Olbers et al., 1985) as

$$\kappa_{ij}^T = A_i^T \delta_{i,j} + (A_c^T - A_i^T) D_{ij}$$

where

$$D_{ij} = \frac{\partial_i \sigma \partial_j \sigma}{|\partial \sigma|^2}.$$

A_i^T and A_c^T are along and across isopycnal diffusivities of heat, and $\partial_i \sigma$ is the i^{th} derivative of potential density. The diffusivity can be allowed to vary vertically.

The velocity field is divided into relative and reference components,

$$\begin{aligned} u &= u_0(x, y, z_0) + u_{rel} \\ v &= v_0(x, y, z_0) + v_{rel} \end{aligned} \quad (3.6)$$

and the advection by the relative parts, which are derived from the density fields, are moved to the right hand side of equation (3.5) to form a linear equation for the reference velocities.

It is convenient to also define a w_{rel} , which contains the vertical structure of w obtained from the relative horizontal velocities, eliminating the need to solve for w at each level. Vertical velocity can be partitioned in either of two ways, depending on whether it is computed from the continuity equation, (3.3) or from the linear vorticity balance, (3.4). Which ever way w is obtained, an additional constraint on the horizontal reference level velocities will be needed to insure that all constraints, (3.1), (3.3) and (3.4), are satisfied by the total velocity field.

Method 1:

w is computed from the continuity equation,

$$(u_x + v_y + w_z) = 0.$$

Integrating over z and using (3.6), this gives

$$w = w_{ref}(x, y, z_0) - (u_{0,x} + v_{0,y})(z - z_0) - \int_{z_0}^z (u_{rel,x} + v_{rel,y}) dz$$

from which we can define

$$\begin{aligned} w_0 &\equiv w_{ref} - (u_{0,x} + v_{0,y})(z - z_0) \\ w_{rel} &\equiv - \int_{z_0}^z (u_{rel,x} + v_{rel,y}) dz. \end{aligned} \quad (3.7)$$

The total velocity field (relative plus reference) then identically satisfies the continuity equation, but not necessarily the linear vorticity equation (3.4), which using (3.6) and (3.7) can be written as

$$\beta(v_0 + v_{rel}) = f(w_0 + w_{rel})_z. \quad (3.8)$$

Notice that by the thermal wind equations (2.6), the relative velocities separately satisfy the vorticity equation,

$$u_{rel,x} + v_{rel,y} = \frac{g\beta}{\rho f^2} \int_{z_0}^z \rho_x dz = -\frac{\beta}{f} v_{rel},$$

so that from (3.7),

$$\beta v_{rel} = f w_{rel,z}. \quad (3.9)$$

Substituting (3.7) into (3.8), then subtracting off (3.9), we find

$$\beta v_0 = -f(u_{0,x} + v_{0,y}) \quad (3.10)$$

is the necessary additional constraint on the reference velocities.

Method 2:

w is computed from the vorticity balance,

$$\beta v = f w_z.$$

Integrating in z and using (3.6), we get

$$w = w_{ref}(x, y, z_0) + \frac{\beta}{f} v_0 (z - z_0) + \int_{z_0}^z \frac{\beta}{f} v_{rel} dz$$

from which we can define

$$\begin{aligned} w_0 &\equiv w_{ref} + \frac{\beta}{f} v_0 (z - z_0) \\ w_{rel} &\equiv \int_{z_0}^z \frac{\beta}{f} v_{rel} dz. \end{aligned} \tag{3.11}$$

With w computed from (3.11), the total velocity field then identically satisfies the vorticity equation, but does not automatically satisfy the continuity equation. We therefore need to require

$$(u_0 + u_{rel})_x + (v_0 + v_{rel})_y + (w_0 + w_{rel})_z = 0. \tag{3.12}$$

Substituting (3.11) and (3.9) into (3.12), we find the constraint on the horizontal reference velocities is again equation (3.10).

Although it may appear that the second method is preferable since it avoids differentiation of the horizontal velocities, it is shown in the next section that in the finite difference formulation these methods are essentially equivalent. In this study, w will be obtained from the continuity equation. Since we are using the flux form (3.5) of the tracer equations (that is, $\nabla \cdot (\underline{u}T)$ rather than $\underline{u} \cdot \nabla T$) it seems that mass should be balanced exactly before we attempt to reduce the tracer imbalances in the inversion. Any mass imbalance would also cause apparent tracer imbalances.

With the velocity field separated into relative and reference parts, the tracer equations (3.5) are now linear in the unknowns, u_0 , v_0 , w_{ref} , A_i^T and A_c^T . With the

integrated form of the equations, the finite difference formulation is exactly mass conserving. Using the Divergence Theorem and the definition of the diffusivity tensor, (3.5) becomes

$$\oint_{boundary} (\underline{u}_0 T) \cdot ds - \oint_{boundary} \left[A_i^T (\delta_{ij} - D_{ij}) + A_c^T D_{ij} \right] \frac{\partial T}{\partial x_j} ds_i = - \oint_{boundary} (\underline{u}_{rel} T) \cdot ds. \quad (3.13)$$

We will have one equation of the form (3.13) for each tracer in each box at each level. There is also one constraint equation of the form (3.10) for each horizontal location:

$$\iiint \beta v_0 dx dy dz = - \iiint f(u_{0,x} + v_{0,y}) dx dy dz. \quad (3.14)$$

Current Meter Constraint Equations

In this section we describe how the velocities measured at the current meter mooring are included as an additional constraint on the reference level velocities at surrounding points. We require that the total velocity field (relative plus reference), when interpolated to the location of the mooring, be consistent with the current meter observations. The interpolation is done by objective mapping as for the tracer fields.

At the current meter location, \underline{x}_{cm} , the velocity is the sum of the relative and reference velocities:

$$\begin{aligned} u_{rel}(\underline{x}_{cm}) + u_0(\underline{x}_{cm}) &= u(\underline{x}_{cm}) \\ v_{rel}(\underline{x}_{cm}) + v_0(\underline{x}_{cm}) &= v(\underline{x}_{cm}). \end{aligned} \quad (3.15)$$

Expressing $u_{rel}(\underline{x}_{cm})$ and $u_0(\underline{x}_{cm})$ as a linear combination of the surrounding points, the expression for u at each depth (and similarly for v) is (again following Bretherton et al., 1976)

$$\begin{aligned} u_{rel}(\underline{x}_{cm}) &= \bar{u} + \sum_i \sum_j C_i F_{ij}^{-1} (u_{rel}(x_j) - \bar{u}) \\ u_0(\underline{x}_{cm}) &= \sum_i \sum_j C_i F_{ij}^{-1} u_0(x_j). \end{aligned} \quad (3.16)$$

where the sum is over gridpoints lying within 2 correlation length scales of the mooring. \bar{u} is the objective mean (2.2) of the relative velocity at each depth, and C_i and F_{ij} are expected products as in equations (2.3) and (2.4). Here C is a vector since we are only interpolating to one point, the mooring location. The correlation length scale was again chosen to be 100 km in keeping with the tracer length scale. Substituting (3.16) into (3.15), we get equations for the observed current meter velocities in terms of the relative and reference velocities at grid locations. The constraint equations then can be written, putting the unknown reference velocities on the left hand side and the known relative velocities and current meter velocities on the right hand side, as

$$\begin{aligned} \sum_i \sum_j C_i F_{ij}^{-1} u_0(\underline{x}_j) &= - \sum_i \sum_j C_i F_{ij}^{-1} (u_{rel}(\underline{x}_j) - \bar{u}) + u(\underline{x}_{cm}) - \bar{u} \\ \sum_i \sum_j C_i F_{ij}^{-1} v_0(\underline{x}_j) &= - \sum_i \sum_j C_i F_{ij}^{-1} (v_{rel}(\underline{x}_j) - \bar{v}) + v(\underline{x}_{cm}) - \bar{v}. \end{aligned} \quad (3.17)$$

Two equations of the form (3.17) are written for each depth where we wish to impose current meter constraints. We have vertically averaged the velocities over the 8 instruments between 265 m and 380 m, and impose constraints at levels 350 m, 400 m and at 800 m.

Equations (3.13), (3.14) and (3.17) are written matrix form as $A\underline{y} = \underline{b}$, where \underline{y} is comprised of the reference velocities and diffusion coefficients, A is the matrix of coefficients, and \underline{b} contains the advection by the relative velocities. The equations are written in finite difference form in section 3.2.

3.2 Finite Difference Formulation

In this section capital letters will refer to the velocities computed on the grid. Referring to figure 7, the horizontal relative geostrophic velocities are computed as follows:

$$\begin{aligned}
 U_{relE} &= \frac{g}{\rho_0 f_M} \frac{(\int \rho_1 - \int \rho_2)}{\Delta Y} \\
 U_{relW} &= \frac{g}{\rho_0 f_M} \frac{(\int \rho_4 - \int \rho_3)}{\Delta Y} \\
 V_{relN} &= -\frac{g}{\rho_0 f_N} \frac{(\int \rho_1 - \int \rho_4)}{\Delta X_N} \\
 V_{relS} &= -\frac{g}{\rho_0 f_S} \frac{(\int \rho_2 - \int \rho_3)}{\Delta X_S}
 \end{aligned} \tag{3.18}$$

where

$$\int \rho_i \equiv \sum_{k=k_{z_0}}^{k_*} \rho(z_k) dz_k$$

and i denotes the edge; $i = 1$ in the northeast corner and increases clockwise.

Finite difference forms for calculating W_{rel} by each method are given to demonstrate that they are equivalent.

Method 1):

$$(W_{relU} - W_{relL}) \Delta X_M \Delta Y = -(U_E - U_W) \Delta Y \Delta Z - (V_N \Delta X_N - V_S \Delta X_S) \Delta Z.$$

Using definitions (3.18) and rearranging gives

$$\begin{aligned}
 W_{relU} - W_{relL} &= \frac{g \Delta Z}{\rho_0 \Delta X_M \Delta Y} \left[\frac{\int \rho_1 (-f_N + f_M)}{f_M f_N} + \frac{\int \rho_2 (-f_M + f_S)}{f_M f_S} \right. \\
 &\quad \left. + \frac{\int \rho_3 (f_M - f_S)}{f_M f_S} + \frac{\int \rho_4 (f_N - f_M)}{f_M f_N} \right].
 \end{aligned}$$

Method 2):

$$\frac{W_{relU} - W_{relL}}{\Delta Z} = \frac{\beta}{f_M} \frac{(V_N + V_S)}{2}.$$

Using (3.14), this becomes

$$W_{relU} - W_{relL} = \frac{\beta \Delta Z}{2} \left[\frac{-\int \rho_1}{f_M f_N \Delta X_N} + \frac{-\int \rho_2}{f_M f_S \Delta X_S} + \frac{\int \rho_3}{f_M f_S \Delta X_S} + \frac{\int \rho_4}{f_M f_N \Delta X_N} \right].$$

We see that the difference between the two methods amounts to the approximations, $\Delta X_N \approx \Delta X_M$ and $\beta \approx (f_N - f_M)/(\Delta Y/2)$ at the northern edge of the cell, and at the southern edge, $\Delta X_S \approx \Delta X_M$ and $\beta \approx (f_M - f_S)/(\Delta Y/2)$, and therefore they are numerically equivalent.

The finite difference form of the tracer balance equations (3.13) with constant cross-isopycnal diffusivity is as follows:

$$\begin{aligned}
& [(U_0 T)_E - (U_0 T)_W] \Delta Y \Delta Z + [(V_0 T)_N \Delta X_N - (V_0 T)_S \Delta X_S] \Delta Z \\
& + [(W_0 T)_U - (W_0 T)_L] \Delta X_M \Delta Y \\
& - A_{Tc} \left[[(D_{xx} T_x + D_{xy} T_y + D_{xz} T_z)_E \right. \\
& \quad - (D_{xx} T_x + D_{xy} T_y + D_{xz} T_z)_W] \Delta Y \Delta Z \\
& \quad - [(D_{yx} T_x + D_{yy} T_y + D_{yz} T_z)_N \Delta X_N \\
& \quad \quad - (D_{yx} T_x + D_{yy} T_y + D_{yz} T_z)_S \Delta X_S] \Delta Z \\
& \quad - [(D_{zx} T_x + D_{zy} T_y + D_{zz} T_z)_U \\
& \quad \quad - (D_{zx} T_x + D_{zy} T_y + D_{zz} T_z)_L] \Delta Y \Delta X_M \left. \right] \\
& = [(U_{rel} T)_E - (U_{rel} T)_W] \Delta Y \Delta Z + [(V_{rel} T)_N \Delta X_N - (V_{rel} T)_S \Delta X_S] \Delta Z \\
& \quad + [(W_{rel} T)_U - (W_{rel} T)_L] \Delta X_M \Delta Y.
\end{aligned} \tag{3.19}$$

Capital subscripts, N,S,E,W,U and L indicate the side on which the quantity is evaluated and small subscripts, x,y and z denote (finite difference) derivatives which are not written out explicitly. Vertical variation in diffusivity can be represented by a sum of Chebyshev polynomials replacing the constant diffusivities in (3.19),

$$A_c^T(z) = \sum_{l=0}^L a_l T_l(z).$$

The finite difference form of the vorticity equation constraint, (3.14), is after slight rearrangement

$$\begin{aligned}
& (U_{0E} - U_{0W}) \Delta Y \Delta Z + V_{0N} \left(\frac{\beta}{2f_M} \Delta X_M \Delta Y \Delta Z + \Delta X_N \Delta Z \right) \\
& + V_{0S} \left(\frac{\beta}{2f_M} \Delta X_M \Delta Y \Delta Z + \Delta X_S \Delta Z \right) = 0.
\end{aligned} \tag{3.20}$$

(3.19) and (3.20) and the current meter constraint equations, (3.17) are the equations to be inverted for the reference velocities and diffusivities.

3.3 The SVD Solution

The constraint equations, (3.13), (3.14) and (3.17), are combined into a linear system of m equations in the n unknown reference velocities and diffusivities, and written in matrix form as

$$A\mathbf{y} = \mathbf{b}.$$

\mathbf{y} is a column vector composed of U_0 , V_0 , and W_{ref} at each horizontal location, and the diffusion coefficients A_c^T and A_l^T . The solution is obtained by singular-value decomposition, which for underdetermined systems provides the minimum length solution, that is, no structure is introduced which is not required by the data. The advantage of singular-value decomposition is that in addition to the solution and an estimate of its variance, one also obtains detailed information about how well individual variables can be resolved and which equations provide the most information.

Before solving, the matrix must be normalized to prevent unintentional emphasis on a particular variable or equation. The inversion procedure will preferentially adjust parameters with large coefficients, and will more exactly satisfy equations with large coefficients. The columns are therefore normalized by the inverse of the square root of the column length to encourage the (weighted) solution to come out to be order 1, and the rows are nondimensionalized by dividing by the row length.

The matrix can then be systematically weighted by column and row. The matrix was weighted by column to reflect the expected size of each parameter so that within each equation, the coefficients are all the same order of magnitude. This way, no one variable dominates the solution. In this problem w_{ref} was weighted by 10^{-4} , and u_{ref} , v_{ref} and A_c were weighted by 1. In experiments using horizontal diffusion, A_l was weighted by 10^6 . The equations are weighted by row according to the confidence one

has in each constraint. The tracer balance equations have been given equal weight since there was no apriori reason to prefer a particular tracer or particular depth. The vorticity constraint was also weighted by 1. Where current meter constraints were used, those equations were weighted by 0.5 to reflect the large variances in the current meter observations.

The mathematics of SVD is derived in detail in Lanczos (1961) and in Wunsch (1978) so we will only outline it here. The basic idea is that the matrix A can be decomposed into the product of 3 matrices, $A = U\Lambda V^T$, where the U matrix is composed of the m eigenvectors, \underline{u}_i , of the $m \times m$ matrix AA^T , the V matrix is composed of the n eigenvectors, \underline{v}_i , of the $n \times n$ matrix $A^T A$, and Λ is a diagonal matrix containing the k nonzero eigenvalues, λ_i , of the coupled U - V system, in order of decreasing magnitude. Since the \underline{v}_i span the n dimensional solution space, the solution, $\hat{\underline{y}}$ can be expressed as their linear combination. The solution can be written in the form (Wunsch, 1978)

$$\hat{\underline{y}} = \sum_{i=1}^k \frac{U_i^T \cdot \underline{y}}{\lambda_i} \underline{v}_i + \sum_{i=k+1}^n \alpha_i \underline{v}_i. \quad (3.21)$$

The solution is constructed by a summation over terms of increasingly complex structure, over the k terms corresponding to the k nonzero eigenvalues. In practice, with noise in the system, the eigenvalues never reach zero and one must choose a cutoff value for the summation, that is, an “effective” rank of the system. The second summation, over $i = k + 1, n$, contains that part of the solution proportional to the \underline{v}_i which are orthogonal to the matrix A , ie, about which A has no information, hence (in the absence of inequality constraints) is set equal to zero for the minimum length solution. k is chosen by balancing the increasing variance of the solution with the successively better fit of the solution to the equations. The residuals, \underline{r} , defined as $\underline{r} \equiv A\hat{\underline{y}} - \underline{b}$, provide a measure of how well the solution satisfies the constraint equations. Each additional term reduces the residuals, but at the expense of increased variance of the solution due to noise in the observations. The choice of effective rank was made by

plotting the average residuals (for all the equations) versus the average variance (for all the variables) and looking for the optimal rank with regard to residuals and error. In the next two subsections we discuss how the solution variance is defined and what constitutes an acceptable level of residuals.

Solution Variance

The variance of the solution has two contributions, that due to noise in the data, and that due to incomplete resolution. With three assumptions about the noise field, that the noise has zero mean, is uncorrelated from measurement to measurement and has average standard deviation of σ , Wiggins (1972) has shown that the variance of the estimate \hat{b} of the p^{th} variable due to noise in the observations can be expressed as

$$\langle (\hat{b}_p - b_p)^2 \rangle = \sigma^2 \sum_{i=1}^k \frac{V_{pi}^2}{\lambda_i^2} \quad (3.22)$$

where σ^2 can be estimated from the residuals \underline{r} at rank k as

$$\sigma^2 = \frac{|\underline{r}|^2}{m - k}.$$

Note that the variance due to noise becomes increasingly magnified (as $1/\lambda_i^2$) as the summation progresses.

The resolution matrix VV^T provides a measure of how well individual parameters are resolved, that is, whether they are being determined individually or in combination with other nearby parameters (see Wiggins, 1972 or Wunsch, 1978). The resolution of a particular variable is indicated by the corresponding diagonal term in VV^T . A value of 1 on the diagonal signifies perfect resolution of that variable. The error due to failure to resolve can be expressed as

$$\langle (\hat{b} - b)^2 \rangle = [(VV^T - I)b_{true}]^2 \quad (3.23)$$

where the magnitude of b_{true} can be assumed to be of order 1, since the matrix has been weighted for this result. The closer that VV^T is to the identity matrix, I , the

Depth	Expected Error	Eddy Variability	Seasonal Variability
	$\Delta T, \Delta S$	$\Delta T, \Delta S$	$\Delta T, \Delta S$
250	2.1, .35	2.0, .50	-1.0, -.20
350	1.2, .20	1.5, .30	-.5, -.10
400	.8, .10	1.0, .20	-.4, -.05
500	.7, .10	1.0, .15	-.4, -.06
700	.4, .02	.5, .05	-.1, .00
800	.2, .01	.4, .02	-.2, -.01

Table 2: Expected magnitude of temperature and salinity residuals as a function of depth (computed in the appendix). Also tabulated are expected error in the equations from the eddy time variability (estimated from the tracer maps) and the long term time variability (from differences in the mean temperature and salinity from spring to fall) at each depth.

smaller the resolution error. The total solution variance then is the sum of the two effects, (3.22) and (3.23):

$$\langle (\hat{b}_p - b_p)^2 \rangle = \sigma^2 \sum_{i=1}^k \frac{V_{pi}^2}{\lambda_i^2} + [(VV^T - I)b_{true}]^2 \quad (3.24)$$

We choose the effective rank, k , such that the standard deviation of the solution is generally smaller than the magnitude of the solution, to the extent that the data will permit.

Residuals

Ideally, for a steady state problem with no errors in the observations, the residuals could be reduced to zero by a model incorporating all relevant dynamics. However the errors in the CTD data, and consequently in the relative velocity field will produce irreducible residuals. The expected size of these residuals due to observational error is estimated in the appendix, and tabulated as a function of depth in table 2. Residuals of the conservation equations are expressed in terms of the temperature and salinity imbalances (in degrees and ppt) which would accumulate over 6 months per unit volume.

For a term to be neglected in the advection–diffusion equation, it must be smaller in magnitude than the expected error, that is, below the noise level. The validity of neglecting the time derivative term can be examined by estimating the contributions from both the seasonal change in the average tracer fields, and the local change due to eddies. The seasonal average change is only about half the expected error and is therefore probably negligible (table 2), but the eddy variability is about the same magnitude as the expected error and may be significant in the advection–diffusion equation. At 400 m depth, the expected residuals due to error are about 0.8 degrees and 0.08 ppt over 6 months, while the possible change in the temperature and salinity fields due to an eddy passing through the control volume is about 1 degree and .2 ppt. The values of eddy variability in table 2 are probably upper bounds since they were estimated using the strongest gradients in the mapped region. Since we have no information about the paths of individual eddies, we omit the time derivative term, but must check the validity of any steady state solution by making certain that the final residuals are consistent with the original assumptions. We check that the temperature and salinity residuals are randomly distributed in space about a zero mean. Structure remaining in the residuals after the inversion signifies that the model is not including all the relevant dynamics. We also average the residuals for each tracer at each depth and compare the resultant standard deviations with the expected error in the equations given in table 2. The magnitudes must be comparable for an acceptable solution.

3.4. Results of Inversions

Six levels were chosen for evaluation of the tracer balances. Additional levels were found to be redundant. The levels used are centered at 250, 350, 400, 500, 700 and 800 db (figure 19). This distribution avoids the upper layers which may be affected by unknown surface fluxes, and gives good coverage in the step region and in the Antarctic Intermediate water below. The 350 and 400 db levels were chosen because the current meter records suggested that there might be significant shear in this pressure interval, but were actually found to provide redundant information in the inversions.

Our starting model which will be adjusted by the inversion procedure is that of zero reference level velocities. Values of the horizontally averaged temperature and salinity residuals at each level are given for this initial model for spring and fall data sets in table 3. Comparing the standard deviation of the starting residuals with the expected error at each depth (table 2), it is clear that the starting model generates unacceptably large residuals distributed about a large negative mean. The data requires, at the least, a non-zero reference level velocity. The spring initial residuals are somewhat larger than the fall residuals, indicating that larger adjustments to the initial model are required. The results from the fall and spring data sets will be presented separately.

We will present the results of 3 inversions for the fall data set, and 2 for the spring. The first model for each data set will be adiabatic, that is without diffusivities. The residuals are checked for consistency with the original assumptions, that is, a random distribution about zero mean and an average magnitude consistent with the estimated error in the original equations. Solutions will then be sought with vertically varying cross isopycnal diffusivities of heat and salt. Finally, for the fall data set, solutions with the addition of the 30 day averaged current meter constraints will be presented.

Fall Solutions

Temperature and salinity balances in 9 boxes (shown in figure 6) at 6 depths along with 1 vorticity constraint in each box gives a system of 117 equations in 34 unknown

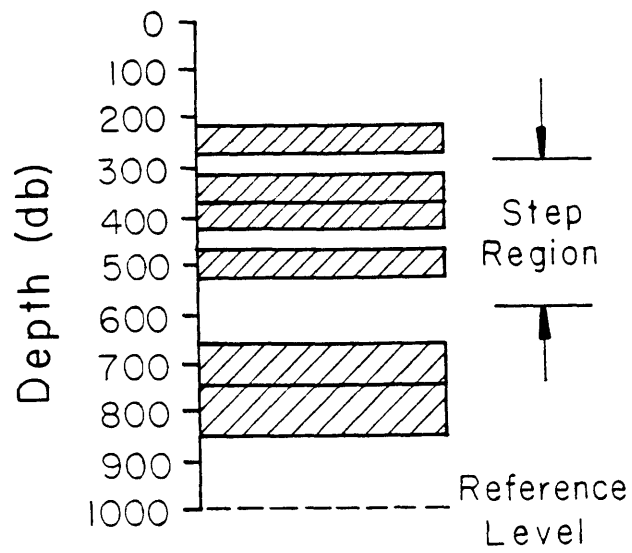


Figure 19. Profile of grid on which tracer balances were evaluated.

Fall

Depth	T Residuals	S Residuals
250	-1.49 (6.79)	-.32 (1.31)
350	-1.39 (4.02)	-.27 (.74)
400	-1.46 (2.98)	-.26 (.53)
500	- .69 (2.12)	-.10 (.36)
700	- .31 (.90)	-.05 (.10)
800	- .08 (.69)	.01 (.10)

Spring

250	-4.86 (8.61)	-.89 (1.64)
350	-3.92 (6.69)	-.69 (1.23)
400	-4.20 (5.57)	-.79 (1.09)
500	-1.68 (2.16)	-.39 (.49)
700	- .43 (1.92)	-.11 (.23)
800	- .10 (1.60)	-.02 (.19)

Table 3: Initial residuals for fall and spring data sets. Standard deviations given in parentheses.

reference velocities. For the first solution found, the adiabatic one, the effective rank of the system was chosen to be 31. Resolution of all the variables, as measured by diagonal elements of VV^T (equation 3.23), is close to 1 (in general, $\geq .8$).

The horizontal reference level velocities and their standard deviations from (3.24) are shown along with the total velocity field at 400 db in figure 20. Reference level velocities in general act to reduce the largest geostrophic velocities at 400 db (compare figure 20 with figure 13). The balance of terms in the temperature and salinity equations averaged over all the boxes is shown in figure 21. The balance is such that the sum of the horizontal advection terms (term 3) balances the vertical advection (term 4), leaving spatially averaged residuals (squares) distributed about small mean values (compared to the estimated error in table 3). This average profile of the terms is quite representative of the balance in any individual box. The final distribution of residuals appears to be randomly distributed in space. Profiles of the final residuals of the temperature

equations (salinity residuals are similarly distributed) are shown for each of the 9 boxes in figure 22. The standard deviations of the temperature and salinity residuals at each depth are shown in figure 23 and appear to be consistent with the expected error in table 2.

Although the balance of terms is between horizontal and vertical advection, vertical velocities individually have very large error bars (figure 24). We found vertical velocities between 10^{-4} and 10^{-3} cm/s , one to two orders of magnitude larger than the value that Lambert and Sturges (1977) assumed for their estimates of the advection–diffusion balance in the Caribbean. But variances of the vertical velocities, (coming about equally from the variance on w_0 , equation (3.24), and from the error in w_{rel} estimated in the appendix) are so large as to make the values generally indistinguishable from zero. At the chosen rank, the diagonal elements of VV^T corresponding to w_0 are near 1, signifying that vertical velocity is well resolved. However, examination of VV^T at earlier ranks shows that the horizontal reference velocities are almost completely resolved before the vertical velocity enters the solution. Vertical velocity in this formulation is used to further reduce the residuals that remain after the horizontal velocities are determined.

Although the adiabatic solution seems to be consistent with the data used, we will add to the model vertically varying cross–isopycnal diffusivities to compare their magnitude with previous estimates. The addition of six Chebyshev polynomials (0th through 5th order) for both the heat and salt diffusivities adds 12 unknowns, for a system of 117 equations in 46 unknowns. The effective rank is increased to 39. The solution for horizontal reference velocities is practically indistinguishable from the adiabatic case so is not shown. The balance of terms in the advection – diffusion equation (figure 25) is slightly altered, with the vertical advection term reduced in magnitude and about the same size as the cross–isopycnal diffusivity. Although the vertical velocities are slightly smaller in this diffusive model, the error bars are even larger. The diffusivity

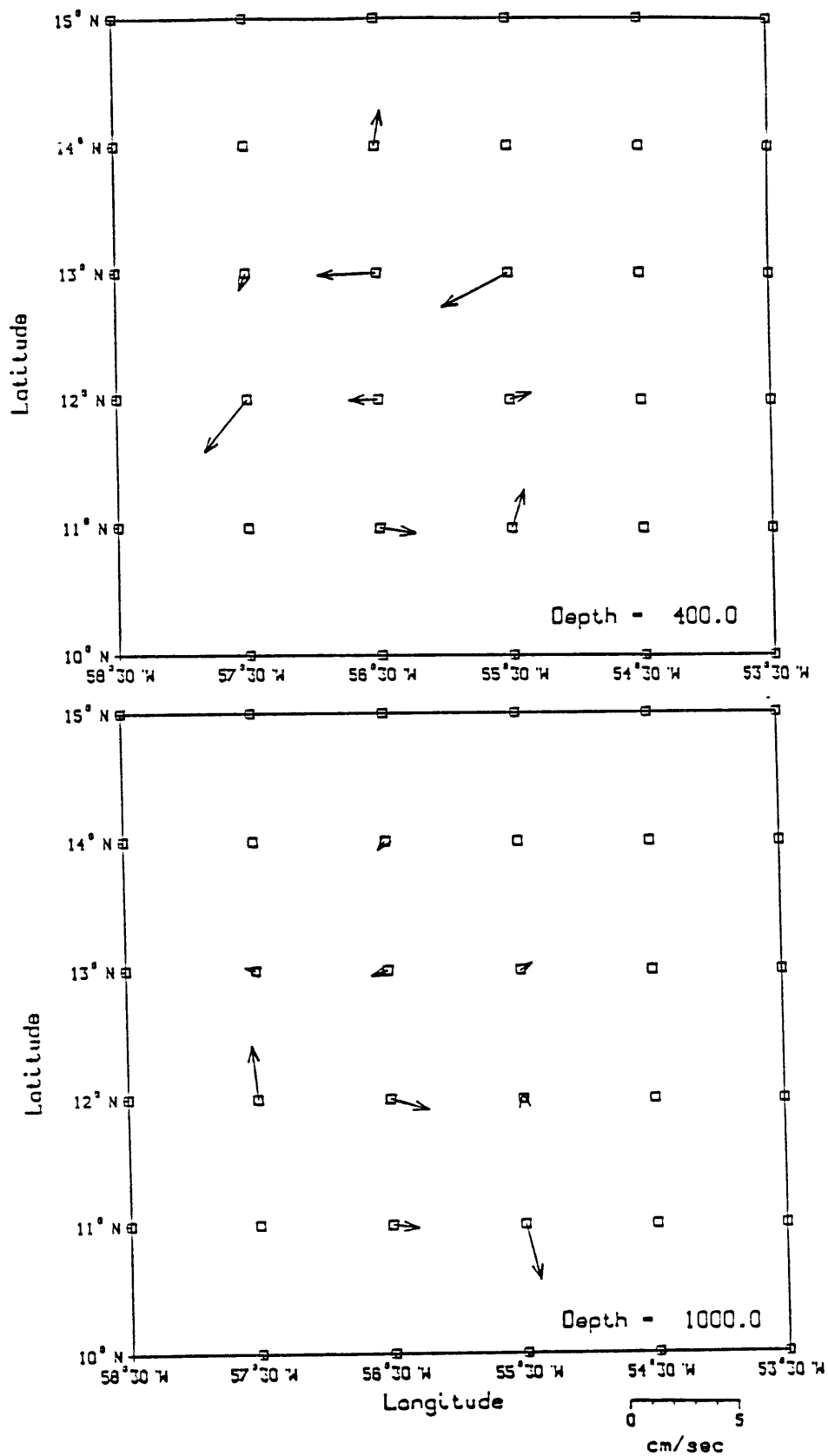


Figure 20. Fall reference level velocities and velocities at 400 db for adiabatic solution. Standard deviations of the reference velocities are generally about 0.2–0.6 cm/s.

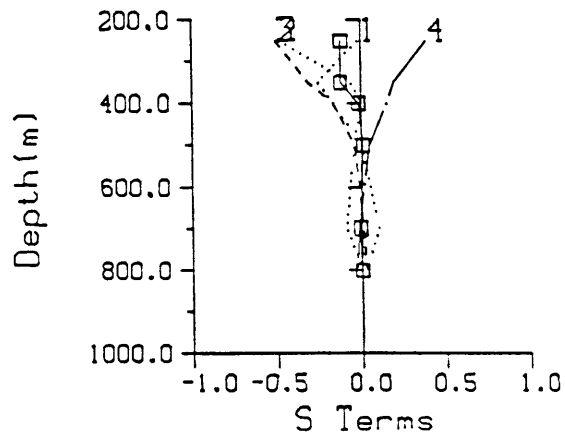
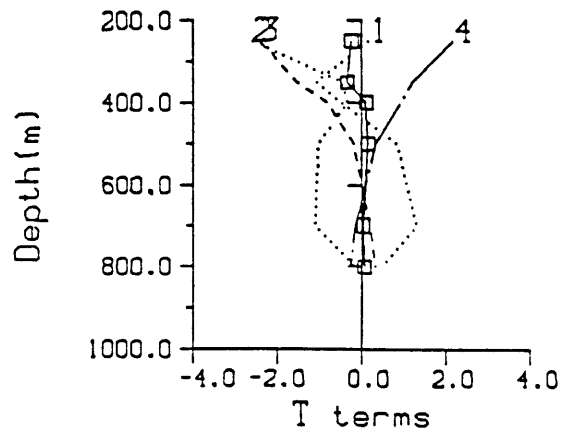


Figure 21. Balance of terms in the T and S equations averaged over the 9 balance boxes for fall, adiabatic model. Dimensions are degrees and ppt accumulating over 6 months per unit volume. Positive values correspond to cooling and freshening. 1(dotted) =eastward advection, 2(dotted) =northward advection, 3(dashed) =total horizontal advection, 4(dash dot) =vertical advection. Residuals are marked by squares.

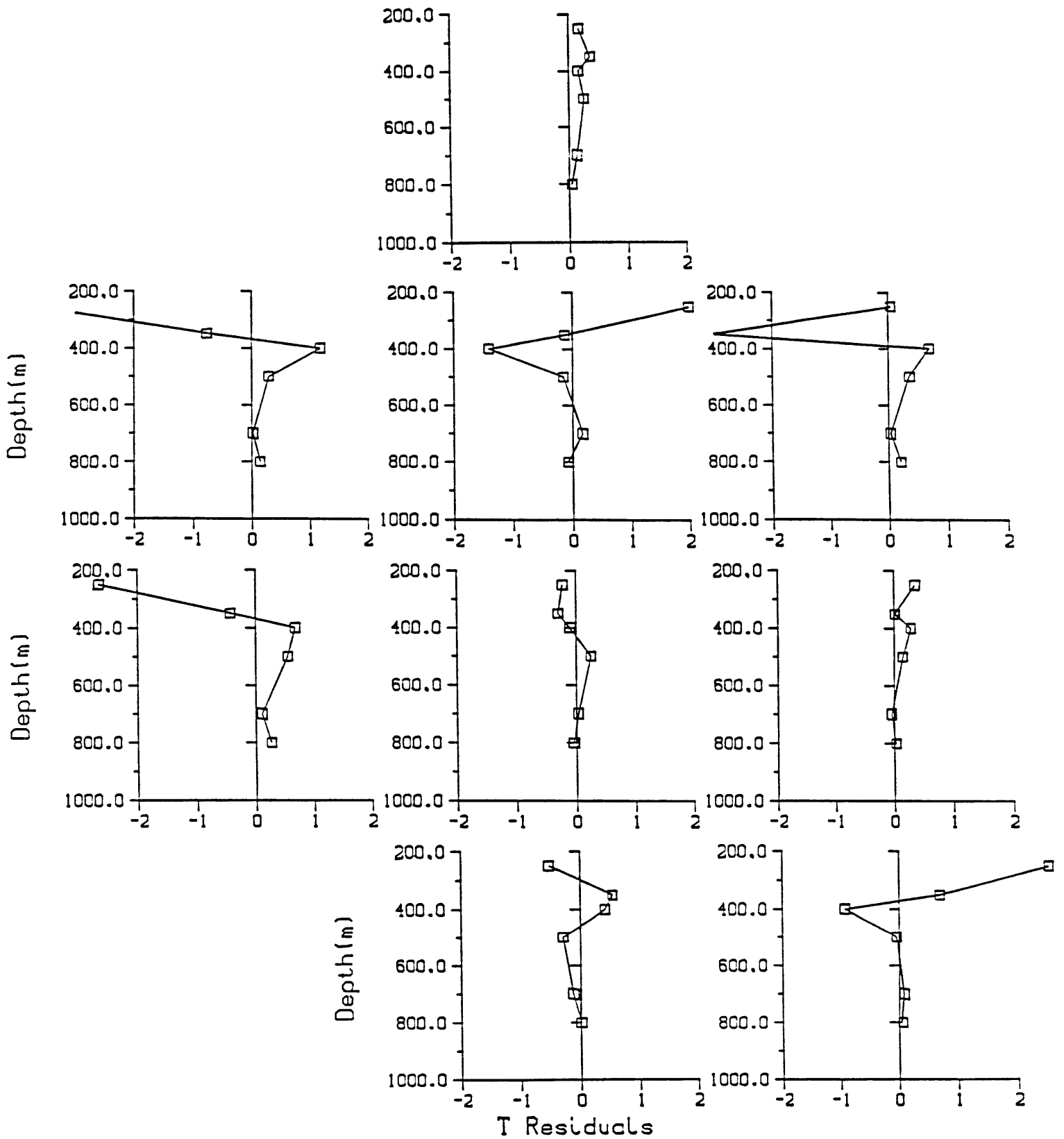


Figure 22. Fall temperature residual profiles for each balance box. Dimensions are change in field (per unit volume over 6 months) in degrees. Final residuals for adiabatic model at rank 31.

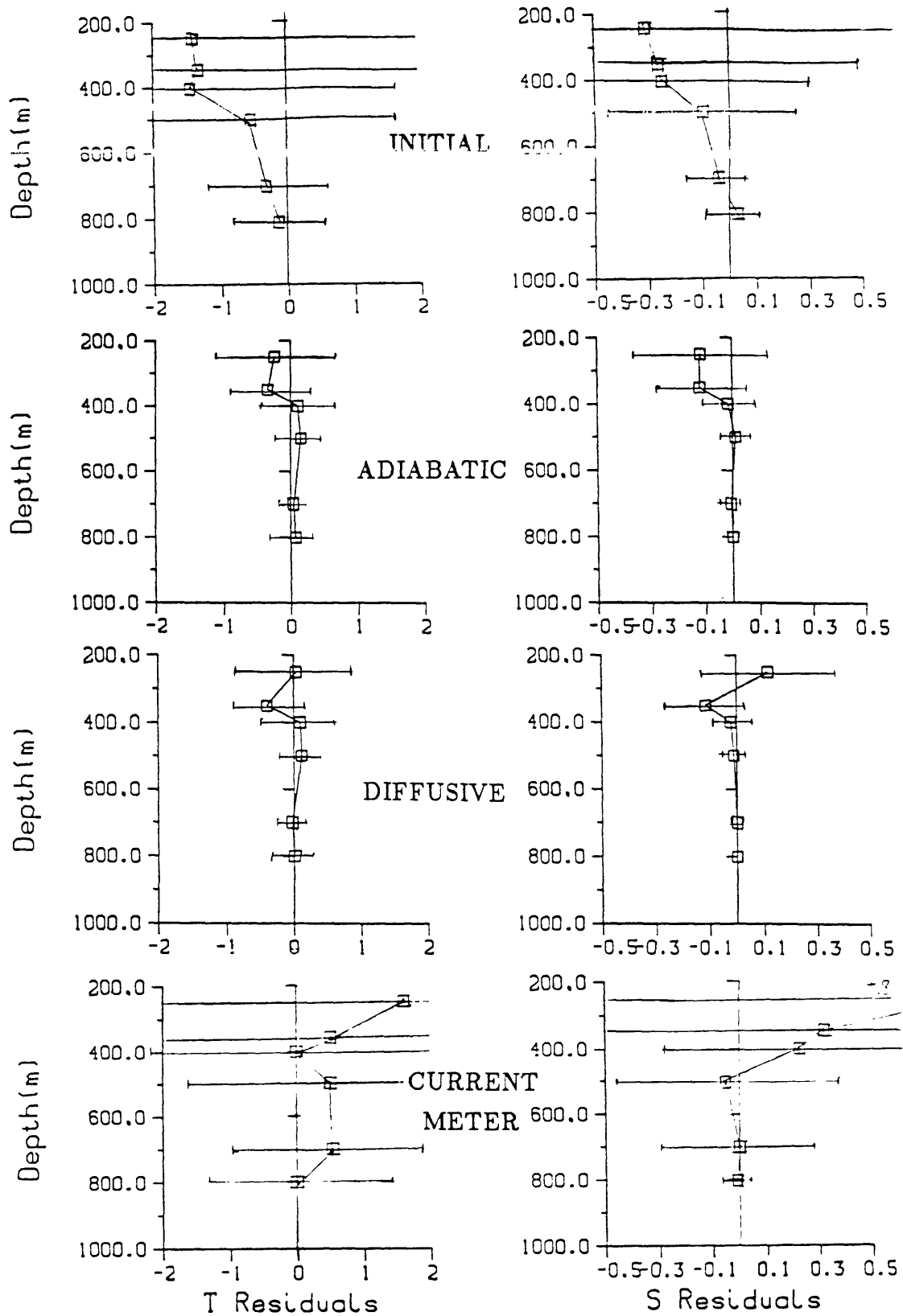


Figure 23. Fall Residuals. Horizontally averaged T (left) and S (right) residuals profiles for the initial model ($\underline{u}_0 = 0$) and for the adiabatic, diffusive and current meter constrained solutions. Error bars indicate standard deviation. Positive T and S is cooling and freshening.

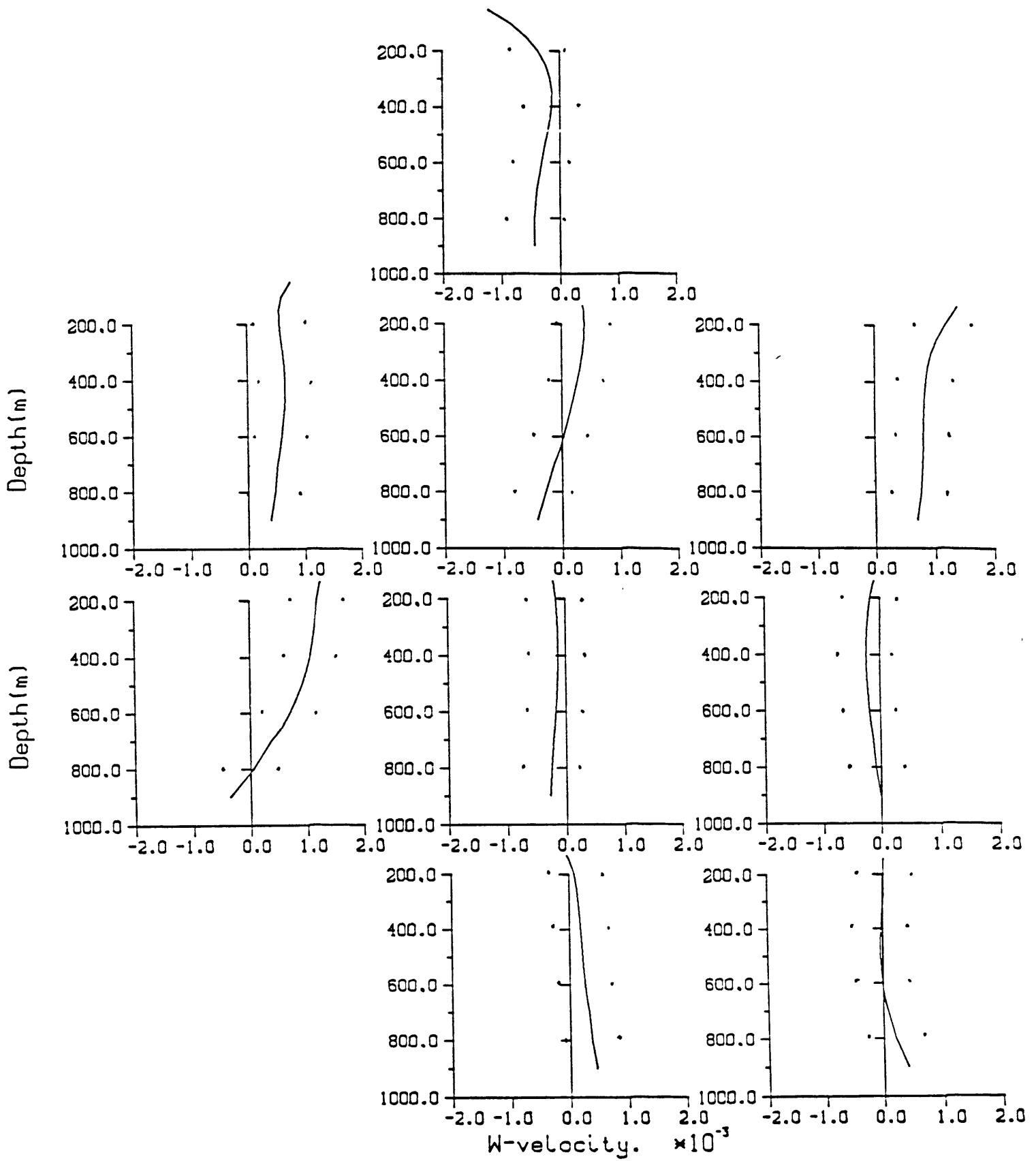


Figure 24. Vertical velocity, $w_{total}(10^{-3}cm/s)$ in each box for adiabatic, fall data inversion. Estimated standard deviation is marked by dots.

profiles for heat and salt are shown in figure 26. The error bars may provide useful upper bounds on the diffusivities.

The distribution of residuals looks random, much the same as figure 22. While the standard deviations are only slightly smaller than the adiabatic case (figure 23), the means are more evenly distributed about zero, and the solution can be considered a slight improvement over the adiabatic case. No substantial reduction of residuals is found, since the residuals were already reduced to the noise level by reference velocities alone. It seems that the CTD data cannot distinguish between vertical transfer by advection or by diffusion and is equally well satisfied by either solution.

We have attempted to find a solution for the fall data consistent with the 30 day (or, almost equivalently, the 13 day) average current meter velocities. As the current meter observations imply much larger velocities than the thermal wind velocities for the fall period, reference level velocities on the order of 10 cm/s are required. As found before, the main difference in the adiabatic and diffusive solutions is in the relative importance of vertical velocity and diffusivity, both of which have large uncertainties. We will show only the results of the diffusive model.

Applying current meter constraints at 3 levels, 350, 400 and 800 db, adds 6 equations, for a system of 123 equations in 46 unknowns. The effective rank was chosen to be 31. Not only the solution (figure 27), but also the magnitude of the resultant residuals is about an order of magnitude larger than without the current meter constraints. The error bars on the diffusivities are much larger (± 10) than without the current meter constraints, even though the effective rank is much smaller. The distribution of residuals still looks random, but the mean values are no longer nearly zero (figure 23), but about .5 degree and .2 ppt, and the standard deviations are very large (compare figure 23 with table 3). Even increasing the effective rank to 45 is not sufficient to reduce the residuals much further. *It appears that this steady state model using the*

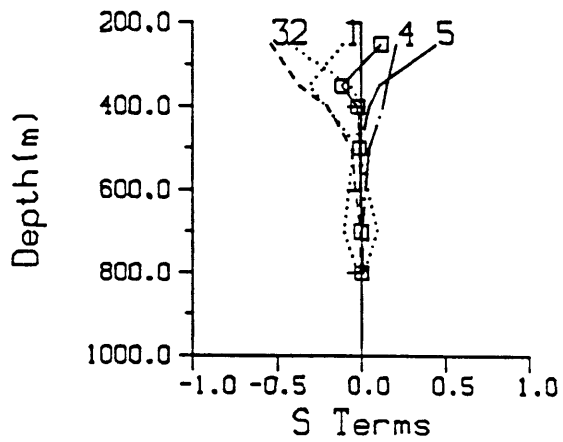
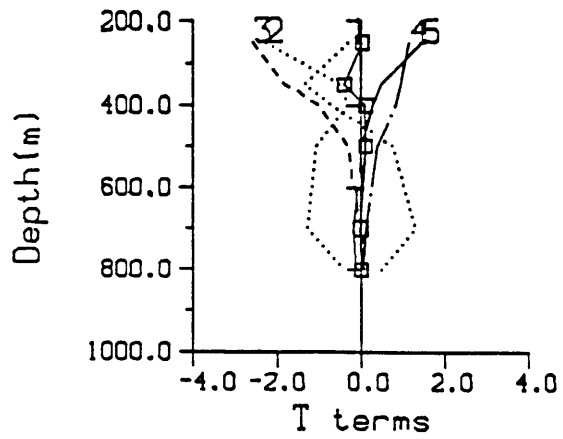


Figure 25. Balance of terms in the fall diffusive model. Positive values correspond to cooling and freshening. 1(dotted)= eastward advection, 2(dotted)= northward advection, 3(dashed)= total horizontal advection, 4(dash-dot)= vertical advection, 5(solid)= diffusion. Residuals are marked by squares.

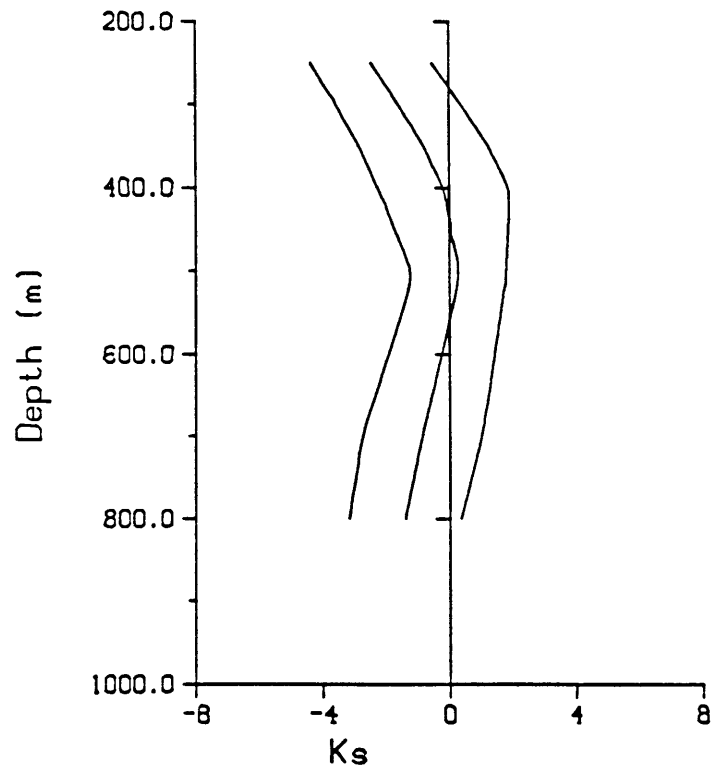
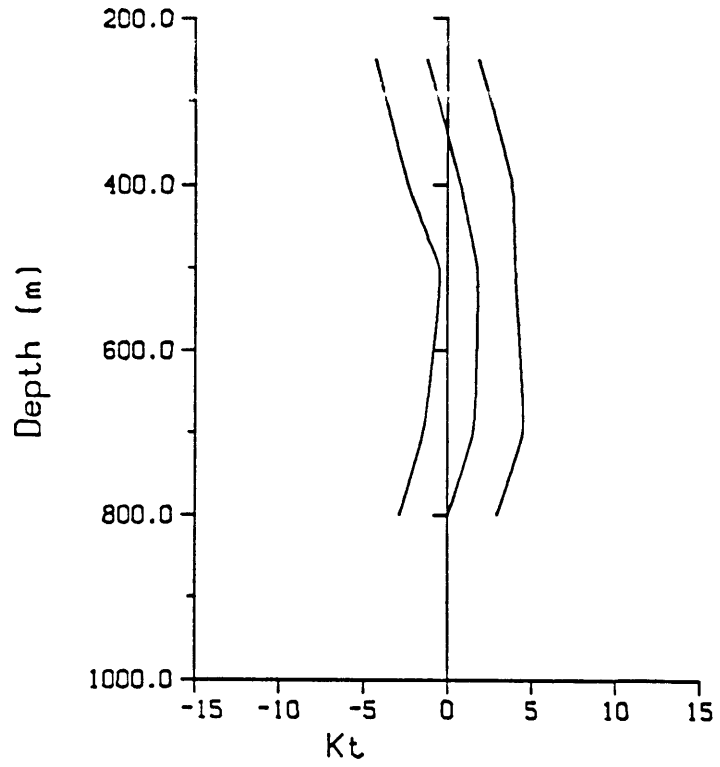


Figure 26. Cross isopycnal heat (upper) and salt (lower) diffusivities and standard deviation (outer lines) for fall data. Units are cm^2/s .

hydrographic data is inconsistent with the strong eddy present in the fall portion of the current meter record.

Spring Solutions

In general, the spring solutions exhibit larger residuals with greater scatter, implying that the spring data is less consistent with a steady state model. This result may be due to the fact that balance boxes contain stronger eddies in the spring than in the fall, which can be seen both in temperature and salinity gradients (figures 8–11) and in relative velocities (figures 12–14). We first seek the best adiabatic solution for the spring data set and find that it does not fit the model as well as the fall data did. We then add diffusivities to see if this improves the residuals. Only slight improvement in the solution was obtained.

The adiabatic system again has 117 equations and 34 unknowns. The effective rank of the adiabatic solution was chosen to be 28. The reference level velocities and velocity field at 400 db are shown in figure 28. As seen in the fall, the reference level velocities are antiparallel to the strongest eddy velocities and act to reduce eddy intensity (compare figure 12). The spatially averaged balance of terms (figure 29) is similar to that for fall, but noisier. The residuals are about twice as large in the spring, yet still fairly randomly distributed. The standard deviations of the spatially averaged residuals, figure 30, are still the same order of magnitude as the estimated error in the equations, although for salinity, the standard deviations about twice as large as the expected error.

To see if the residuals could be reduced further, we again added vertical profiles of heat and salt diffusivities, for a system of 117 equations and 46 unknowns. The rank was chosen to be 37.

The balance of terms (figure 31) is such that diffusivity is larger than vertical advection for both T and S equations above 550 m. However, this is probably not a significant result, because both w and the diffusivities (figure 32) have larger standard

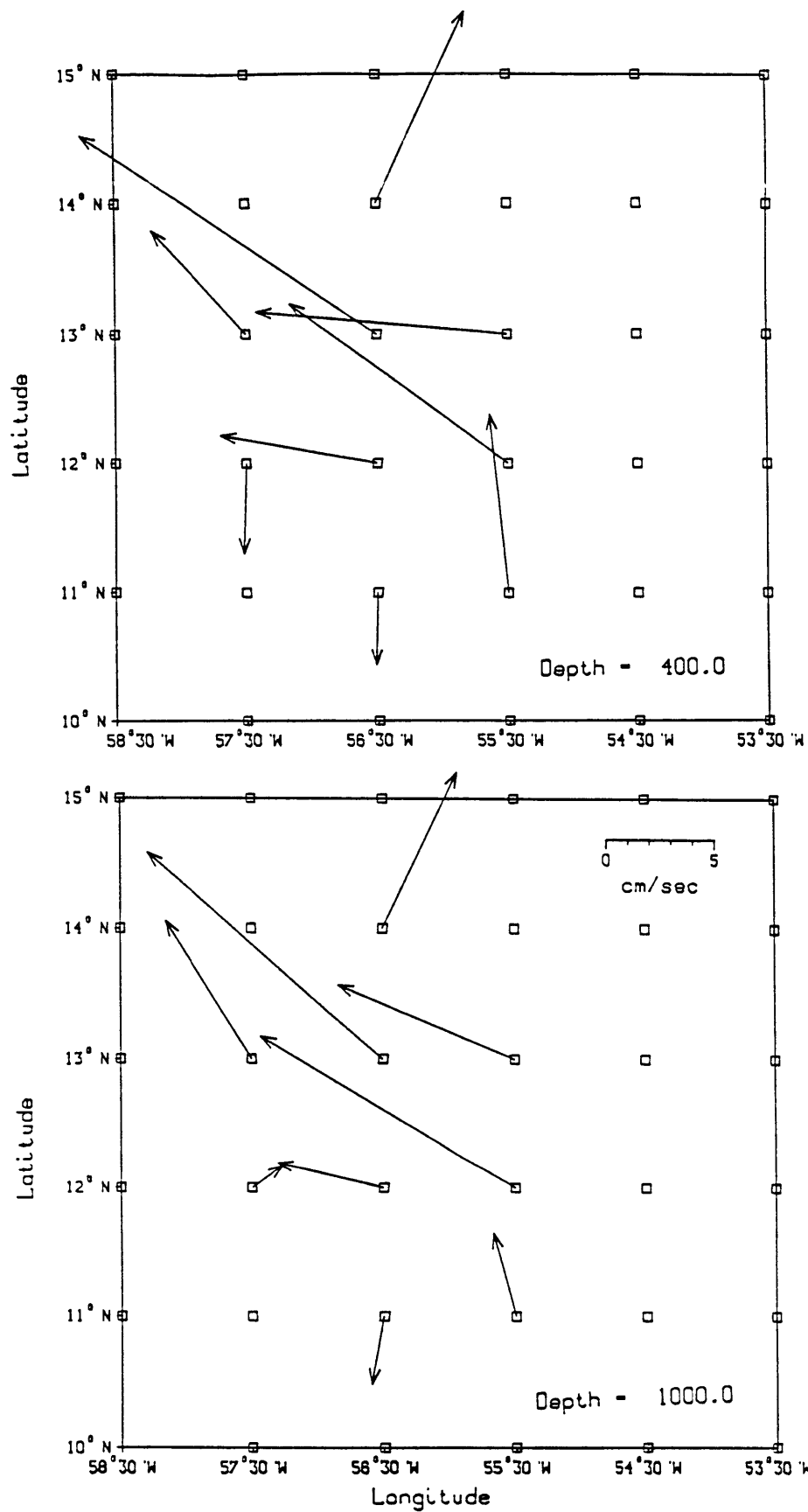


Figure 27. Reference level velocities for current meter constrained fall, diffusive solution. Standard deviation is about 2.0–5.0 cm/s.

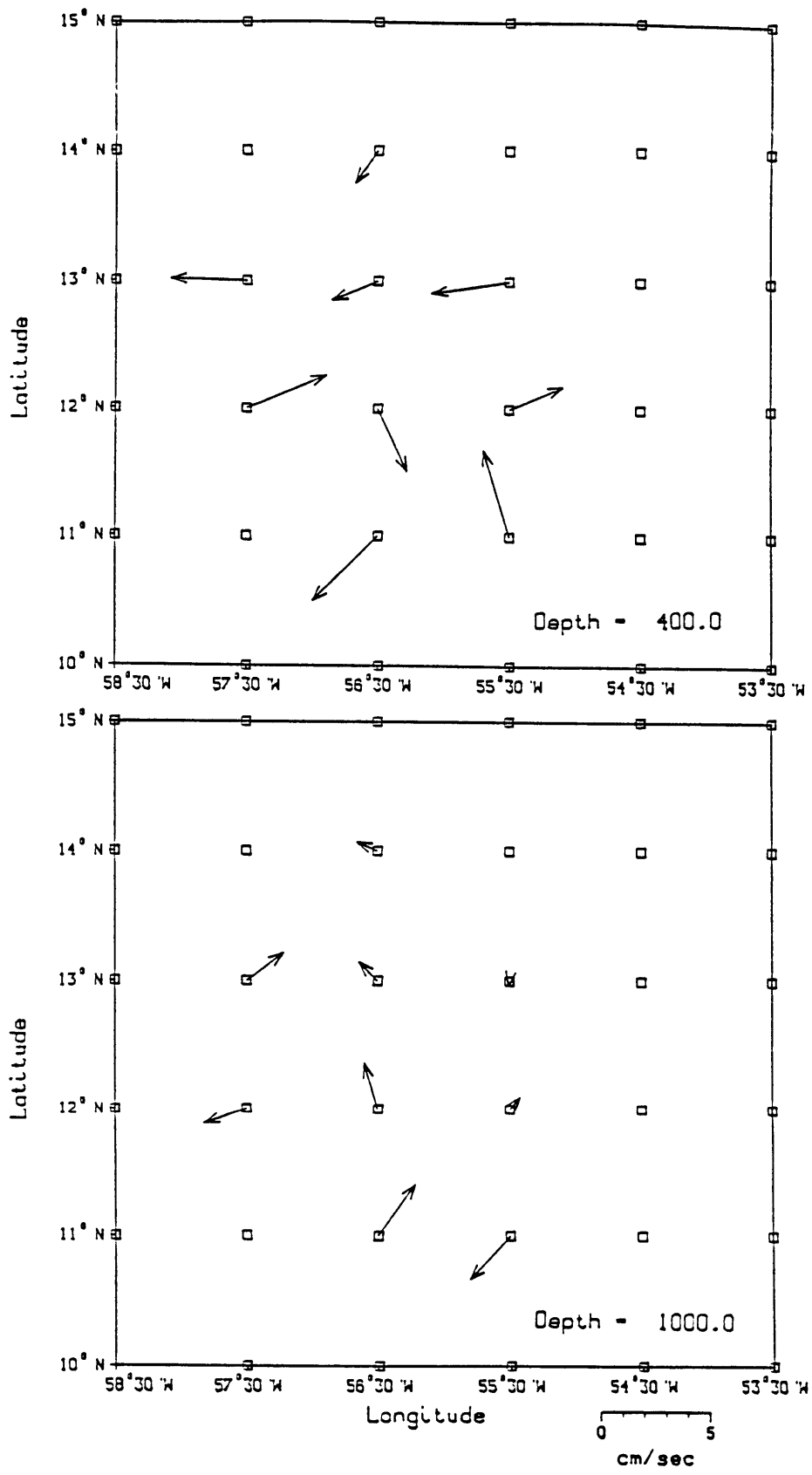


Figure 28. Spring adiabatic solution for reference level velocities and velocities at 400 db. Standard deviation is about 0.2–0.6 cm/s.

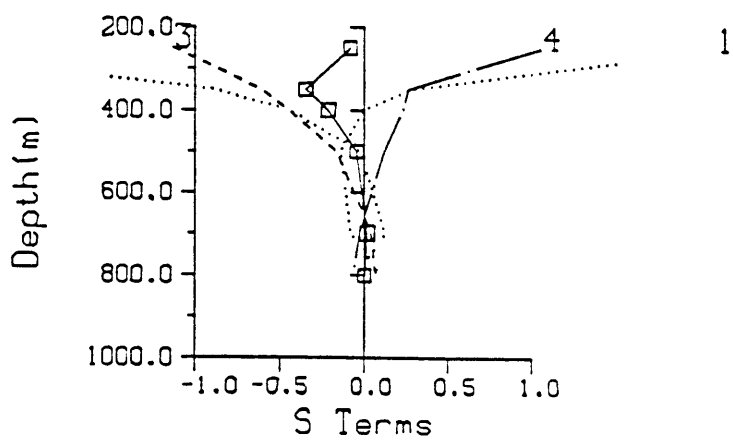
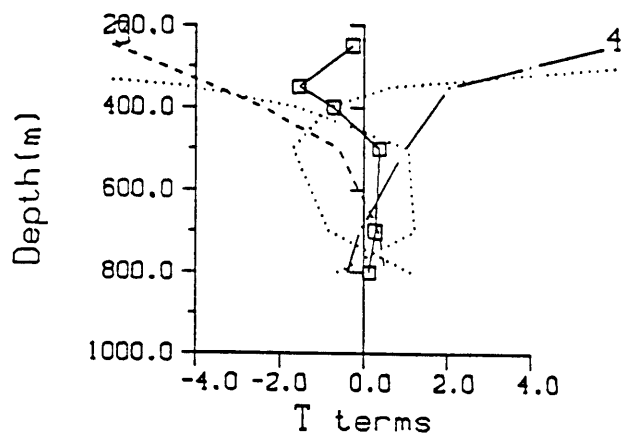


Figure 29. Average balance of terms in each box for spring adiabatic model. Labels are the same as in figure 21.

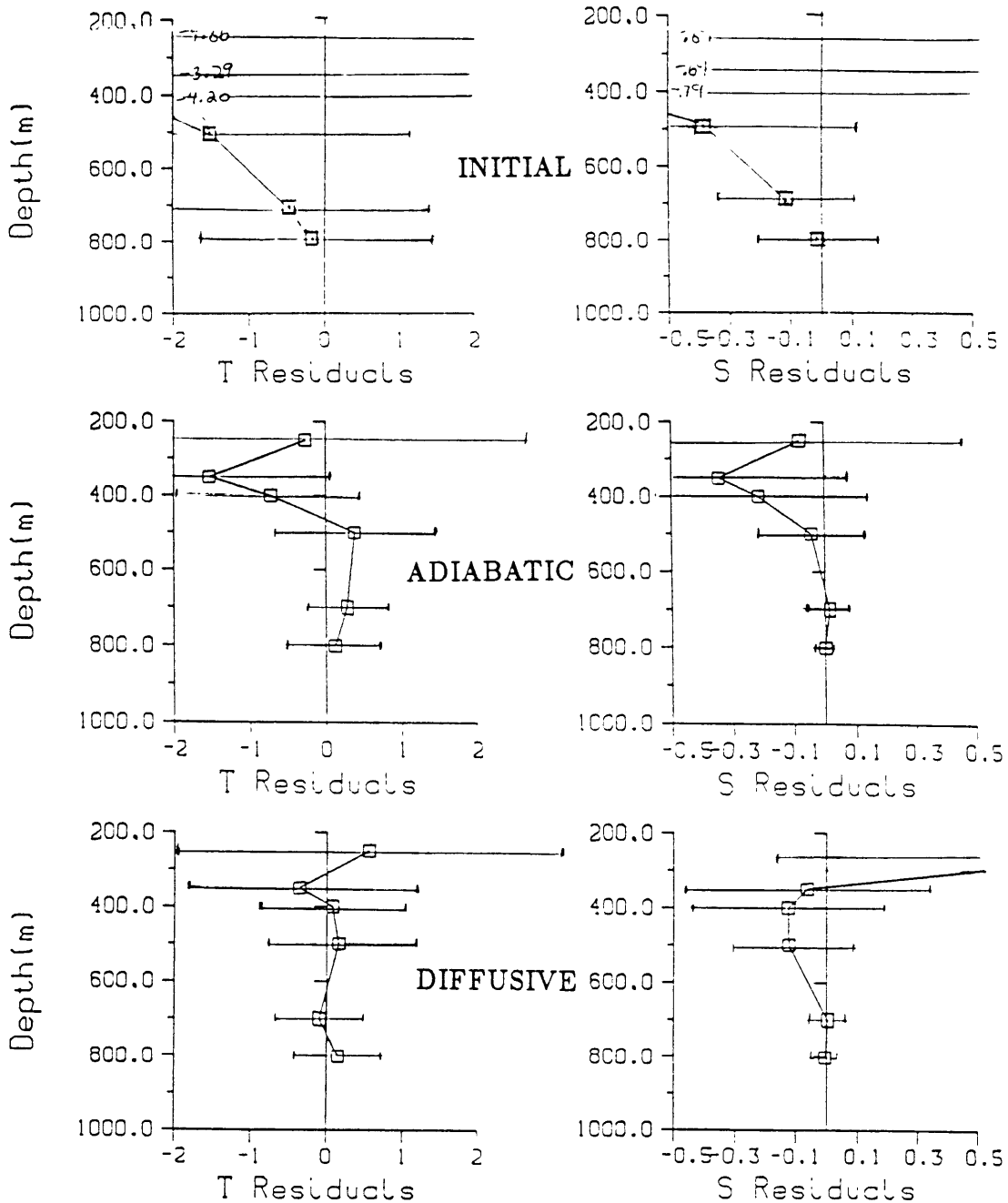


Figure 30. Spring Residuals. Horizontally averaged T and S residuals at each depth for the starting model ($u_0 = 0$) and for the adiabatic, and diffusive solutions. Error bars indicate standard deviation.

deviations than those found in the fall. The averaged temperature and salinity residuals at each level have somewhat reduced mean values over the adiabatic model, but still have only marginally acceptable standard deviations (figure 30).

Summary of Cartesian Inversions

In both spring and fall, the balance of terms was horizontal advection balanced by the sum of vertical advection and cross-isopycnal diffusivity, neither of which were well constrained by the inversions. The horizontally averaged horizontal advection term acted to increase the temperature and salinity at each level. Together the diffusion and vertical advection terms acted to cool and freshen the water.

The fact that the addition of further complexity in the model, that is diffusivity, does not have much effect on the residuals suggests that the residuals are more controlled by the missing time derivative term than by diffusivity. Diffusivity provided a slight reduction in residuals. The primary parameters in reducing the residuals were the horizontal reference velocities. This could be seen by examining the diagonal elements of the VV^T matrix at various stages in the summation of equation (3.21). The inversion first used the horizontal velocities to reduce the residuals, then W and κ were engaged later in the summation to try to further reduce the remaining residuals.

The fall data are apparently consistent with an adiabatic steady state model, as long as we do not impose the current meter constraints. The inversion using just the tracers acts to reduce eddy velocities and to bring the solution closer to a steady state model, while the current meter constraints push the solution the opposite way. The large barotropic component of flow (about 10 cm/s) indicated by the current meter data is insufficiently constrained by just one mooring. If additional moorings had been used to delineate the structure of the flow at 1000 m, this information might have been a useful constraint in the inversion, and may even have allowed a time dependent model.

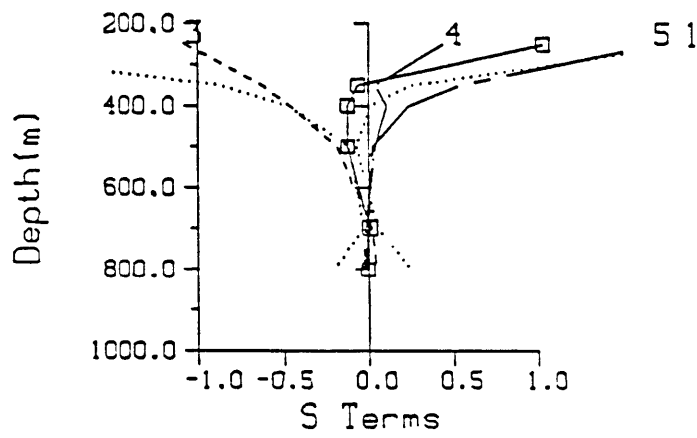
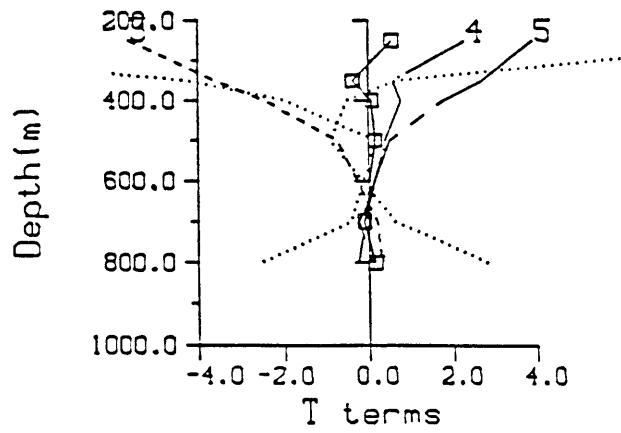


Figure 31. Average balance of terms in each box for spring diffusive model. Labels are the same as in figure 25.

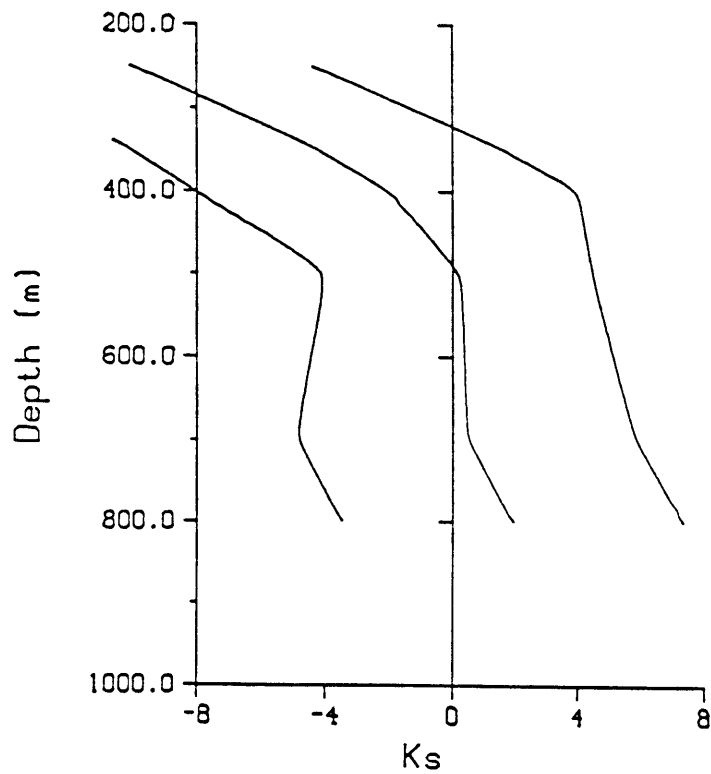
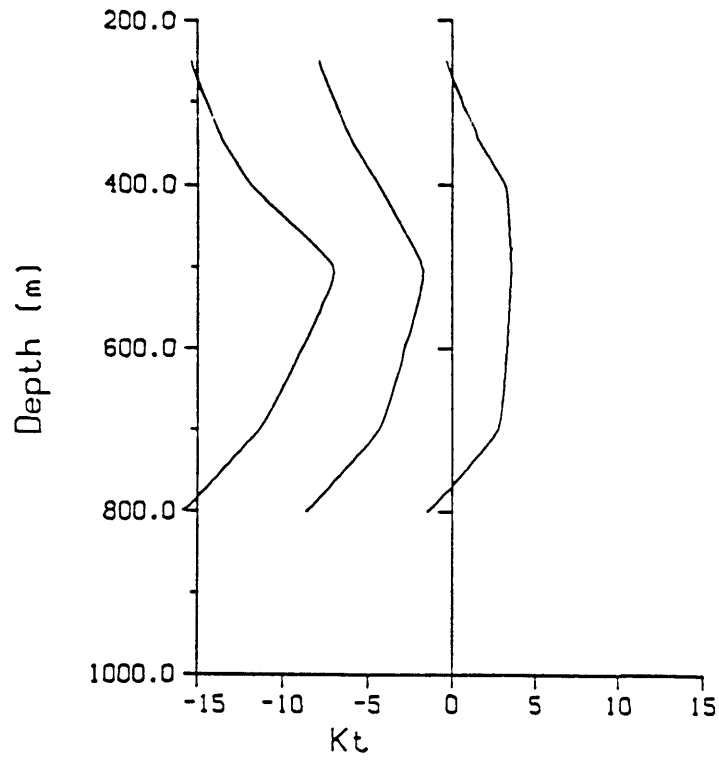


Figure 32. Cross isopycnal heat (upper) and salt (lower) diffusivities and standard deviation (outer lines) for spring data. Units are cm^2/s .

The spring data are less consistent with a steady state model, probably due to the stronger eddy velocities and stronger tracer gradients in the region where balances were evaluated. In the tracer maps at 800 db, eddies can be seen in the spring data but not in the fall. The diffusivities were less well constrained in the inversion of spring data, perhaps because the balance boxes included fewer staircases than they did in the fall. The top of the staircase corresponds roughly with sigma theta 26.8, which lay at about 240 db depth in the fall and 270 db in the spring. The uppermost tracer balance level, centered at 250 db, would have contained staircase structure only in the fall. The horizontal distribution also favored the fall data set. In the spring, well developed steps were seen in only the eastern half of the region where balances were sought, so that west of about 56°W, only irregular steppiness was seen in the CTD profiles. In contrast, in the fall profiles, well developed steps were present over the entire area where balances were evaluated.

In order to better define an average advection and diffusion for the region, attempts were made to smooth out the eddies using objective mapping (with a 500 km correlation length scale) to obtain long term average tracer and velocity fields. Unfortunately, inversions using this smoothed data set did not yield any useful estimates regarding the importance of diffusion because the smoothed data were easily fit by a purely adiabatic model and lacked any resolution of the diffusivities. Tziperman (1987) discusses why inversions using time averaged data sets may not be expected to provide meaningful estimates of higher order terms such as vertical velocity and diffusivity. He argues that these parameters κ and w are unreliable because they are determined from the residuals left after the primary parameters, u and v have been determined. Small adjustments in the horizontal velocities cause large changes in the structure of the remaining residuals. Without smoothing however, it is difficult to define an average advection through the region.

Chapter 4. Isopycnal Inversions

4.1 Model Dynamics

As in the previous formulation, we seek the simplest steady state, geostrophic model which is consistent with the observations. The advection–diffusion equation will be a slightly modified version of equation (3.5). In the cartesian formulation the cross-isopycnal transfer had 2 components: the component of w normal to isopycnals, and the turbulent mixing, $\kappa(z)$. With that parameterization, we found that we did not obtain satisfactory resolution of either w or κ . We now reformulate the problem to simplify the treatment of cross-isopycnal transfer. Rather than dividing w into relative and reference components as before, we will solve directly for cross isopycnal velocity, w^* at each level. Double diffusive mixing will be represented by unknown cross-isopycnal fluxes, F , which are non-zero only between sigma theta levels 26.8–27.2, where thermohaline steps are found. Double diffusive heat and salt fluxes will be related by

$$F_T = \gamma \frac{\beta}{\alpha} F_S.$$

as suggested by Schmitt (1981). γ is taken to have an average value of .7 in the step region, so that with $\beta = 7.5 \cdot 10^{-4}$ and $\alpha = 2.0 \cdot 10^{-4}$, the flux ratio used is $F_S = 0.38 F_T$. Double diffusive fluxes can be allowed to vary horizontally, if necessary. This model can also include turbulent diffusion along and across isopycnals, as in the previous formulation, if the inversions indicate that this term is necessary. The turbulent diffusion, κ , would be the same for heat and salt.

Using the continuity equation, the temperature (and similarly for salt) advection–diffusion equation now looks like

$$\nabla \cdot (\underline{u}T) - \nabla \cdot (\kappa \cdot \nabla T) + \nabla \cdot F_T = 0. \quad (4.1)$$

We divide u and v into relative and reference parts ($w_{rel} = 0$), and compute the relative parts from the dynamic heights on isopycnals according to equations (2.7). Moving the terms containing the unknowns, $u_0(x, y)$, $v_0(x, y)$, $w^*(x, y, z)$, $F_T(z)$, (and $\kappa(z)$), to the left hand side, and terms containing the relative velocities to the right hand side, then integrating over each box, we get an equation analagous to (3.13):

$$\oint_{boundary} (\underline{u}_0 T) \cdot ds - \oint_{boundary} (\kappa \cdot \nabla T) \cdot ds + \oint_{boundary} F_T \cdot ds = - \oint_{boundary} (\underline{u}_{rel} T) \cdot ds. \quad (4.2)$$

Since we are allowing w^* to be set by the inversion rather than computing it from the continuity equation as before, the total velocity field is not automatically nondivergent. We must impose the continuity equation as a separate constraint,

$$\oint_{boundary} \underline{u} \cdot ds = 0. \quad (4.3)$$

We have tried to make a model with the advective transfer across isopycnals specified by the cross isopycnal components of the horizontal velocity. These components are given by $\underline{u}_c \equiv \underline{u} \cdot \nabla h$, where ∇h is the normal to an isopycnal surface. Although the velocities were horizontally nondivergent and in finite difference form would have conserved mass exactly in rectangular boxes, boxes bounded by isopycnals do not conserve mass. The mass imbalances led to large and irreducible tracer imbalances and we could not find a satisfactory solution with acceptable residuals. In order to conserve mass and obtain a satisfactory solution we must allow the model to determine the necessary cross isopycnal mass fluxes, w^* . The equations used in the inversion, (4.2) and (4.3) are expressed in finite difference form in the next section.

4.2 Finite Difference Formulation

As in the cartesian model, we use a staggered grid in the horizontal plane as shown in figures 17.a and 17.b. Only the vertical grid is different. A profile of the new grid is shown in figure 33. The sigma theta range from 26.0 to 27.4 has been divided into 4 boxes in which tracer balances are evaluated. The mean depths of the uppermost and lowermost isopycnals are 158 db and 947 db in spring (137 and 914 db in fall), so that this model represents a much coarser grid in the vertical than did the cartesian grid. The levels were chosen to isolate the staircase structure in the 2 center boxes and to have one box above and one below the staircases. Double diffusive fluxes are sought at levels 26.8, 27.0 and 27.2, which define the upper extent, the middle and lower extent of the staircases. Cross isopycnal velocity W^* is solved for at the 5 interfacial levels of the 4 boxes.

Equation (4.2) is written in finite difference form, excluding the turbulent diffusion, as

$$\begin{aligned}
 & [(U_0 T \Delta Z)_E - (U_0 T \Delta Z)_W] \Delta Y + [(V_0 T \Delta X \Delta Z)_N - (V_0 T \Delta X \Delta Z)_S] \\
 & \quad + [(W^* T)_U - (W^* T)_L] \Delta X_M \Delta Y + [(F_T)_U - (F_T)_L] \Delta X_M \Delta Y \\
 & = [(U_{rel} T \Delta Z)_E - (U_{rel} T \Delta Z)_W] \Delta Y + [(V_{rel} T \Delta X \Delta Z)_N - (V_{rel} T \Delta X \Delta Z)_S].
 \end{aligned} \tag{4.4}$$

Capital subscripts, N,S,E,W,U and L indicate the side on which the quantity is evaluated. ΔZ is computed from the pressure on isopycnals and is different on each side of the box. The mass balance equation (4.3) would be written the same way, except T is replaced by 1 and the double diffusive flux term does not appear. This isopycnal formulation greatly simplifies the form of the advection-diffusion equation.

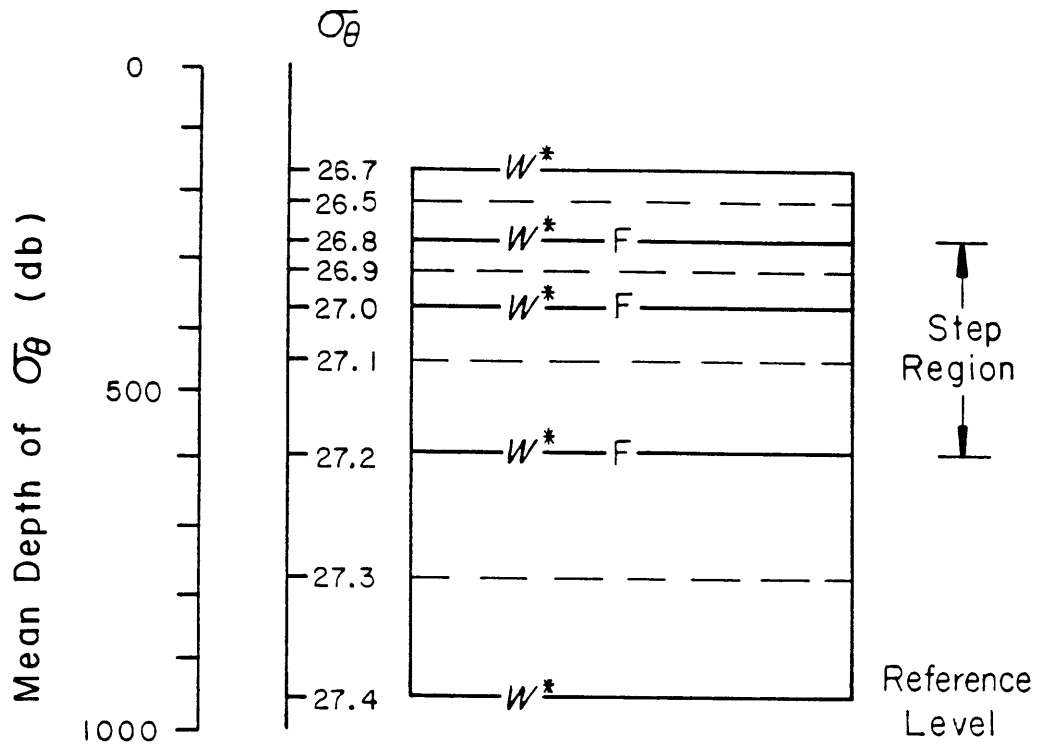


Figure 33. Vertical profile of the grid. Average depth of the isopycnals (for spring) is indicated by the depth axis. Double diffusive fluxes are allowed at the interfaces marked with F, and the W^* are found at each of the 5 interfaces. (The flat interfaces here are only schematic; the actual geometry follows the isopycnals.)

4.3 Results of Isopycnal Inversions

With equations evaluated for temperature, salinity and mass conservation at 4 levels and 9 horizontal boxes, we have a system of 108 equations. At each horizontal location we solve for U_0 , V_0 and 5 W^* 's . In addition there are 7 peripheral horizontal reference velocities and 3 values of double diffusive flux for the grid, for a total of 73 unknowns. We will discuss here the solutions using the fall and spring data sets for comparison with the results of the inversion in cartesian coordinates. The model does not include turbulent diffusivities, as we found that the model has enough free parameters with $W^*(z)$ and that additional parameters were not required by the data. Although the model could in principle include current meter constraints, in light of the results of the cartesian inversions, those constraints will be omitted here.

The mass balance equation was given 10 times the weight of the tracer equations to insure that the temperature and salinity residuals were not artificially increased by mass imbalances. This weighting scheme improved the residuals for all of the equations. The columns multiplying W^* and F were weighted by 10^{-3} so that coefficients were all the same order of magnitude. All other variables were weighted by 1. We also found that subtracting the mean temperature and salinity values at each box and balancing the tracer anomalies, T' and S' , improved the final residuals. This is because in the flux form of the equations, $\underline{u} \cdot \nabla T$ is replaced by $\nabla \cdot (\underline{u}T)$, which contains $T(\nabla \cdot \underline{u})$. Any inadvertent mass imbalances are therefore multiplied by T or S, so use of T' and S' minimizes the effect of 'leaky' boxes. Mass imbalance was not a problem in the cartesian formulation where the continuity equation was satisfied identically.

Fall Solution

The rank was chosen to be 61. Initial and final residuals are shown in Table 4. Reference level velocities and velocities at sigma theta 27.0 are shown in figure 34. The reference level velocity is slightly more eastward than the cartesian solution, but the velocity in the steps ($\sigma_\theta=27.0$) looks very similar to that at 400 db (compare with figure

20). About the only difference is that where the isopycnal surface is much shallower than 400 m, as in the southwest corner, the velocities are larger.

The cross-isopycnal velocity is shown in figure 35. In this formulation, the diagonal elements of VV^T as the summation (3.21) progresses indicate that W^* is resolved together with the horizontal reference velocities, rather than after the horizontal velocities have already been determined. Error bars are smaller than those on vertical velocities in the cartesian formulation. W^* is not consistent in sign, even in the step region, and horizontally averaging gives values less than $1 \times 10^{-4} \text{ cm/s}$ at each depth. We have also computed the cross-isopycnal component of the horizontal velocities, $\underline{u} \cdot \nabla h$, to compare its magnitude with W^* . As seen in figure 35, there does not seem to be much correlation.

The values of double diffusive buoyancy heat fluxes for the bottom, middle and top of the step region are as follows:

$$\begin{aligned} \text{top:} \quad & \alpha F_T = (5.4 \pm 4.2) \times 10^{-8} \text{ cm/s} \\ \text{middle:} \quad & \alpha F_T = (-0.2 \pm 2.0) \times 10^{-8} \text{ cm/s} \\ \text{bottom:} \quad & \alpha F_T = (-6.4 \pm 5.4) \times 10^{-8} \text{ cm/s} \end{aligned}$$

Correspondingly, buoyancy salt fluxes $\beta F_S = 7.7 \times 10^{-8} \text{ cm/s}$ on the top, and $\beta F_S = -9.1 \times 10^{-8} \text{ cm/s}$ on the bottom. These were resolved independently of W^* , and the divergence is better resolved than the individual fluxes. The value of $\frac{\partial}{\partial z} \beta F_s$ is $(.54 \pm .3) \times 10^{-11} \text{ s}^{-1}$.

The balance of terms in individual boxes is generally horizontal advection balancing cross-isopycnal advection. The horizontal averages of both of these advection terms, shown in figure 36, is much smaller than the unaveraged terms. The slope of the flux term can be ignored since the middle value has such large variance, only the average flux over the layers is determined. The positive value of the double diffusion term signifies that the time derivative of T and S is negative, that is cooling and freshening,

Fall

Sigma Theta	T Residuals	S Residuals
26.5	.15 (4.44)	.05 (1.39)
26.9	-.76 (3.54)	-.19 (.89)
27.1	-.53 (2.93)	-.11 (.61)
27.3	-.05 (.84)	-.01 (.13)
26.5	.04 (1.55)	.05 (.47)
26.9	-.34 (2.18)	.02 (.49)
27.1	-.11 (.73)	.02 (.14)
27.3	.09 (.56)	.01 (.10)

Spring

26.5	-.03 (4.68)	-.00 (1.46)
26.9	-.87 (3.37)	-.21 (.85)
27.1	-3.23 (9.32)	-.66 (1.90)
27.3	-.10 (1.25)	-.01 (.20)
26.5	.15 (2.06)	.03 (.33)
26.9	-.23 (.53)	.05 (.22)
27.1	-.25 (1.21)	-.01 (.38)
27.3	.02 (.46)	.02 (.09)

Table 4: Initial and final residuals for fall and spring inversions. Standard deviations given in parentheses.

which is the expected role of double-diffusion in turning NACW into the mixture of NACW and SACW observed in the C-SALT region.

Spring Solution

The rank of the solution was chosen to be 65. Velocities at sigma theta 27.4 and 27.0 are shown in figure 37. Again, the velocities look quite similar to the cartesian solution (figure 28). The balance of terms averaged over all the boxes is shown in figure 38. The residuals (table 4) are about the same magnitude as the fall isopycnal solution, and are somewhat smaller than the spring solution in the cartesian inversion. Cross-isopycnal velocity again looks rather randomly distributed in space and has error bars

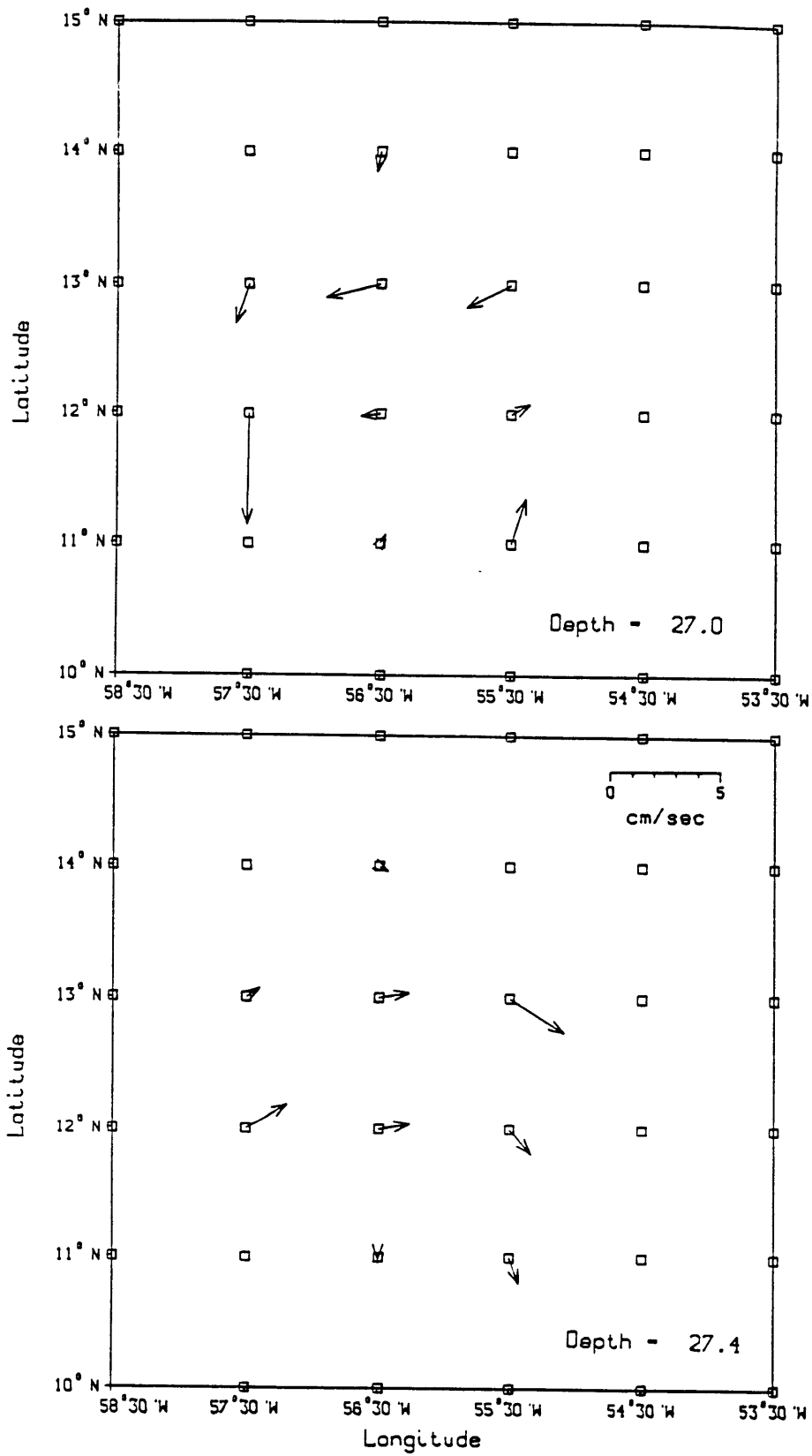


Figure 34. Reference level velocities (27.4) and velocities at sigma theta 27.0 for the fall isopycnal inversion. Standard deviation of the reference velocities is about 0.6–0.9 cm/s.

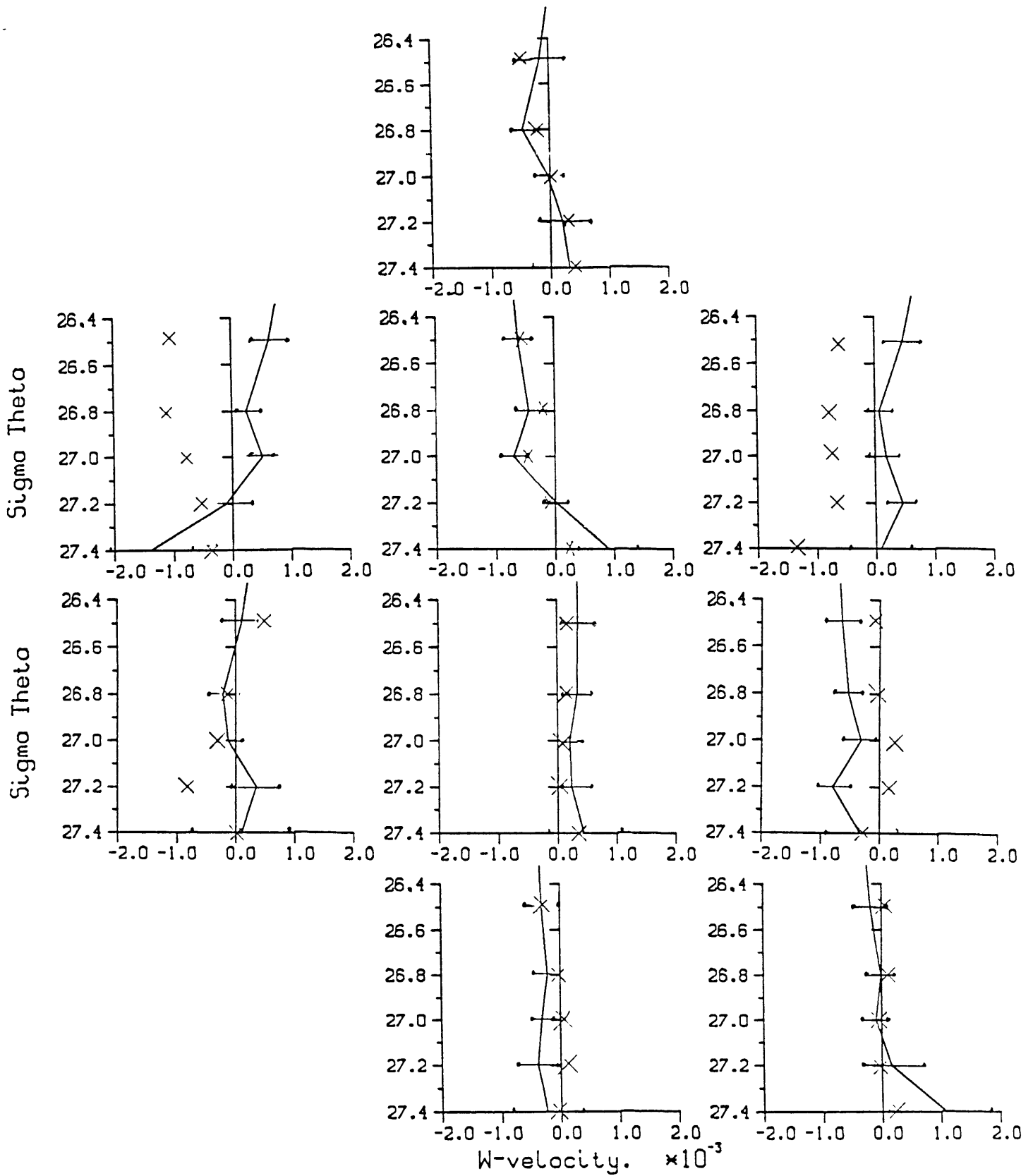


Figure 35. Fall cross-isopycnal velocity profiles in each of the 9 balance boxes. Standard deviation indicated by error bars. Cross isopycnal component of the horizontal velocity ($\underline{u} \cdot \nabla h$) marked by X's.

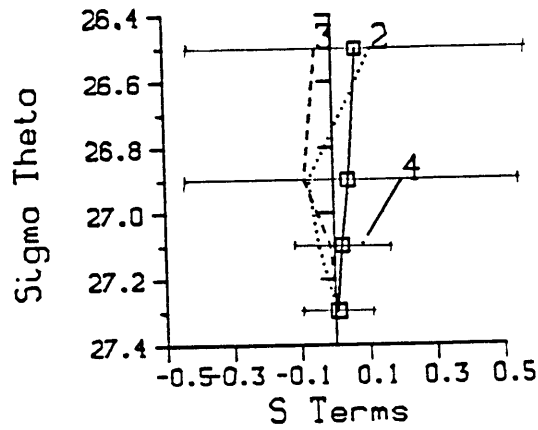
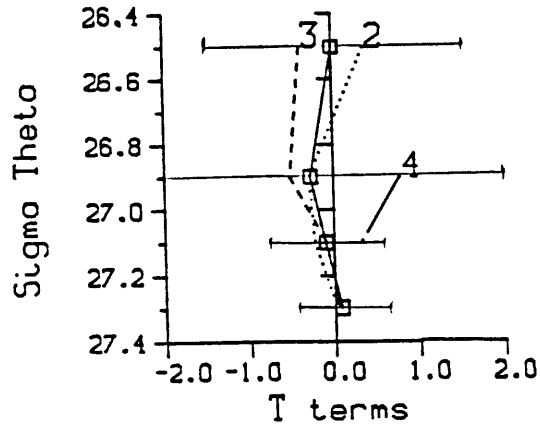


Figure 36. Fall balance of horizontally averaged terms. Positive terms correspond to cooling and freshening. 2(dotted line)= horizontal advection; 3(dashed line)= cross isopycnal advection; 4(solid line)= double diffusion; Residuals indicated by squares. Note scale is twice as large as used in cartesian figures. Standard deviation of the residuals is indicated by error bars.

smaller than the values of W^* . The values obtained for the buoyancy heat fluxes are very close to those obtained in the fall inversion:

$$\begin{aligned} \text{top:} \quad & \alpha F_T = (3.6 \pm 3.4) \times 10^{-8} \text{ cm/s} \\ \text{middle:} \quad & \alpha F_T = (0.8 \pm 1.8) \times 10^{-8} \text{ cm/s} \\ \text{bottom:} \quad & \alpha F_T = (-6.0 \pm 4.8) \times 10^{-8} \text{ cm/s} \end{aligned}$$

Correspondingly, $\beta F_S = 5.1 \times 10^{-8} \text{ cm/s}$ on the top, and $\beta F_S = -8.6 \times 10^{-8} \text{ cm/s}$ on the bottom. As in the fall, the flux divergence is better determined than the individual fluxes and $\frac{\partial}{\partial z} \beta F_s$ has a value of $(.42 \pm .2) \times 10^{-11} \text{ s}^{-1}$.

Summary of Isopycnal Inversions

Spring and fall solutions gave similar results, unlike the situation found in cartesian coordinates where the spring solution had larger residuals. Both isopycnal solutions had horizontal advection acting to increase temperature and salinity in the step region, and double diffusion acting to cool and freshen the water. Cross-isopycnal advection was not consistent in sign, acting in the same sense as horizontal advection in the fall, and in both senses in the spring. W^* had an average magnitude of about $5 \times 10^{-4} \text{ cm/s}$, and had smaller error bars than the cartesian vertical velocity.

Spring and fall inversions gave similar estimates of the buoyancy salt flux divergence, $\frac{\partial}{\partial z} \beta F_s = (.42 \pm .2) \times 10^{-11} \text{ s}^{-1}$ in spring and $(.54 \pm .3) \times 10^{-11} \text{ s}^{-1}$ in fall. This average value for the C-SALT staircase is roughly half the size of the Lambert and Sturges's (1977) value, $\frac{\partial}{\partial z} \beta F_s = 1.33 \times 10^{-11} \text{ s}^{-1}$ for the Caribbean region. We can obtain a rough estimate of the corresponding salt diffusion coefficients from $\frac{\partial}{\partial z} \beta F_s \approx \kappa \frac{\partial^2 S}{\partial z^2}$ using the buoyancy salt flux divergence and average salinity gradients between sigma theta 26.9 and 27.1. We get $\kappa_s = (2.8 \pm 1.3) \text{ cm}^2/\text{s}$ in spring and $\kappa_s = (3.9 \pm 2.2) \text{ cm}^2/\text{s}$ for the fall data, compared to Lambert and Sturges's estimated $5.7 \text{ cm}^2/\text{s}$. These results support the finding of Schmitt et al. (1987) whose analysis of the C-SALT staircase indicates that Lambert and Sturges's (1977) estimates of double diffusive fluxes (based on the 4/3 power law) may be overestimated.

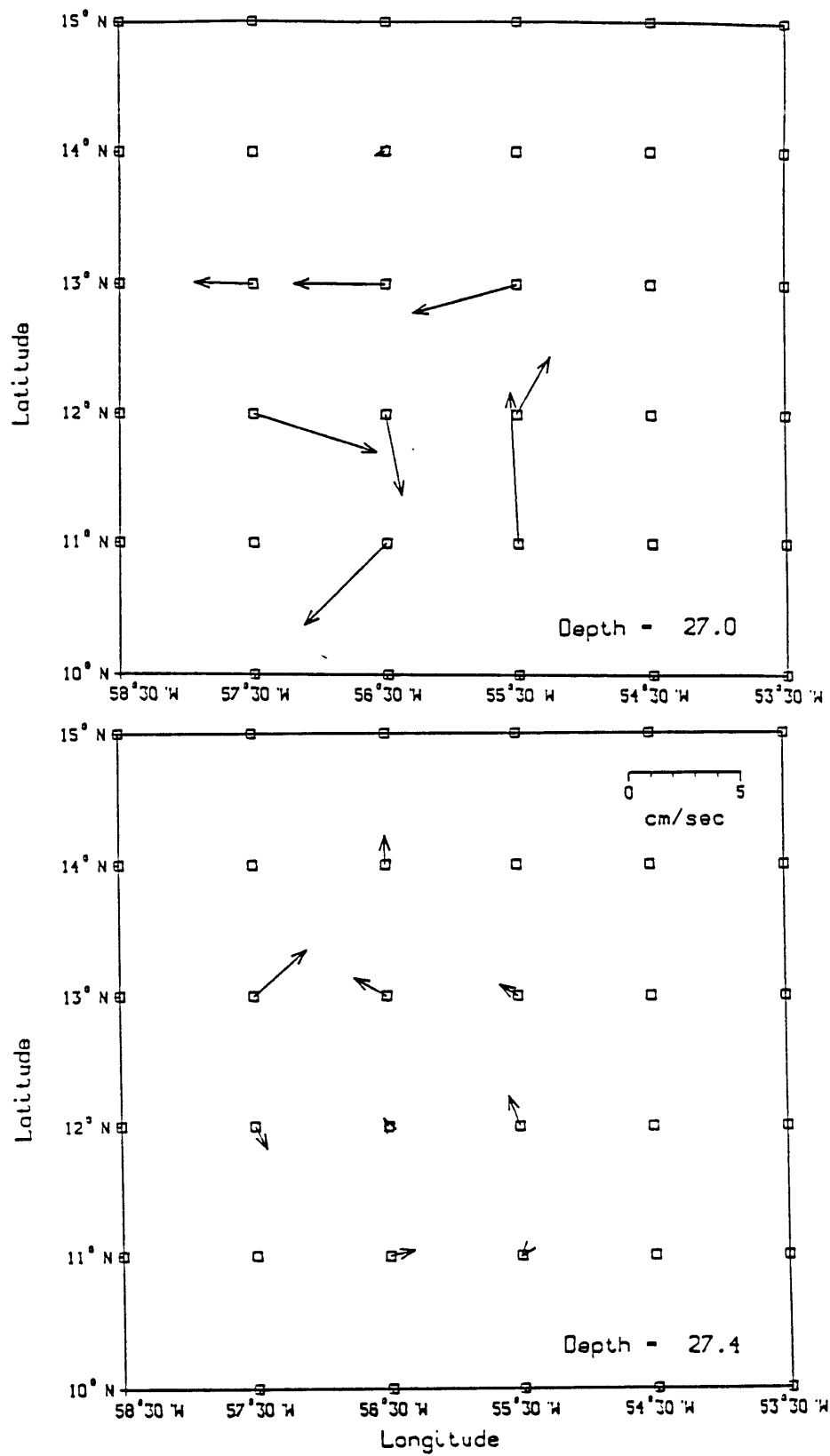


Figure 37. Reference level velocities (27.4) and velocities at sigma theta 27.0 for the spring isopycnal inversion. Standard deviation is about 0.5–0.7 cm/s.

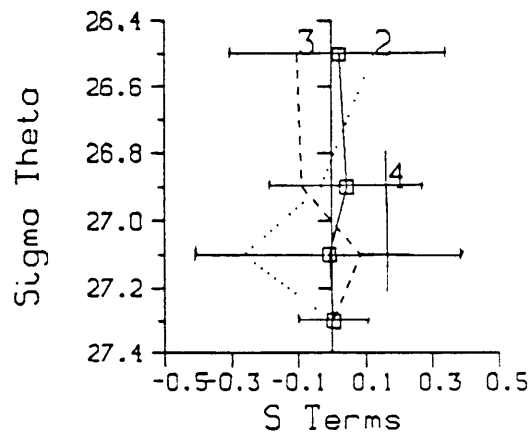
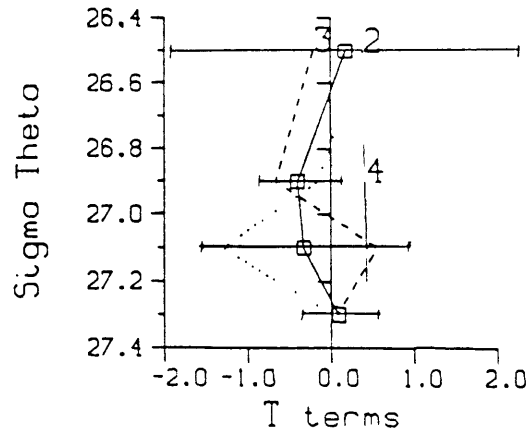


Figure 38. Spring balance of horizontally averaged terms. Positive terms correspond to cooling and freshening. 2(dotted line)= horizontal advection; 3(dashed line)= cross isopycnal advection; 4(solid line)= double diffusion; Residuals indicated by squares. Note scale is twice as large as used in cartesian figures.

Chapter 5. Summary and Conclusions

In order to compare the results of the cartesian and isopycnal inversions, we first review the physics represented by each formulation. Although comparison would be more straightforward if the physics were identical, the cartesian inversions were done first, and the results of that model were taken into account in designing the isopycnal model.

In the diffusive cartesian model, we had a system of 117 equations in 46 unknowns. Constraints imposed were conservation of heat and salt at 6 depth levels, and a linear vorticity balance. Mass balance was assured by using the continuity equation to compute $w(z)$. At each horizontal location, we solved for u_0 , v_0 and w_0 , and solved for a horizontally averaged $\kappa_T(z)$ and $\kappa_S(z)$. We found that horizontal advection (which increased temperature and salinity) was balanced by the sum of vertical advection and diffusion (which decreased temperature and salinity). Individually however, both the vertical advection and diffusion had very large error bars. The horizontal reference velocities were the primary parameters used in the inversion to reduce the residuals. We also found that the spring solution was noisier than the fall, having both larger residuals and larger error bars on w and κ .

The isopycnal formulation consisted of a system of 108 equations in 73 unknowns, significantly more free parameters than the cartesian model had. The constraints imposed at each horizontal location were mass, heat and salinity balances at 4 adjacent depth levels, which covered the same depth range as the 6 cartesian levels. Rather than using the finite difference form to solve for (poorly resolved) diffusion coefficients, we solved directly for fluxes. Instead of imposing analytic constraints to determine the vertical structure of the vertical velocity, we allowed the solution to directly determine cross-isopycnal velocity at each level. We also solved for reference velocities u_0 and v_0 at each horizontal location. Horizontally averaged double-diffusive fluxes of heat and salt, related by the ratio γ , were sought between sigma theta 26.8 and 27.2, the levels

where staircases are found. The inversion used all the parameters together to reduce the residuals, rather than using primarily horizontal velocities, as was found in the previous formulation. The horizontal velocities were similar to the cartesian solution, but had slightly larger error bars. Horizontal advection acted to increase temperature and salinity, and double diffusion had the opposite effect, as expected. Double-diffusive flux divergence was similar in the spring and fall inversions. Cross-isopycnal velocity had a magnitude of about $5 \times 10^{-4} \text{ cm/s}$, varied in sign and had smaller error bars than the cartesian vertical velocity. The smaller error bars are partly due to the fact that w^* was determined directly, so that the error bars have no contribution from the error in computing the divergence of the horizontal velocities.

With the isopycnal model, we have better resolution of the double diffusive fluxes, probably due to better isolation of the staircase structure in the vertical, and more effective parameterization of cross-isopycnal processes. Diffusive fluxes confined to the steps and related through the flux ratio, γ , better represent the expected effects of double diffusion than the turbulent diffusivities in the cartesian model. These turbulent diffusion coefficients were non-zero outside the staircase depths, where physical interpretation is not obvious since sub-grid scale eddies are not expected to be significant. In the cartesian inversion of the spring data, the turbulent diffusion coefficients took on large negative values in the uppermost level where staircases were not present. The role of these negative diffusion coefficients in the solution may have been to reduce the residuals caused by the large eddy variability seen on the shallow pressure surfaces (see e.g. table 2).

Inversions using either cartesian or isopycnal layers gave similar estimates of horizontal reference level velocities. The reference velocities acted to reduce the strength of the eddy field and to bring the solution closer to a steady state model. The current meter constraints, on the other hand, emphasized the barotropic eddy field. With just one current meter, the horizontal structure of the eddy field was insufficiently constrained,

and the inversion could not find a solution which was consistent with the tracer data. In order to usefully include current meter constraints, it would be necessary to have enough current meters to delineate the eddy field, which in this region necessitates a spacing of about 100 km.

We were only partly successful in determining the regional advection–diffusion balance in the C–SALT staircases. The horizontally averaged balance of terms in all of the solutions suggests that horizontal advection is a major process in bringing in heat and salt, and that diffusion acts to cool and freshen this water. It is not possible to conclude that these are the dominant processes in this region, since the vertical advection also seems to be at least an order of magnitude greater than that assumed by Lambert and Sturges (1977) for the northeastern Caribbean Sea.

It is difficult to define an average velocity in a region dominated by energetic eddies, but the horizontal advection term determined by these inversions is probably a reasonable spatial average. Attempts to estimate long term average diffusion using spatially smoothed data and the cartesian formulation were unsuccessful. This was probably due to the fact pointed out by Tziperman (1987) that estimates of secondary parameters (ie., those determined from the residuals left after the primary parameters have been determined) are unreliable. Since in the isopycnal formulation, both horizontal and across–isopycnal velocities are primary parameters, it may be worthwhile to attempt further inversions using the isopycnal formulation with smoothed data to obtain meaningful average values of cross–isopycnal processes.

Appendix: Error estimates

The error associated with the RHS of each equation is primarily due to the errors in computing the geostrophic relative velocity. Expressing the total velocity as the sum of the “correct” velocity u , plus an uncertainty, Δu , and similarly for the mapped tracer c , the advection term can be written as

$$\nabla \cdot (uc + \Delta uc + u\Delta c + \Delta u\Delta c).$$

Neglecting second order terms, the error can be approximated by the terms:

$$\nabla \cdot (\Delta uc + u\Delta c).$$

The error in the velocity is due to the cumulative errors in the mapped density from which it is computed:

$$\Delta u_{rel} = \frac{g}{f\rho_0} \frac{\partial}{\partial y} \Delta \left(\sum_{i=1}^N \rho_i dz_i \right).$$

Assuming the errors in ρ at each level are independent and of constant value σ , the error due to the sum can be expressed as:

$$\Delta \left(\sum_i \rho_i dz_i \right) = \overline{dz_i} \sqrt{N} \sigma$$

where the overbar indicates the RMS average. The estimated error in each of the horizontal velocities is then

$$\Delta u = \frac{g \overline{dz}}{f\rho_0 dy} \sqrt{N} \sigma$$

The average value of σ was estimated to be about $5 \cdot 10^{-6}$ by inspection of $(\rho_{map} - \rho_{obs})/\rho_{obs}$.

The error in w , which is computed from the continuity equation as the sum of 4 terms involving horizontal velocity, can be approximated by

$$\Delta w = (\sqrt{4} \cdot \Delta u) \frac{dz}{dx} \approx 9 \cdot 10^{-4} \Delta u.$$

The error in the RHS due to error in the relative velocities can be expressed as (including multiplication by 6 months to get units of temperature or salinity)

$$dt \frac{\partial}{\partial x} (\bar{c} \Delta u) \approx 1.56 \cdot 10^7 \frac{s}{6mo} \Delta u \frac{(C_E - C_W)}{dx}.$$

Similarly for the vertical velocity term:

$$\Delta t \frac{\partial}{\partial z} (\bar{c} \Delta w) \approx 1.56 \cdot 10^7 \frac{s}{6mo} \Delta w \frac{(C_U - C_L)}{dz}.$$

The RMS sum of the (assumed) independent errors gives the expected error on the RHS of each equation for each depth level:

$$err(RHS)^2 \approx (1.4 \cdot \Delta u \cdot \Delta C_{EW})^2 + (1.4 \cdot \Delta v \cdot \Delta C_{NS})^2 + (.31 \cdot 10^4 \cdot \Delta w \cdot \Delta C_{UL})^2.$$

These error estimates are tabulated for each depth in Table 2. The units are the change in temperature and salinity in each control volume which would be expected to accumulate over 6 months just due to errors in the relative velocities.

References

- Boyd, J. D., and H. Perkins, 1987. Characteristics of thermohaline steps off the north-east coast of South America, July 1983. *Deep-Sea Res.*, Vol. 34, pp. 337-364.
- Bretherton, F. P., R. E. Davis and C. B. Fandry, 1976. A technique for objective analysis and design of oceanographic experiments applied to MODE-73. *Deep-Sea Res.*, Vol. 23, pp. 559-582.
- Bruce, J. G., and J. L. Kerling, 1984. Near equatorial eddies in the North Atlantic. *Geophys. Res. Letters*, Vol. 11, pp. 779-782.
- Chandler, C. L. and R. W. Schmitt, 1987. C-SALT CTD data report R/V Endeavor 128. W.H.O.I., unpublished document.
- Elliot, A. J., M. R. Howe and R. I. Tait, 1974. The lateral coherence of a system of thermohaline layers in the deep ocean. *Deep-Sea Res.*, Vol. 21, pp. 95-107.
- Fuglister, F. C., 1960. *Atlantic Ocean atlas of temperature and salinity profiles and data from the international geophysical year of 1957-58, Vol. 1.*
- Ingham, M. C., 1966. The salinity extrema of the World Ocean. Ph.D. dissertation, Oregon State University, Corvallis.
- Lambert, R. B., and W. Sturges, 1977. A thermohaline staircase and vertical mixing in the thermocline. *Deep-Sea Res.*, Vol. 24, pp. 211-222.
- Lanczos, C., 1961. *Linear Differential Operators*, Van Nostrand, Reinhold, New York, 564 pp.
- Mazeika, P. A., D. A. Burns and T. H. Kinder, 1980. Mesoscale circulation east of the southern Lesser Antilles. *J. Geophys. Res.*, Vol. 85, pp. 2743-2758.
- McDougall, T. J., 1984. The relative roles of diapycnal and isopycnal mixing on subsurface water mass conversion. *J. Phys. Oceanogr.*, Vol. 14, pp. 1577-1589.
- Metcalf, W. G., 1968. Shallow currents along the northeastern coast of South America. *J. Mar. Res.*, Vol. 26, pp. 232-243.

- Olbers, D. J., M. Wenzel and J. Willebrand, 1985. The inference of North Atlantic circulation patterns from climatological hydrographic data. *Rev. Geophys.* Vol. 23, pp. 313-356.
- Roemmich, D., 1983. Optimal estimation of hydrographic station data and derived fields. *J. Phys. Oceanogr.*, Vol. 13, pp. 1544-1549.
- Schmitt, R. W., 1979a. Growth rate of super-critical salt fingers. *Deep Sea Res.*, Vol. 26A, pp. 23-40.
- Schmitt, R. W., 1979b. Flux measurements on salt fingers at an interface. *J. Mar. Res.*, Vol. 37, pp. 419-436.
- Schmitt, R. W., 1981. Form of the temperature-salinity relationship in the Central Water: evidence for double-diffusive mixing. *J. Phys. Oceanogr.*, Vol. 11, pp. 1015-1026.
- Schmitt, R. W., 1987. The C-SALT program. *EOS*, Vol. 68, pp. 57-60.
- Schmitt, R. W. and D. L. Evans, 1978. An estimate of the vertical mixing due to salt fingers based on observations in the North Atlantic Central Water. *J. Geophys. Res.*, Vol. 83, No. C6, pp. 2913-2919.
- Schmitt, R. W., H. Perkins, J. D. Boyd and M. C. Stalcup, 1987. C-SALT: an investigation of the thermohaline staircase in the western tropical North Atlantic. *Deep-Sea Res.*, in press.
- Stern, M. E., 1960. The 'salt fountain' and thermohaline convection. *Tellus*, Vol. 12, pp. 172-175.
- Stern, M. E. and J. S. Turner, 1969. Salt fingers and convecting layers. *Deep-Sea Res.*, Vol. 16, pp. 497-511.
- Turner, J. S., 1967. Salt fingers across a density interface. *Deep-Sea Res.*, Vol. 14, pp. 599-611.
- Turner, J. S., 1973. *Buoyancy effects in fluids*. Cambridge University Press, Cambridge.
- Tziperman, E., 1987. Mixing and general circulation dynamics: theory and observations. Ph.D. Thesis, M.I.T.

- Wiggins, R. A., 1972. The general linear inverse problem: Implication of surface waves and free oscillations for earth structure. *Rev. Geophys. Space Phys.*, Vol. 10, pp. 251-285.
- Williams, A. J., 1974. Salt fingers observed in the Mediterranean Outflow. *Science*, Vol. 185, pp. 941-943.
- Wunsch, C., 1978. The North Atlantic general circulation west of 50° W determined by inverse methods. *Rev. Geophys. and Space Phys.*, Vol. 16, pp. 583-620.
- Wüst, G., 1964. *Stratification and circulation in the Antillean-Caribbean Basin*. Columbia University Press, 130 pp.

Acknowledgements

Thanks to Carl Wunsch for his always insightful criticism, which both improved my work and built character. Thanks to Jim Price for invaluable encouragement in my early formative years. Thanks to Ray Schmitt for the CTD data and for helpful and inspiring discussions. Thanks to Hank Perkins for graciously providing the current meter data in whatever form I wanted. Thanks to Bud Brown for skillful drafting services, cheerfully rendered. Thanks to Barbara Grant, who masterfully intervened in those tense situations when the computer and I failed to communicate. Thanks to Eli Tziperman, from whom I learned countless valuable lessons, including *how to complete impossibly complicated tasks in only 5 minutes*, and of course, the importance of not over-doing it. Thanks especially to my good, good friends, (a.k.a. fellow punishers) who have contributed enormously to making this endeavor almost worth all the time it took me. (Well, I guess if you throw in the 60 lbs. of salmon at the end – it was worth it – definitely.) This work was supported by Office of Naval Research grant N00014-85-G-0241.